

Motion Compensated Iterative Reconstruction for Cardiac X-ray Tomography

Alfonso Agatino Isola

Colophon

This book was typeset by the author using L^AT_EX₂_ε. The main body of the text was set using a 10-points Computer Modern Roman font. All graphics and images were formatted as Encapsulated PostScript (™ Adobe Systems Incorporated). The final PostScript output was converted to Portable Document Format (PDF) and transferred to film for printing.

Cover design by Valentina Cristalli using the Adobe Illustrator CS 3. All rights reserved. The graphics on the cover shows a segmented human heart and the corresponding estimated surface's motion vector fields (cyan arrows).



The research described in this thesis was carried out at the Philips Research Laboratories (Hamburg, Germany) and the Erasmus MC – University Medical Center Rotterdam (Rotterdam, The Netherlands).

This work received financial support of the European Community under a Marie-Curie Host Fellowship for Early Stage Researchers Training, MEST-CT-2005-020424.

Copyright © 2010 by Alfonso A. Isola. All rights reserved. No part of this publication may be reproduced or transmitted in any form or by any means, electronic or mechanical, including photocopy, recording, or any information storage and retrieval system, without permission in writing from the author.

ISBN 978-88-905004-0-4

Printed by Ipskamp Drukkers B.V., Enschede, The Netherlands.

Motion Compensated Iterative Reconstruction for Cardiac X-ray Tomography

Iteratieve reconstructie met bewegingscorrectie voor cardiale
Röntgen-CT-beeldvorming

Proefschrift

ter verkrijging van de graad van doctor aan de
Erasmus Universiteit Rotterdam
op gezag van de
rector magnificus

Prof.dr. H.G. Schmidt

en volgens besluit van het College voor Promoties.

De openbare verdediging zal plaatsvinden op
vrijdag 18 juni 2010 om 11:30 uur

door

Alfonso Agatino Isola

geboren te Catania, Italië



Promotiecommissie

Promotor: **Prof.dr. W.J. Niessen**

Overige leden: **Prof.dr.ir. A.F.W. van der Steen**

Prof.dr. P.J. de Feyter

Prof.dr. F.J. Beekman

Copromotor: **Dr. M. Grass**

Preface

The important thing is not to stop questioning. Curiosity has its own reason for existing. One cannot help but be in awe when he contemplates the mysteries of eternity, of life, of the marvellous structure of reality. It is enough if one tries merely to comprehend a little of this mystery every day. Never lose a holy curiosity.

— ALBERT EINSTEIN (1879 – 1955)

This thesis describes the research I carried out as part of my Ph.D. study at the Philips Research Laboratories, Hamburg, Germany and at the Erasmus MC, University Medical Center Rotterdam, The Netherlands.

Legends make us believe that in the remote past research had to be carried out by solitary and eccentric scientist secluded in a small and dark tower room. During the past three years, I have experienced the exact opposite. To be successful, research requires the cooperation of a multitude of inspiring people working in a multi-disciplinary research team. Thus, I would like to acknowledge the people who have made the completion of this doctoral dissertation possible.

First of all, I would like to thank my promotor and co-promotor, Prof. Wiro J. Niessen and Dr. Michael Grass. Wiro gave me the opportunity to join the Biomedical Imaging Group at Erasmus MC to perform this Ph.D. research. I am deeply indebted to him for his assistance and supervision of this work, and for teaching me how to carry out academic research. Michael initiated this project. His vast experience and clear ideas on scientific research, passed on during many interesting discussions, were extremely helpful and motivating. I would also like to thank Andy Ziegler, who was my tutor at Philips Research Laboratories during the first six months of this work. I am greatly indebted to him for his infinite patience and help in introducing me to the fantastic world of iterative CT image reconstruction and medical CT imaging.

The majority of this thesis was carried out at Philips Research Laboratories, Hamburg, Germany (PFL-H) where numerous people were involved. Many people contributed to making my time at the laboratory pleasurable and productive: Dirk Schäfer who introduced me to thin-plate spline interpolation and multiplanar reformation methods; Holger Schmitt helped me with all kinds of questions about myocardial perfusion; Peter Forthmann provided me with many good ideas about scattered interpolation, and in particular I am grateful to him for kindly providing me the segmented human heart shown on the cover of this book; Udo van Stevendaal for his help on in-

roducing me to the cardiac-motion compensation image reconstruction theory; Ewald Rössl for his help for improving the inverse deformation field technique used in chapter 5; Klaus Erhard helped me with all kinds of image reconstruction-related questions; Herman Schomberg provided me support and discussion on theoretical questions. Special thanks go to Thomas Köhler for our frequent brainstorming about iterative and analytical image reconstructions. During my stay at PFL-H I also had the great opportunity to collaborate intensively with the people from Digital Imaging group. My great thanks go to Cristian Lorenz, Jens von Berg, Steffen Renisch and Sven Kabus for introducing me to the field of image registration for aligning pulmonary CT images. Finally, I want extend many thanks to Roland Proksa for revising my publications and to our department heads, Dye Jensen and Günter Zeitler. I enjoyed and appreciated the friendly and cooperative atmosphere of the “hamburger” Philips Research Laboratories.

The work described in chapter 4 was partially completed at the Erasmus University MC Rotterdam, Departments of Medical Informatics and Radiology, Biomedical Imaging Group Rotterdam, The Netherlands. I enjoyed the collaboration with this group, and I valued the excellent support of Coert Metz, Michiel Schaap and Stefan Klein on introducing me to the field of coronary centerline extraction and elastic image registration, and Ihor Small for kindly providing me the latex templates used to realize this book.

It is hard to not mention my co-Ph.D. students at PFL-H who have made my stay in Hamburg special and a pleasure: my office mate Mariya Doneva, Tobias Voigt, Eberhard Hansis, Ronny Ziegler, Sebastian Zander, Hanno Homann and Uwe Jandt. I greatly enjoyed our daily coffee breaks, and discussions about medical imaging, soccer, religion, Italian politics, Italian kitchen, and so on.

I am beholden to my beloved parents, Mario and Maria, my brothers Dario and Marco and my cousins Mimmo and Alfonso for their material and non-material support in all these years and for leading me always in the right direction.

Last but not least, I would like to acknowledge my girlfriend, Valentina, who will soon become my wife. She is always happy to share my joy and, when needed, remove my doubts. She was, is and will always be the most important person of my life. I will never finish to thank her for supporting me throughout these years and making my existence so special.

Alfonso A. Isola
Rotterdam, February 2010

Contents

Colophon	ii
Preface	v
Abbreviations	xi
1 Introduction	1
1.1 Historical perspective of computed tomography	1
1.2 Cardiac CT applications	3
1.2.1 Coronary artery calcium scoring	4
1.2.2 Detection and characterization of coronary artery stenoses	4
1.2.3 Morphological and functional assessment of heart chambers	5
1.3 Cardiac CT acquisition strategies	6
1.3.1 Prospective ECG triggering	7
1.3.2 Retrospective ECG gating	8
1.4 Cardiac CT reconstruction strategies	9
1.4.1 Aperture weighted cardiac reconstruction for cone-beam CT . .	9
1.4.2 Iterative reconstruction for cardiac cone-beam CT	10
1.5 Imaging artifacts	11
1.5.1 Motion artifacts	12
1.5.2 Banding artifacts	12
1.5.3 Streak artifacts	12
1.6 Motion compensated reconstruction	12
1.7 Thesis outline	13
2 Motion-compensated iterative cone-beam CT image reconstruction with adapted blobs as basis functions	17
2.1 Introduction	18
2.2 Method and materials	19
2.2.1 Iterative reconstruction using spherically symmetric basis functions	19
2.2.2 Voxel-dependent footprint	20
2.2.3 Volume-dependent footprint for motion-compensated iterative reconstruction	23

2.2.4	Motion-compensated image reconstruction with cardiac gated SART	27
2.2.5	Software phantoms and simulations	29
2.3	Results	31
2.4	Discussion	32
2.5	Conclusions	39
3	Motion-compensated iterative reconstruction of a region of interest in cardiac cone-beam CT	41
3.1	Introduction	42
3.2	Method and materials	43
3.2.1	Introduction	43
3.2.2	Basis functions and the iterative statistical reconstruction method	43
3.2.3	MC iterative reconstruction of a cardiac region of interest	45
3.2.4	Motion estimation by manual tracking of anatomical landmarks	46
3.3	Experiments and results	47
3.4	Discussion	53
3.5	Conclusions	58
4	Cardiac motion-corrected iterative cone-beam CT reconstruction using a semi-automatic minimum cost path-based coronary centerline extraction	61
4.1	Introduction	62
4.2	Methodology	63
4.2.1	4D ROI image reconstruction	63
4.2.2	Local motion estimation by semi-automatic coronary centerline extraction	65
4.2.3	Motion-corrected iterative cardiac CT ROI reconstruction	66
4.3	Experiments and results	68
4.3.1	Clinical cases and helical cone-beam CT scanners	68
4.3.2	Manually indicated start-end coronary centerline points	68
4.3.3	Coronary motion-vector field estimation	70
4.3.4	Clinical validation	71
4.3.5	Image quality assessment	76
4.3.6	Manual and semi-automatic coronary arteries motion estimation	76
4.4	Discussion	77
4.5	Conclusions	79
5	Fully automatic non-rigid registration-based local motion estimation for motion-corrected iterative cardiac CT reconstruction	81
5.1	Introduction	82
5.2	Methodology	84
5.2.1	Introduction	84

5.2.2	Generation of 4D image data sets	84
5.2.3	The elastic image registration (EIR) framework	84
5.2.4	Extraction of the cardiac motion vector fields	88
5.2.5	Motion-corrected image reconstruction with SART	90
5.3	Experiments and results	92
5.3.1	CT scanning and reconstruction settings	93
5.3.2	Phantom study	93
5.3.3	Cardiac motion estimation	96
5.3.4	Consistency study of the estimated motion vector fields	98
5.3.5	MC iterative coronary ROI reconstructions in patient data	101
5.3.6	Validation on clinical data of the blobs volume-adaptation for MC iterative reconstructions	105
5.4	Discussion	107
5.5	Conclusions	109
6	Summary	111
	Bibliography	115
	Samenvatting	125
	PhD Portfolio	129
	Publications	131
	Curriculum Vitae	133

Abbreviations

2D	two-dimensional
3D	three-dimensional
4D	four-dimensional
CT	computed tomography
HU	Hounsfield unit
ECG	electrocardiogram
ROI	region of interest
FOV	field of view
RCA	right coronary artery
LCA	left coronary artery
LV	left ventricle
MAD	mean absolute difference
NCC	normalized correlation coefficient
SSD	sum of squared differences
STD	standard deviation
SNR	signal-to-noise ratio
EIR	elastic image registration
RM	stochastic gradient descent of Robbins-Monro
FBP	filtered back-projection
FDK	Feldkamp reconstruction algorithm
EBCT	electron-beam CT
MSCT	multi-slice computed tomography
MVF	motion vector field
MC	motion-compensated
MM	motion map
AWCR	aperture weighted cardiac reconstruction method
MC AWCR	motion-compensated AWCR
ML	convex maximum likelihood algorithm
OSML	iterative ordered subsets convex ML
AWCOSML	aperture weighted cardiac OSML
MC AWCOSML	motion-compensated AWCOSML
ART	algebraic reconstruction technique
SART	simultaneous ART
gated AWSART	ECG-gated aperture weighted SART
MC gated AWSART	motion-compensated gated AWSART
MC gated AWSART _{nvs}	MC gated AWSART w/o blob volume scaling

Introduction

Radiology has not come to the end of its expansion, and in spite of all the advances of fifty years the vista of progress still stretches out in front of us. In the fascinating country already charted and signposted there are still many by-paths to be explored even by those who now travel by motor car where the pioneers had to blaze the exciting trails before the paths were made. And for those spirits that are more adventurous there are still uncharted lands over the horizon, lands that will open up and through which one day the roads will run.

— ALFRED ERNEST BARCLAY (1876 – 1949)

1.1 Historical perspective of computed tomography

Computed tomography (CT) is a method that generates images of the interior of the body by digital computation applied to the measured transmission of X-rays. It achieves this by rotating an X-ray source and a set of aligned X-ray detectors around the patient. The word tomography is derived from the Greek *tomos* (cut) and *graphein* (to write).

The history of CT starts in Germany in 1895 when Wilhelm Conrad Röntgen (1845-1923) (Fig. 1.1(a)) discovered a new type of radiation, which he called X-rays [105]. This type of electromagnetic radiation, which has a shorter wavelength than visible light and the ability to penetrate matter, was immediately used to image the interior of the human body. The images thus obtained showed a two-dimensional (2D) projection of the inner structures. The contrast in the images was based on the differences in X-ray attenuation coefficients and in the thickness of the various tissues. In 1901 Röntgen received the first Nobel prize for physics. Basic to the CT technology are the theoretical principles of reconstruction of a three-dimensional (3D) object from multiple two-dimensional (2D) views relying on a complex mathematical model, as formulated by Johann Radon in 1917 [100].

In 1956 the South African nuclear physicist Allan M. Cormack (1924-1998) (Fig. 1.1(b)) initiated his work on cross-sectional imaging to improve the radiotherapy treatment planning. In 1963 and 1964 he published his work on the problem of reconstructing a cross-section of a body by using information from projection data through that body [13]. Cormack tested his method with transmission measurements

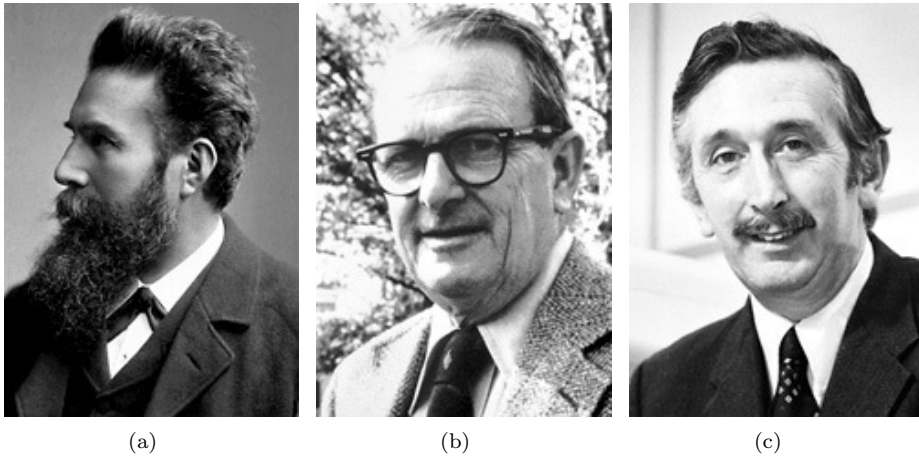


Figure 1.1. Three Nobel prize winners who played a role in the history of computed tomography. (a) W. C. Röntgen, (b) A. M. Cormack, (c) G. N. Hounsfield. Photographs © The Nobel Foundation.

obtained from a phantom using gamma radiation. His efforts were not directly used for diagnostic applications. In any case the computing power was not sufficient at that time. The principle of reconstructing cross-sections was introduced into the medical world by the British engineer Godfrey Newbold Hounsfield (1919-2004) (Fig. 1.1(c)). Hounsfield developed his own reconstruction technique as he was unaware of Cormack's work. In 1972 he presented the first full-scale CT-scanner (EMI Mark I, EMI Ltd., London, United Kingdom) and the first picture of a patient's head [34]. This image represented a cross-section with a thickness of 13 mm and consisted of a matrix of 80 by 80 pixels, which showed the anatomical structure of the brain. Compared to a plain X-ray image, the CT image showed remarkable contrast between tissues with small differences in X-ray attenuation coefficient. Godfrey Hounsfield and Allan Cormack were both rewarded in 1979 by the Nobel prize committee with the Nobel prize for medicine "for the development of computer assisted tomography".

An outstanding innovation opening the doors towards heart imaging was introduced in 1982 [7] with the electron-beam CT (EBCT). This system does not contain any moving mechanical parts, but it accelerates a focused electron beam towards stationary tungsten targets, thus permitting very rapid scanning times. A dramatic reduction of temporal resolution to 50-100 ms for an axial slice, and a slice thickness at the submillimeter level (0.8 mm) enabled the acquisition of images showing the calcium in the coronary arterial wall which could be quantified [3]. Using X-ray opaque contrast agent, the first non-invasive coronary angiography studies could be obtained [1]. A major drawback of EBCT were the high cost of both the purchase and maintenance of the system, which has greatly limited widespread use of this technique. The introduction of CT technology based on the so-called spiral or helical acquisition, late in the 1980s, also represented an important step. In these systems, a sliding ring containing both, the X-ray emitting source and the detectors, allows a

fast continuous rotation of the gantry that sweeps around the body of the patient in a helical course as the table is continually moving in the direction of the longitudinal axis [49]. The rotation time of the gantry was initially in the order of 1 s, while in 1994 it had been reduced to 0.75 s. For the first time a true volumetric acquisition of an anatomical region in 25-30 s became feasible, with slices between 2-10 mm thickness [49]. Despite these features, however, the achievement of adequate images of the heart and the coronary arteries was still beyond the scope of CT.

An important advance was the introduction of multi-slice CT (MSCT) technology, in 1993. Systems initially had 2 rows of detectors [72], which reduced the time of the examination. Then, systems equipped with 4 rows of parallel detectors were set up, in 1998, providing rotation times of 0.5 s and, by means of complex segmentation algorithms, reconstructions with a temporal resolution between 125-250 ms [88]. Spatial resolution was also improved as slice thickness was reduced to 1-1.25 mm. With these advances, the achievement of a cardiac volume free of movement artifacts was feasible, although this implied a breath-hold time between 35-45 sec. Systems with 8, 12 and 16 rows of detectors soon followed, the latter becoming available in 2002, for the first time allowing, the acquisition of cardiac volume data with true isotropic spatial resolution: identical size of the voxel in the three planes, between 0.5-0.625 mm, and with rotation time below 0.5 s [67, 87, 106]. The required breath-hold time for 16-slice equipments is between 20-30 s. Relevant as they are, these improvements have not been considered sufficient for cardiac examination, and in 2004-2005, new generations of MSCT equipped with 32, 40, and 64 detectors have been introduced [31, 64, 89]. The main advantage, in practice, of these new systems is the reduction in scan time, allowing breath-hold times lower than 10 s, which results in a high image quality for most cardiac studies that are free from arrhythmia or respiratory artifacts.

Latest CT scanners image 256 slices simultaneously, with a coverage along rotational axis up to 80 mm and rotation time as short as 0.27 s. Moreover, several protocol-driven and patient-adaptive dose reduction technologies are integrated that automatically use the quantity and quality of radiation where and when needed, leading to dose reductions of up to 80% over previous methods (Philips Brilliance iCT, Philips Healthcare, Cleveland, OH, USA). A recently introduced 320 slices CT system (Aquilion One, Toshiba Medical Systems, Tokyo, Japan) thanks to its array of 320 ultra high resolution 0.5 mm detector elements, it has a z-axis detector coverage of 160 mm, large enough to cover the entire heart in a single rotation and thus avoiding to scan over several heart beats [110].

1.2 Cardiac CT applications

Cardiac imaging is a rapidly emerging clinical technique for non-invasive diagnosis of cardiovascular diseases [10]. For example, monitoring of coronary artery calcium progression could be a potential tool for the identification of patients at risk of suffering from myocardial infarction [144].

Early detection and evaluation of high-grade stenotic segments in the coronary arteries is another important clinical application of cardiac CT imaging, as it can be used for diagnosing coronary artery disease and guiding therapy options to prevent

acute myocardial infarctions [31, 64]. Furthermore, analysis of CT images of the left ventricle (LV) allows detection of possible mitral valve stenosis, which can be responsible for pumping abnormalities and the consequent insufficient blood flow from the heart to all the organs and tissues of the human body.

Another application is *functional imaging* of the heart. By retrospectively gating (see Chp. 1.3.2) a reconstruction from the same data set in any given phase of the cardiac cycle is allowed. Hence, an evaluation of functional cardiac parameters is possible, enabling the assessment of cardiac parameters such as wall motion and ejection fraction. Finally, *myocardial perfusion imaging* by follow-up CT scanning is a promising diagnostic tool to assess the extent of infarcted myocardial regions.

1.2.1 Coronary artery calcium scoring

There is an increasing interest in cardiology to go beyond the traditional coronary risk factors and, pending the discovery of a simple screening test for the detection of the asymptomatic vulnerable patient, also base the coronary risk prediction in the detection and quantification of coronary artery calcium as a marker of atherosclerotic disease.

Coronary artery calcium is an excellent marker of the process of atherosclerosis, as it is present almost exclusively in atherosclerotic plaques of the vessel wall, its amount correlating with the burden of the disease [144]. Electron-beam computed tomography (EBCT) has proven to be the first non-invasive technique for the quantification of coronary artery calcium. The development of MSCT has become a valuable alternative to EBCT.

The coronary artery calcium quantification method adopted for MSCT exams was initially introduced in 1990 by Agatston for EBCT scanners [3]. The *Agatston Score* [3] is strongly dependent on acquisition protocol and cardiac motion. This method is based on the X-ray attenuation coefficient (or CT number, measured in Hounsfield (HU)) and the area of calcium deposits. According to this method, densities equal to or greater than 130 HU are considered to correspond to calcium. Volume and mass calculation of the amount of calcium are alternative methods to the Agatston score for the evaluation of coronary artery calcium.

1.2.2 Detection and characterization of coronary artery stenoses

Multi-slice computed tomography (MSCT) is a potentially useful tool for a comprehensive study of the complex aspects of coronary artery lesions [31]. It allows, on one hand, to obtain of a noninvasive coronary angiography, or a *luminogram* of the arteries, where the degree of obstruction of lesions can be assessed. On the other hand, MSCT is not limited to this analysis but it is also able to provide information on the arterial wall itself and on the extent and components of atherosclerotic plaques. The assessment of coronary artery lesions by MSCT implies different, important aspects of their relevance, as is the magnitude of obstruction, and the composition of atherosclerotic plaques and its morphological features, all related to the stability of lesions. Typical degree of obstruction are: *non-significant stenoses* (less than 50% of

the vessel lumen); *borderline stenoses* (50-70%), and *significant stenoses* (more than 70%). A classification for the components of the lesion can be done in: *thrombotic lesions*, *non-calcified*, *mixed* or “*soft*” *lesions* (adipose or fibroadipose), and *calcified lesions* (fibrocalcified and calcified). The calcium component in the latter kind of lesion can be *focal*, *diffuse*, *eccentric* or *concentric*.

A typical diagnostic tool of MSCT to study coronary artery lesions consists of the visualization of reconstructed *axial images*. Although limited to a 2D view, axial images provide an adequate method for the analysis of cardiac and thoracic anatomy, and due to its excellent resolution, also for the evaluation of the components of the coronary atherosclerotic lesions.

To improve coronary artery visualization and lesion interpretation a *multiplanar reconstruction* (MPR) [10] can be utilized. The MPR consists of obtaining sections of the vessels on multiple orientation and is not limited to the axial plane. By means of *curved* MPR, a clear view of both lumen and the wall of the vessel is possible, leading to a detailed analysis of lesions. To perform a *curved* MPR, semi-automatic centerline extraction techniques [77, 111] are used to determine the center of the vessel through consecutive axial images. By computing this information, the system provides a two-dimensional image of the course of the vessel independent of its anatomic distribution.

Finally, another coronary artery diagnostic tool is *3D volume rendering*. This tool provides a 3D reconstruction of the coronary tree. The presence of a noncalcified atherosclerotic lesion, characterized by a reduction in the luminal density, is promptly detected, although 3D images are not the preferred method for the estimation of the severity of the lesion.

1.2.3 Morphological and functional assessment of heart chambers

Data on volume and function, particularly of the left ventricle, constitute important clinical information in all patients with heart disease. While a number of other imaging methods provide accurate data on these parameters and can be applied in clinical routine, MSCT estimations are valuable in those patients with proven or suspected ischemic heart disease who are referred to a noninvasive coronary angiography study [115]. The analysis of ventricular volume and function is performed from multiplanar reformations of the retrospectively ECG-gated data set obtained from a cardiac CT scan.

Myocardial perfusion imaging by MSCT represents a promising tool to support the diagnosis and treatment of acute infarctions [61, 66, 90]. An assessment of the heart muscle viability can allow to distinguish between necrotized and dysfunctional but viable tissues after acute or chronic ischemia, and can be used as an indicator of early heart disease [127].

Hypoenhanced regions on the initial scan, and hyperenhanced regions on late scans obtained 5-15 minutes after contrast material injection represent two types of abnormal myocardial enhancement patterns which have been described in literature [61, 66, 90]. A strong relationship, between the presence and size of these two abnormal myocardial defects and the degree of follow-up regional dysfunction after acute myocardial infarction was observed [66]. Also, the probability of myocardial

functional recovery is significantly inversely related to the presence and size of both early hypoenhanced and late hyperenhanced regions [66].

Animal studies have shown *early hypoattenuation* to be a measure of low reflow regions, which may result from abnormal flow at the level of either the epicardial artery and/or the myocardial capillaries [61, 66, 79, 94, 103].

Late hyperenhancement has been shown to be a marker of necrotic tissue [66, 103]. The mechanism of hyperenhancement of healed myocardial infarction or collagenous scar is thought to be related to an accumulation of contrast media in the interstitial space between collagen fibers [61, 66].

Finally, *dynamic myocardial perfusion* imaging by MSCT can be an efficient tool to quantitatively evaluate the condition of the myocardial tissue. Hereto, a cardiac follow-up CT scan (e.g. the *Step-and-Shoot* scanning-mode) can be applied to generate a sequence of volumes acquired during the first-pass of a contrast agent bolus. Then, the X-ray attenuation changes for each voxel in the acquired images can be visually evaluated by using the corresponding time-intensity curves [78, 120]. Moreover, these time-intensity curves can be used as an input for the assessment of quantitative perfusion-related parameters [78, 120].

1.3 Cardiac CT acquisition strategies

Challenges for image reconstruction in cardiac CT arise from the rather fast cardiac motion and incomplete data that are associated with helical (and circular) scanning combined with cardiac gating [26, 38, 44, 46, 48, 74, 121]. Cardiac CT is a special CT protocol, which has passed through three, chronologically overlapping, developmental stages and is now in its fourth stage of development. The first stage was fluoroscopy-based CT (1972-1995) stimulated by physiologic research needs. The next was clinical CT-based exploration (1975-1980) of the potential of clinical CT in cardiology. This was followed by the electron beam CT-based stage (1980-present), which was the first CT approach applicable to clinical cardiology. Finally, volumetric CT imaging methods achieved with multislice scanning approaches of helical CT (1998-present) show great promise for clinically applicable CT of the cardiovascular system.

MSCT allows fast acquisition and makes it possible to acquire redundant data. These improvements enabled the imaging of the heart. Especially reconstructions of quiet cardiac phases which can be found, as an example, at *late diastole*, yield good results [31, 64, 89]. This is due to the fact that the scanner's temporal resolution is high enough compared to the motion-speed of the heart. In order to correlate the reconstruction with the beating heart, an electrocardiogram (ECG) is recorded parallel to the acquisition.

There are two techniques of cardiac CT image reconstruction: *ECG-triggered*, or *prospective scanning*, and *ECG-gated*, or *retrospective scanning*. Both techniques are discussed in the following subsections. These two methods have in common that reconstruction is performed at a certain phase point referred to as *reference phase point*. To ensure that sufficient line integrals are acquired, a time window (*gating window*) is placed around the reference phase point. The width of this window is responsible for the temporal resolution of the system.

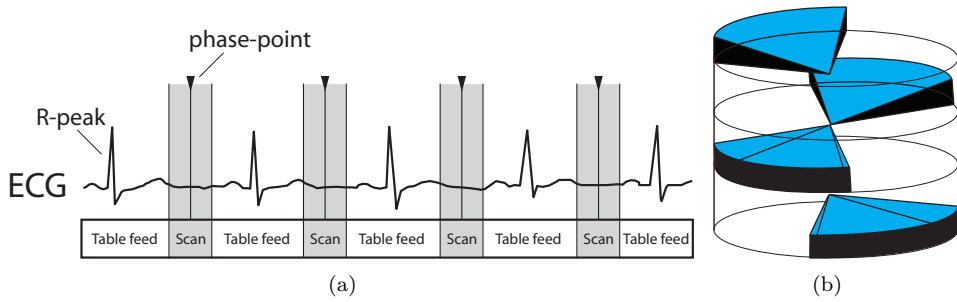


Figure 1.2. Prospective triggering: scanning time points are estimated in respect to the ECG’s R-peaks (a), and the *Step-and-Shoot* acquisition (b).

1.3.1 Prospective ECG triggering

When CT scanning is necessary to rule out coronary artery disease only, and functional information is not needed, it is sufficient to image and expose a single cardiac phase. In the prospective mode [29,36] the scanning is performed at a predetermined time window of the cardiac cycle, usually during *mid-diastole* (or *diastasis*) and *end-systole* (Fig. 1.2(a)). This time window can be defined in milliseconds from the R wave of the ECG, or as a percentage of the cardiac cycle. It can be combined with a helical or circular mode of acquisition, where the combination with the circular acquisition is more frequent. A typical scanning-mode used in prospective acquisition is the so called *Step-and-Shoot* (Fig. 1.2(b)). During acquisition, the table stops at a certain position, then data are acquired during one rotation of the gantry. The table is forwarded up to the next position, another cycle is recorded. This procedure is repeated until the complete volume is covered (Fig. 1.2).

Technological advances which enable the use of prospective gated coronary CT reconstructions represent a significant improvement in radiation dose reduction. Using a 64-slice and dual-source MSCT, prospective triggering has been shown to be technically and clinically feasible, and compared to retrospective gating dose reductions of 52-85 % have been reported [20,29]. Despite the promising results of these prospective ECG-triggered CT studies, current 64-slice and dual-source MSCT is limited to patients with heart rates below 75 bpm. Earls [19] noted that more than 40% of all patients presenting to cardiac CT angiography would have to be excluded from prospective CT acquisition without pharmacological heart rate control. Despite multiple oral and/or intravenous β blocker administrations, it was noted in [19] that 9.5% of patients still failed to meet appropriate prospective heart rate thresholds. Moreover, in obese patients with body mass index greater than 30 kg/m² lower image quality was observed [20].

Another great drawback for ECG triggering is the so-called *heart rate variability* [125] which describes the variation of beat-to-beat intervals. As the offset for each scan is derived from the preceding RR intervals, an ectopic beat can result a deviant delay and thus lead to incorrect projections at wrong table positions.

Recently, a 256-slice MSCT scanner with 0.27 s rotation, 120 kW X-ray tube,

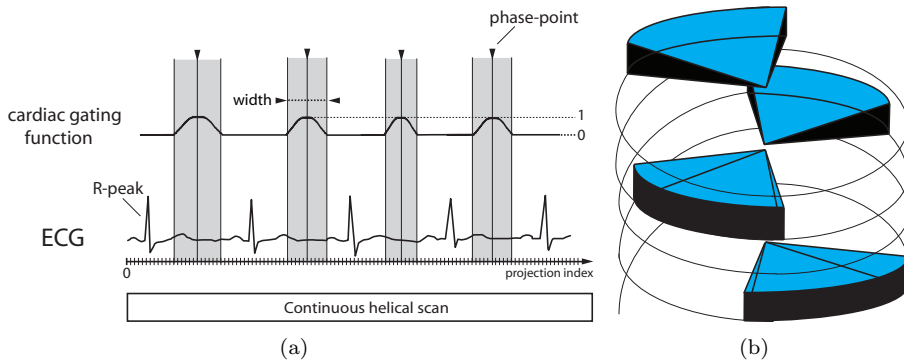


Figure 1.3. Retrospective scanning method: diagrams of the ECG-gating (a) and the corresponding segmented helical scan used for the reconstruction(b).

and an 80.0 mm detector array has been introduced (Philips Brilliance iCT, Philips Healthcare, Cleveland, OH, USA). While large scale studies are necessary, first early clinical results indicate that this new system potentially enables imaging beyond the 75 bpm and the 30 kg/m^2 body mass index thresholds without any β blocker medication. Moreover, in order to reduce the susceptibility of the prospective scanning to heart rate variations, new real-time arrhythmia handling mechanism are utilized. When arrhythmias are detected, the scan is stopped to prevent unnecessary dosage, and the anatomic region is then scanned after the ECG signal stabilizes [21, 143].

1.3.2 Retrospective ECG gating

Imaging tissue, or an organ, over multiple physiological phases (e.g. over the cardiac cycle) can provide both anatomical and functional information. In retrospective scanning [26, 45, 47, 57, 86, 122] the acquisition is performed in a continuous helical mode during one breath-hold. A simultaneous recording of the ECG allows for the reconstruction of images at determined phases throughout the cardiac cycle (Fig. 1.3). After the scan, each projection is assigned to its exact phase point. Thus, a prediction of phase points is not necessary. Retrospective gating enables calculation of the optimal width of the gating window. Heart rate is a crucial aspect in this mode, since more cardiac cycles are available in the breath-hold period. Consequently, a higher number of segments is available for the image reconstruction, thus improving the temporal resolution.

Retrospective scanning is thus the adequate mode of acquisition to study the left ventricular function, provided the acquisition of data over the whole cardiac cycle is continuous.

Continuous acquisition in the retrospective scanning mode leads to a higher radiation dose than in the prospective mode. To reduce the X-ray dosage, retrospective CT angiography is frequently performed using a helical scanning direction in combination with radiation dose modulation, i.e., the peak tube current is only used within a chosen temporal window of the R-R interval, while, outside this window a minimal

tube current is applied. Nevertheless, prospective ECG-triggered coronary CT angiography has shown to reduce radiation dose below that of retrospective ECG-gated coronary CT angiography with dose modulation [29]. Despite prospective triggering scanning is frequently applied for coronary CT angiography, retrospective exams are still preferred at higher heart rates or in obese patients, although with the new generation of 256-slice MSCT scanners the new exact maximum thresholds are still under research.

1.4 Cardiac CT reconstruction strategies

Nowadays, several strategies to reconstruct the 3D attenuation coefficient distribution from the measured projection data exist. In general, the reconstruction techniques can be divided into two classes: *analytical* and *iterative* methods. Analytical reconstruction methods [9, 22, 51, 128] apply an analytical inversion of the Radon transform [100] to give a direct solution to the reconstruction problem. Iterative reconstruction methods [17, 60, 85, 126, 148] solve the problem numerically by minimizing the difference (or ratio) between the forward projected image and the measured data, sometimes under the constraint of *a priori* knowledge about the imaged object. In the following subsections, a brief presentation of an analytical and iterative reconstruction methods for cardiac CT is given.

1.4.1 Aperture weighted cardiac reconstruction for cone-beam CT

The *Aperture Weighted Cardiac Reconstruction for Cone-Beam CT* (AWCR) is a heart-rate-adaptive helical cardiac cone beam reconstruction technique [57]. It is based on 3D filtered back-projection (FBP) [9, 22, 51, 128] using retrospective gating. It is similar to *Extended Cardiac Reconstruction* (ECR) [26], but makes use of data from all illumination windows. As previously mentioned, an ECG is recorded in parallel to the scanning. This provides a relation between the cardiac cycle and the time points at which every projection is recorded. One major aspect of AWCR is a weighting of line integrals depending on their associated phase point. Indeed, line integrals of quiet heart phases are emphasized while line integrals of strong motion shall be suppressed. Thus redundant line integrals belonging to the same phase point but not necessarily to the same cardiac cycle are collected. To achieve this, at least in good approximation, the common acquisition protocol is a helical cone-beam scan using a low pitch and short rotation times. Furthermore, larger detector arrays are of help to cover large parts of the object of interest.

The AWCR algorithm can be divided into few steps. First of all the fan-beam geometry is transformed into a parallel-beam geometry. Subsequently, the data are pre-weighted with the cosine of the cone-angle and high pass filtered in row direction applying a band limited ramp filter. Finally, the 3D-back-projection is performed after a weighting with an additional weighting function which takes cardiac motion constraints and the voxel-specific illumination into account. A more detailed introduction to the AWCR-framework can be found in [57].

1.4.2 Iterative reconstruction for cardiac cone-beam CT

Iterative reconstruction methods [4, 25, 60] represent a different approach for CT imaging which consists of assuming that the cross section consists of an array of unknowns, and then setting up algebraic equations for the unknowns in terms of the measured projection data. General advantages of iterative [4, 25, 60] compared to analytical reconstruction [85, 93, 126] are the ability to model the acquisition process accurately and to introduce *a-priori* knowledge about the imaged object. Moreover, iterative reconstruction methods have the potential to require less data than FBP methods, and they are more robust to the effects of noise [17, 85, 126, 148]. However, at the same time, a well known drawback of iterative reconstruction methods is the necessity that a field-of-view (FOV) has to be reconstructed that covers the whole volume, which contributed to the absorption. In the case of a high resolution reconstruction, this imposes very large memory and computation requirements during reconstruction. ROI reconstructions [149] can mitigate this problem.

Volumetric CT reconstruction algorithms determine the absorption function f of the object sampled by a set of 2D projections at different angles. A linear combination \tilde{f} of a limited set of basis functions b can be used to represent the continuous function f . A commonly used basis function is the cubic voxel. The boundaries of a voxel are exactly in the middle between neighboring grids. Spherically symmetric basis functions (also called “blobs”) represent another kind of bases which are frequently used in CT image reconstruction. Following Lewitt [69] for the works presented in this thesis, the Kaiser-Bessel basis functions [68] are used. These spherically symmetric basis functions have many advantages compared to simple cubic voxels, e.g. they are spatially limited and effectively frequency limited, and their appearance is independent of the source position [68].

The main goal of iterative CT reconstruction is to find the optimal set of coefficients μ_i that minimizes the difference (or ratio) between the measured p_j and calculated $\tilde{p}_j^{(n)} = \sum_{i=1}^N A_{ji}\mu_i^{(n)}$ projections, where A_{ji} are the elements of the system matrix, n is the iteration number, and $j = (1, 2, \dots, D)$ are the detector pixels. In chapter 2, a detailed description of the forward projection model [147] used to determine the contribution, A_{ji} , of each blob to the detector pixel, j , will be given.

Generally, iterative reconstruction methods may be divided into two groups. The first group including the *algebraic reconstruction technique* (ART) [25] (utilized for Hounsfield’s first CT scans), solves a system of linear equations $p_j = \sum_{i=1}^N A_{ji}\mu_i$ and does not take the statistics of the measurements into account. An ART algorithm finds the optimal set of coefficients μ_i by iteratively applying a correction array to each voxel (or blob) i as follows

$$\mu_i^{n+1} = \mu_i^n + \lambda \frac{p_j - \tilde{p}_j^n}{\sum_i a_{ji}} a_{ji}, \quad (1.1)$$

where the relaxation parameter, $0 < \lambda < 2$, controls the speed of convergence, and a_{ji} indicates a backprojection weight [147].

In Eq.1.1 a *ray-by-ray* update scheme is used. Hereto, each voxel value is sequentially updated by using the correction term generated by each ray in one projection.

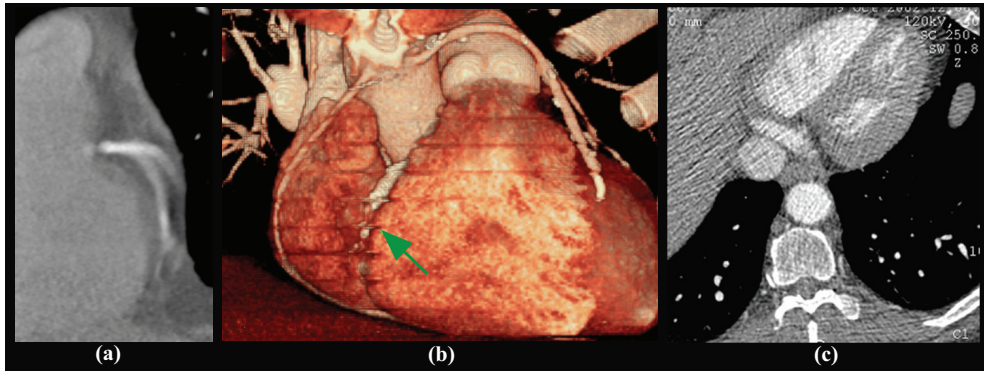


Figure 1.4. Imaging artifacts. The motion blurring (a), the banding (b), and the streak (c) artifacts are shown. In (b) the green arrow indicates an image area strongly degraded by banding artifacts.

A commonly used modification of ART is the *Simultaneous Algebraic Reconstruction Technique* (SART) [4] which lead to superior image quality by simultaneously applying to a voxel the average of the corrections generated by all rays in a projection.

The second group consists of the *statistical* iterative reconstruction methods, such as the *convex Maximum Likelihood* method (ML) [60]. These methods take care of the photon statistics in the measurement, resulting in a higher signal-to-noise ratio (SNR) of the reconstructed images compared to the analytical reconstruction methods [85, 93, 126].

In the next chapters 2-5, in order to increase the convergence speed of the iterative algorithm, efficient ordering schemes [28] will be applied to collect the measured projections in different ordered subsets. Moreover, as previously done for the AWCRC method, a suitable cardiac weighting will be introduced for each projection p_j in the reconstruction algorithm in order to select data belonging to the same cardiac phase and to perform an ECG-gated iterative reconstruction [86, 149].

1.5 Imaging artifacts

The detection of coronary artery lesions from an MSCT study is less problematic than their quantification. Artifacts can severely degrade the quality of a CT image and can lead to inaccurate or false diagnoses.

There are different sources of artifacts in an MSCT coronary angiography (e.g. aliasing, beam hardening, shading, metal, and patient or breathing motion-related artifacts) which are frequently responsible for those cases of disagreement between this technique and conventional invasive angiography [63, 84]. A good overview on CT image artifacts appearances, causes and possible corrections is given in [35]. The following paragraphs will focus on patient cardiac motion-related artifacts.

1.5.1 Motion artifacts

Movement artifacts primarily occur when images are reconstructed in inadequate phases of the cardiac cycle, e.g. in systole or during atrial contraction period. Increased heart rate can induce these artifacts by the shortening of systolic and diastolic periods and also by the increased heart motion. Premature atrial or ventricular beats, or arrhythmias in general, may also be causes of these artifacts.

Motion artifacts lead to blurred images leading to a poorly defined outline of vessel segments, particularly the right coronary artery (RCA) and left circumflex (LCx) arteries, due to their anatomic relationship with the atria (Fig. 1.4(a)). The use of beta-blocking agents or sedatives may reduce the appearance of movement artifacts.

1.5.2 Banding artifacts

These artifacts appear when the heart rate changes significantly during the acquisition time. A strong heart rate variation may lead to a reconstructed image composed of slices corresponding to slightly different phases of the cardiac cycle, resulting in images in which the cardiac shape abruptly changes in a stepwise manner (Fig. 1.4(b)). Banding artifacts are prone to appear at the end of the acquisition time, when the regularity of the cardiac cycle frequently tends to dissipate.

Modern CT systems with large area detectors (Aquilion One, Toshiba Medical Systems, Tokyo, Japan) can image the entire heart in one axial scan without table movement [110], and hence can avoid banding artifacts [23].

1.5.3 Streak artifacts

Streaking artifacts are usually induced by inconsistencies present in single measurements which yields bright lines or streaks in the reconstructed image (Fig. 1.4(c)). The projection data inconsistency could be the result of an inherent problem associated with the data collection process (e.g. patient cardiac motion). Because streak artifacts can mimic coronary artery diseases and cause misdiagnosis, special attention has to be paid to recognizing, avoiding, or correcting them.

1.6 Motion compensated reconstruction

As discussed so far, cardiac motion-related artifacts can degrade the quality of medical images and can hamper a reliable diagnosis of the heart condition. A motion compensated (MC) reconstruction [5, 71, 92, 98, 112, 113, 136] is therefore of great interest to reduce motion artifacts. In particular, MC reconstruction approaches can be applied to image coronary arteries of patient with a high heart rate variation, or if functional data is required, to reconstruct cardiac ROIs at phases of fast cardiac motion. In both situations, the current prospective and retrospective ECG gating methodologies fail to produce motion-artifact free images of the heart.

The prerequisite of MC reconstruction is the availability of motion vector fields (MVF). For a volumetric cardiac reconstruction the MVF is represented by a $\mathbb{R}^3 \rightarrow \mathbb{R}^3$

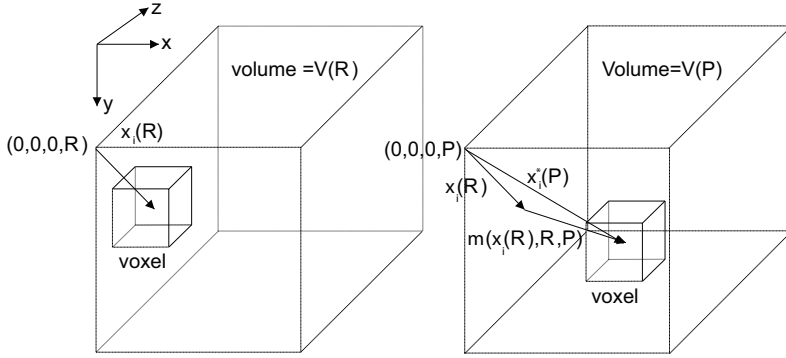


Figure 1.5. Format of the motion-vector field. For each voxel $\mathbf{x}_i(R)$ of the volume $V(R)$ in the reference phase R , the motion-vector field $\mathbf{m}(\mathbf{x}_i(R), R, P)$ describing the displacement of the voxel $\mathbf{x}_i^*(P) = \mathbf{x}_i(R) + \mathbf{m}(\mathbf{x}_i(R), R, P)$ in an arbitrary phase P is given.

mapping $\mathbf{m}(\mathbf{x}_i(R), R, P)$, which displaces each grid point $\mathbf{x}_i(R)$ at a reference heart phase R to a new position $\mathbf{x}_i^*(P)$ in an arbitrary heart phase P (Fig. 1.5) by

$$\mathbf{x}_i^* = \mathbf{x}_i^*(P) = \mathbf{x}_i(R) + \mathbf{m}(\mathbf{x}_i(R), R, P), \quad (1.2)$$

where $R \in [0, 1)$ is the selected reference percentage of the RR interval, and $i = 1, 2, \dots, N$ with $N = N_x N_y N_z$ and N_x, N_y , and N_z are the number of grid points in x, y , and z directions, respectively.

Several methodologies for extracting motion information from an ECG-gated 4D image data set exist in literature [5, 43, 95, 124, 136], three efficient techniques will be applied in the next chapters of this thesis. An MC iterative reconstruction can be used to take the motion of each blob into account during the forward projection step. In case of divergent motion, the MC iterative reconstruction method should take care of the blob-volume change as well. In the next chapter an MC iterative method which uses such volume-adapted blobs as basis functions will be proposed.

1.7 Thesis outline

The main focus of this thesis is to develop and evaluate methods to obtain motion artifact-free CT images of a cardiac region of interest at phases of strong cardiac motion. Generally, at these phases, standard ECG-gated or -triggered reconstruction methods produce blurred images. The aim of this work is twofold:

- To introduce a novel MC iterative CT reconstruction method for a cardiac ROI, which takes the motion into account during the iterative reconstruction process.
- To introduce three novel motion estimation techniques to determine the unknown cardiac local MVF required to perform an MC reconstruction.

First, a novel MC iterative CT reconstruction method is presented. Subsequently, a number of motion estimation methods are proposed. The first method needs of an initial precomputed 4D ECG-gated image data set and a limited number of manually indicated anatomical point landmarks in order to determine the MVF of a chosen cardiac ROI. Second, a semi-automatic coronary artery motion estimation technique with minimal user interaction is proposed, selecting a single pair of coronary artery points in one frame only. Subsequently, a minimum cost path-based approach is used to extrapolate a multi-phase coronary centerline which is used to determine the unknown MVF. Third, a fully-automatic non-rigid registration-based local motion estimation method is proposed to determine the unknown MVF of a selected cardiac ROI.

A brief summary of the chapters is provided below.

In **Chapter 2**, a new three-dimensional method to reconstruct moving objects from cone-beam X-ray projections using an iterative reconstruction algorithm and a given motion vector field is introduced. For the image representation, volume-adapted spherically symmetric basis functions (blobs) are used which can be implemented efficiently as basis functions. A novel method to calculate line integrals through volume-adapted blobs is proposed which takes also the motion induced blob-size change into account. A phantom data validation of this new MC iterative approach is presented, and an image quality comparison with a non-motion compensated iterative method and an MC FBP reconstruction approach is given.

In **Chapter 3**, a novel method for motion compensated iterative CT reconstruction of a cardiac region of interest is presented. As basic reconstruction method a statistical iterative approach is chosen. The 4D motion field used during reconstruction is obtained from a 3D thin-plate spline warping of a limited number of manually indicated anatomical landmarks of the right coronary artery. Results based on two clinical data sets at strongest motion phases are visually and quantitatively compared to results achieved using a standard gated iterative reconstruction. Moreover comparisons with an MC FBP reconstruction method are made.

In **Chapter 4**, a new method which combines iterative computed tomography reconstruction and coronary centerline extraction techniques to obtain motion artifact-free reconstructed images of the coronary arteries is proposed and evaluated. The method relies on motion-vector fields derived from a set of coronary centerlines extracted at multiple cardiac phases within the RR interval. Hereto, start and end points are provided by the user in one time-frame only. The performance of the method is validated on three patients, and an image quality comparison with the results achieved by a classical gated iterative method is given. Finally, the results are also compared to the manual coronary artery motion estimation method introduced in the previous chapter.

In **Chapter 5**, a novel method for motion-corrected iterative CT reconstruction of a cardiac region of interest is proposed. Given a precomputed (non-motion compensated) gated 4D ROI image data set, a fully automatic elastic image registration is applied to recover a dense cardiac displacement field of the ROI from a chosen cardiac reference phase to a number of phases within the RR interval. Here, a stochastic optimizer and multi-resolution approach are adopted to speed up the

registration process. The method is evaluated on phantom data and in four clinical data sets at strong cardiac motion phases. Results are compared with standard gated iterative reconstruction. A qualitative and quantitative accuracy study is presented for the estimated cardiac motion field.

Motion-compensated iterative cone-beam CT image reconstruction with adapted blobs as basis functions

I can calculate the motion of heavenly bodies, but not the madness of people.

— ISAAC NEWTON (1642 – 1727)

Abstract — This chapter presents a three-dimensional method to reconstruct moving objects from cone-beam X-ray projections using an iterative reconstruction algorithm and a given motion vector field. For the image representation, adapted blobs are used, which can be implemented efficiently as basis functions. Iterative reconstruction requires the calculation of line integrals (forward projections) through the image volume, which are compared with the actual measurements to update the image volume. In the existence of a divergent motion vector field, a change in the volumes of the blobs has to be taken into account in the forward and back-projections. An efficient method to calculate the line integral through the adapted blobs is proposed. It solves the problem, how to compensate for the divergence in the motion vector field on a grid of basis functions. The method is evaluated on two phantoms, which are subject to three different known motions. Moreover, a motion-compensated filtered back-projection reconstruction method is used. Using the correct motion vector field within the iterative motion-compensated reconstruction method, sharp images are obtained, with a quality that is significantly better than gated reconstructions.

2.1 Introduction

In cardiac cone-beam computed tomography (CT), a large effort is continuously dedicated to increase scanning speed in order to limit the influence of patient and organ motion. Especially cardiac motion causes artifacts such as blurring and streaks in tomographic images. A variety of algorithms has been proposed in the literature to reduce or compensate for motion artifacts, see [26, 44, 45, 57, 101, 107, 112, 122, 134] and references therein. Most of the correction methods address the calculation of consistent projection data belonging to the same motion state. These data define a subset of all measurements. Reconstruction of another subset leads to a different motion state of the investigated object. For retrospectively gated cardiac cone-beam CT scanning, sophisticated filtered backprojection (FBP) methods have been developed based on different weighting schemes like the Extended Cardiac Reconstruction (ECR) [26], the Extended Parallel Backprojection (EPB) [45] and the Aperture Weighted Cardiac Reconstruction (AWCR) [57]. In addition to the above analytical reconstruction algorithms, also cardiac iterative reconstruction methods have been investigated, such as a modified ART algorithm for gated cardiac CT reconstruction [86].

Overall, the gated cardiac reconstruction methods yield excellent results, not only with respect to processing time and SNR, but also regarding image quality. However, they are limited in their temporal resolution due to the mechanical movement of the gantry. This can lead to a residual motion blurring, especially in the phases of fast cardiac motion. A motion-compensated (MC) reconstruction method can be used to improve the resolution of the reconstructed image and to suppress motion blurring. Blondel et al. in [5] used a precomputed motion vector field to modify the projection operator and calculated an MC reconstruction with ART. The motion induced distortion of the volume leads to a computation of curved line integrals and a change of the voxel volume in the forward projection step. The voxel volume distortion is neglected in Blondel's article. Pack et al. in [92] proposed a dynamic reconstruction method with known motion field, but under the restrictive assumption that the objects of interest have to move according to a continuous and linear motion field. To perform an MC reconstruction, a computation of the motion vector field (MVF) of the moving object is required. For cardiac CT, several cardiac MVF estimation methods have been proposed in literature [5, 43, 98, 124, 136].

Lately, there is a growing interest to use iterative reconstructions for CT data. The main reason for this is that the iterative algorithms allow to include *a priori* knowledge and a noise model in the reconstruction process, which results in a higher signal-to-noise ratio (SNR) of the reconstructed images compared to the analytical reconstruction algorithms [17, 85, 126, 148]. A drawback for iterative techniques is the high computational effort. An important part of the iterative algorithms is the representation of the continuous object, which is scanned with transmission CT. For iterative reconstruction, the continuous object has to be represented with a finite set of coefficients. Spherically symmetric volume elements (blobs) as basis functions for the image representation have many advantages compared with simple cubic voxels or other basis functions, *e.g.* their appearance is independent of the source position [69]. The reconstruction with spherically symmetric basis functions is used in PET re-

construction [15] and in iterative parallel CT image reconstruction [56]. However, a reconstruction of measurements acquired with divergent rays, as recorded with current helical cone-beam CT systems, leads to the question, how the spherically symmetric volume elements have to be sampled correctly. This problem does not appear in a geometry, where the rays are parallel like in PET, or after re-binning CT data to parallel beam geometry. In these cases, the size of the basis functions can be adapted to the sampling of the measurement. For divergent rays, spherically symmetric volume elements, which are close to the source, have a different contribution to forward and back projection than the spherically symmetric volume elements, which have a greater distance from the source. Ziegler et al. [147] presented a method of sampling the spherically symmetric volume elements motivated by the beam geometry of a CT system: due to the divergent ray geometry, the spherically symmetric volume elements are magnified depending on their distance to the source. The convolution of the magnified spherically symmetric volume elements with the sensitive detector areas defines the weights, which are used for the forward and back projection steps. In addition, in [147], also an efficient implementation of such model is presented. However, in case of MC reconstruction, such a model neglects the change of the local blobs density caused by the existence of a divergent MVF. It is shown in this chapter that this leads to an image with streak artifacts. In fact, an MVF with non-vanishing divergence leads to a non-equidistant grid of blobs, hence, the volumes of the blobs and their forward projections on the detector have to be changed. This chapter introduces a new method of sampling the spherically symmetric volume elements by modifying the model discussed above. This new three-dimensional method evaluates spherically symmetric basis functions in combination with a divergent MVF. In short, a blob adaptation is implemented efficiently by changing the blob-size and its forward projection on the detector depending on the neighboring 3D grid points.

This chapter is organized as follows. Section 2.2 describes the used MC iterative algorithm and explains a new method for the line integral calculation. Finally, the phantoms and their motion models used for an experimental validation of the method are described. In Section 2.3, the obtained results are presented. After the discussion of the results in Section 2.4, the conclusions are summarized in Section 2.5.

2.2 Method and materials

2.2.1 Iterative reconstruction using spherically symmetric basis functions

Iterative reconstruction algorithms reconstruct images of transmission CT scans with a large variety of trajectories and detector geometries. A difference or ratio between the measured and calculated forward projection of an intermediate image is determined. It is used to update the intermediate image via back projection. This procedure is repeated, leading to an iterative reconstruction algorithm.

The main part of the model is the representation of the continuous object to be imaged. For the 3D case, the continuous distribution, f , of absorption of the scanned object has to be represented by a finite set of numbers. It is common to represent f

as a function \tilde{f} , which is a sum of basis functions, b , arranged on a regular 3D grid with N equidistant grid points, \vec{x}_i , and reads

$$\tilde{f}(\vec{x}) = \sum_{i=1}^N \mu_i b(\vec{x} - \vec{x}_i), \quad (2.1)$$

where $N = N_x N_y N_z$ and N_x , N_y and N_z , are the number of grid points in the x , y and z direction, respectively. The set of numbers μ_i are the coefficients of expansion which describe the function \tilde{f} relative to the chosen basis set $b(\vec{x} - \vec{x}_i)$. The choice of the basis functions and the way they are used in forward and backward projections have an influence on the image quality and was investigated previously [69]. In the reconstructions presented in this chapter, the Kaiser-Bessel basis functions [68] are used. These spherically symmetric basis functions (also called blobs [117]) are defined by

$$b_{m,a,\alpha}(r) = \begin{cases} \frac{\sqrt{1-(r/a)^2}^m I_m[\alpha\sqrt{1-(r/a)^2}]}{I_m(\alpha)} & \text{if } 0 \leq r \leq a \\ 0 & \text{else} \end{cases} \quad (2.2)$$

where r is the radial distance from the blob center, I_m denotes the modified Bessel function [141] of order m , a is the radius of the basis function, and α is a parameter controlling the blob shape. In this chapter, the standard parameters are used for the Kaiser-Bessel basis functions defined in (2.2), $m=2$, $a/g=2.00$, and $\alpha=10.4$ with grid increment g . These settings satisfy the frequency criteria described in [76].

Usually, in a CT acquisition system, the detector is discretized in detector pixels j , with $j = (1, 2, \dots, M)$ and $M = VR$ for a total of V projections and R detector pixels in each projection. The forward projection, $\tilde{p}_j^{(n)}$, at iteration, n , can be written for a detector pixel, j , as

$$\tilde{p}_j^{(n)} = \sum_{i=1}^N A_{ji} \mu_i^{(n)}. \quad (2.3)$$

This means, that in the forward projection, the contribution, A_{ji} , of each basis function to the detector pixel, j , has to be determined.

2.2.2 Voxel-dependent footprint

The calculation of the weights, A_{ji} , is an important step in iterative reconstruction. For an ideal rectangular detector pixel, A_{ji} is calculated as the line integral through the basis function b at position \vec{x}_i integrated over the area of the detector pixel j . This can be computed analytically for a given shape of a basis function b and reads

$$A_{ji} = \frac{1}{D} \int_{v_1(j)}^{v_2(j)} \int_{u_1(j)}^{u_2(j)} r(u, v) F[\vec{x}_d(u, v), \vec{x}_s, \vec{x}_i] du dv, \quad (2.4)$$

where

$$F[\vec{x}_d(u, v), \vec{x}_s, \vec{x}_i] = \int_0^1 b[\vec{x}(l, u, v) - \vec{x}_i] dl \quad (2.5)$$

is the so-called "footprint" of the basis function b , $\vec{x}_d(u, v)$ is the detector coordinate parameterized, respectively, by a column u and row v . $\vec{x}(l, u, v) = \vec{x}_s +$

$l[\vec{x}_d(u, v) - \vec{x}_s]$ is the direct line from the X-ray source position, \vec{x}_s , to the detector, $u_1(j)$ ($v_1(j)$) is the column (row) detector position of the lower pixel border of pixel j , $u_2(j)$ ($v_2(j)$) is the corresponding column (row) detector coordinate of the upper pixel border (Fig. 2.3), $D = [u_2(j) - u_1(j)][v_2(j) - v_1(j)]$ is the detector pixel area, and $r(u, v)$ is the detector response. For an idealized detector with a homogeneous response and no dead space between the detector pixels, the detector response would be $r(u, v) = 1$ across the whole detector.

For spherically symmetric basis functions, the line integral calculation in Eq. 2.5 depends only on the distance of the line of integration from the basis function center \vec{x}_i [69]. This footprint calculation ignores the integral over the detector pixel area in Eq. 2.4. Ziegler et al. in [147] present a voxel-dependent footprint calculation. Here, the footprint F , which was introduced in Eq. 2.5 is analytically calculated for a blob. The footprint reduces to the Abel transform [8] of the radial profile $b_{m,a,\alpha}$ and can be expressed as

$$\begin{aligned} F_{m,a,\alpha}[\vec{x}_d(u, v), \vec{x}_s, \vec{x}_i] &= F_{m,a,\alpha}(w_{\vec{x}_d(u,v), \vec{x}_s, \vec{x}_i}) \\ &= 2 \int_0^{(a^2 - w^2)^{1/2}} b_{m,a,\alpha}[(w^2 + t^2)^{1/2}] dt \quad |w| \leq a, \end{aligned} \quad (2.6)$$

where

$$w = w_{\vec{x}_d(u,v), \vec{x}_s, \vec{x}_i} = \sqrt{\|\vec{x}_i - \vec{x}_s\|^2 - \left\{ \frac{(\vec{x}_i - \vec{x}_s) \cdot [\vec{x}_d(u, v) - \vec{x}_s]}{\|\vec{x}_d(u, v) - \vec{x}_s\|} \right\}^2} \quad (2.7)$$

is the perpendicular distance from the center of the blob to the line integral, and t is the distance along the line, such that the radial coordinate, r , of a point on the line is given by $r = (w^2 + t^2)^{1/2}$ [68, 69]. Since $b_{m,a,\alpha}$ is space limited to the ball of radius a , the integral in Eq. 2.6 is defined for $|w| \leq a$, and accordingly the limits of integration are $[0, (a^2 - w^2)^{1/2}]$ instead of $[0, \infty)$.

The footprint in Eq. 2.6 is defined in the coordinate system of a blob with the origin at the blob center. To evaluate the footprint $F_{m,a,\alpha}$ on the detector, a voxel-dependent scaling of the footprint was proposed in [81]. For FBP, a voxel-dependent interpolation kernel, which is similar to a scaling of the footprint, was published recently [16].

The data acquisition geometry with a helical cone-beam CT system can be described as follows. The X-ray source moves on a helical trajectory

$$\vec{x}_s(\gamma) = \left(d_{cs} \cos \gamma, d_{cs} \sin \gamma, \frac{\gamma}{2\pi} p_{abs} \right), \quad (2.8)$$

around the object. The rotation axis coincides with the Z axis. The parameter $\gamma \in [0, 2\pi)$ describes the position of the gantry, d_{cs} is the distance of the center of rotation from the source, the pitch p_{abs} is the absolute table travel per rotation. A focus-centered detector rotates at distance d_{ds} from the X-ray source, i.e., the detector is cylindrical with the X-ray source focus at the axis of the cylinder. This means that the detector is parallel to the rotation axis, Z , and the transaxial plane is defined by

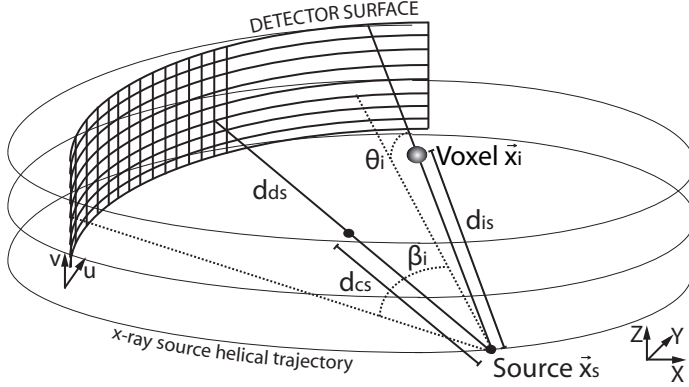


Figure 2.1. A 3D sketch of the acquisition geometry of a focus centered detector with an X-ray source. Here, d_{is} is the distance of the blob i from the source, d_{ds} is the distance of the detector from the source, d_{cs} is the distance of the center of rotation from the source, and θ_i represents the angle between the plane of the gantry and a vector pointing from the source to the blob i .

the X and Y axis. A 2D coordinate system (u, v) is used for the detector. Finally, β_i represents the X-ray source fan angle (Fig. 2.1).

In this focus-centered geometry, and with spherically symmetric basis functions, voxel-dependent scaling of the footprint can easily be performed. It is scaled with a factor $r_\phi(i) = d_{ds} / (d_{is} \cdot \cos \theta_i)$ in the angular direction, and the factor, $r_\zeta(i) = d_{ds} / (d_{is} \cdot \cos^2 \theta_i)$ in the axial direction z (see Fig. 2.1). The footprint of Eq. 2.6 can be evaluated in the detector coordinate system (u, v) . The dependence can be written as

$$\begin{aligned} F_{m,a,\alpha}(w_{\vec{x}_d(u,v), \vec{x}_s, \vec{x}_i}) &= F_{m,a,\alpha}(w_{i,u,v}) \\ &= F_{m,a,\alpha} \left(\sqrt{\left[\frac{u - u_0(i)}{r_\phi(i)} \right]^2 + \left[\frac{v - v_0(i)}{r_\zeta(i)} \right]^2} \right), \end{aligned} \quad (2.9)$$

where $\vec{x}_d[u_0(i), v_0(i)] = d_{ds} \vec{x}_i / (\|\vec{x}_i\| \cdot \cos \theta_i)$ is the coordinate of the center of the volume element i projected on the detector and

$$w_{\vec{x}_d(u,v), \vec{x}_s, \vec{x}_i} = w_{i,u,v} = \sqrt{\{[u - u_0(i)] / r_\phi(i)\}^2 + \{[v - v_0(i)] / r_\zeta(i)\}^2}.$$

As a result of the method described above a blob close to the source has a bigger footprint than a blob close to the detector.

The calculation of the weights requires the evaluation of the footprint as given in Eq. 2.9. This evaluation can be performed by the calculation of the mean of the footprint over the sensitive area of the detector pixel [147], and is expressed with the

scaled footprint in Eq. 2.9 as

$$A_{ji} = L \int_{v_1(j)}^{v_2(j)} \int_{u_1(j)}^{u_2(j)} r(u, v) F_{m,a,\alpha} \left(\sqrt{\left[\frac{u - u_0(i)}{r_\phi(i)} \right]^2 + \left[\frac{v - v_0(i)}{r_\zeta(i)} \right]^2} \right) dudv, \quad (2.10)$$

with $L = 1/\{\int_{-a}^a \int_{-a}^a r(u, v) F_{m,a,\alpha}[(u^2 + v^2)^{1/2}] dudv\}$. Aliasing artifacts due to undersampling of footprints are avoided with this method, independent of the size of the volume elements and the grid increment.

The model in Eq. 2.10 performs well in case of iterative cone-beam CT reconstructions of static objects. However, if an iterative cone-beam CT reconstruction of a moving object (*e.g.*, the heart) has to be performed, this calculation of weights leads to reconstructed images with several motion artifacts. In fact, the calculation of A_{ji} weights in Eq. 2.10 does not take care of the motion of the volume element itself and the change of blobs-volume caused by divergent MVF.

In the following subsection, a new three-dimensional MC iterative reconstruction method is proposed that modifies the model in Eq. 2.10 in order to evaluate blobs in combination with an MVF, where also divergent MVF are investigated and incorporated in the model.

2.2.3 Volume-dependent footprint for motion-compensated iterative reconstruction

The proposed MC iterative reconstruction method needs a set of MVFs between the different time phases. For a cardiac cone-beam CT reconstruction, the MVF can be given by displacement vectors $\vec{m}_i(\vec{x}_i(\phi_r^P), \phi_r^P, \phi)$ of the corresponding grid position $\vec{x}_i(\phi_r^P)$ from a reference heart phase ϕ_r^P to a new grid position $\vec{x}_i^*(\phi)$ in an arbitrary heart phase ϕ (Fig. 2.2) by

$$\vec{x}_i^* = \vec{x}_i^*(\phi) = \vec{x}_i(\phi_r^P) + \vec{m}_i(\vec{x}_i(\phi_r^P), \phi_r^P, \phi). \quad (2.11)$$

Inserting the MVF of Eq. 2.11 into Eq. 2.1 and Eq. 2.10 yields

$$\tilde{f}^*(\vec{x}) = \sum_i \mu_i b(\vec{x} - \vec{x}_i^*) \quad \text{and} \quad (2.12)$$

$$A_{ji}^* = L \int_{v_1(j)}^{v_2(j)} \int_{u_1(j)}^{u_2(j)} r(u, v) F_{m,a,\alpha} \left(\sqrt{\left[\frac{u - u_0^*(i)}{r_\phi^*(i)} \right]^2 + \left[\frac{v - v_0^*(i)}{r_\zeta^*(i)} \right]^2} \right) dudv, \quad (2.13)$$

where $\vec{x}_d[u_0^*(i), v_0^*(i)] = d_{ds}\vec{x}_i^*/(\|\vec{x}_i^*\| \cdot \cos\theta_i^*)$ is the modified coordinate of the center of the volume element i projected on the detector, $r_\phi^*(i) = d_{ds}/(d_{is}^* \cdot \cos\theta_i^*)$ the modified scaling factor in angular direction with d_{is}^* the modified distance of blob i from the source, $r_\zeta^*(i) = d_{ds}/(d_{is}^* \cdot \cos^2\theta_i^*)$ the modified scaling-ratio in axial direction z , and θ_i^* the modified angle between the plane of the gantry and a vector pointing from the source to the modified position of voxel i . In case of a non divergence-free MVF, the movement of the equidistant \vec{x}_i centers of the basis functions in different

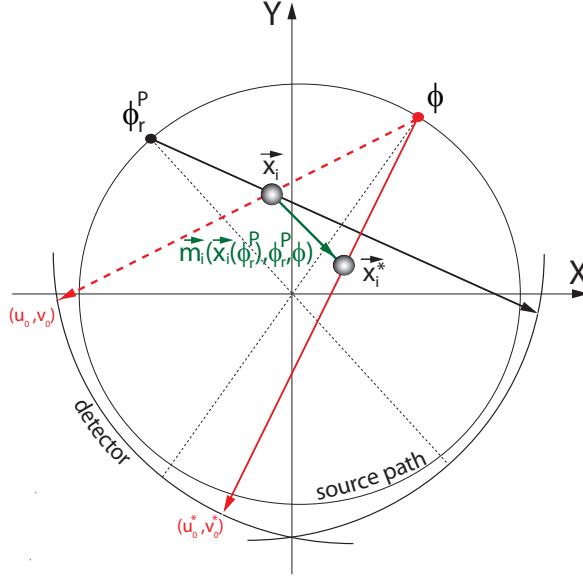


Figure 2.2. The MVF applied at the blob position x_i . The green vector represents the displacement vector $\vec{m}_i(\vec{x}_i(\phi_r^P), \phi_r^P, \phi)$ of the corresponding grid position $\vec{x}_i(\phi_r^P)$ from a reference heart phase ϕ_r^P to a new grid position $\vec{x}_i^*(\phi)$ in an arbitrary heart phase ϕ , the black line represents the line integral through the blob at grid position \vec{x}_i in the reference heart phase ϕ_r^P , the red line represents the new correct line integral through the blob at new grid position \vec{x}_i^* in an arbitrary heart phase ϕ , and finally the dashed red line is the wrong line integral calculated through the blob at the wrong grid position \vec{x}_i in an arbitrary heart phase ϕ .

directions causes a non-equidistant grid of positions \vec{x}_i^* . Therefore, the volume of each blob, and consequently also their footprints on the detector, have to be changed (Fig. 2.3). The calculation of weights in Eq. 2.13 does not take care of the change of the volumes of blobs, which leads to incorrect image reconstructions with several streak artifacts as will be shown in the results section. A volume-dependent adaptation of the blob-footprint is needed to compensate for this effect.

A two step method that approximates the change of the blob-footprint is proposed. First, the width of the blob is changed depending on the neighboring grid points. A good approximation is the adaptation of the width of the i^{th} basis function by the factors

$$r_x(i) = \frac{x_{i+1}^* - x_{i-1}^*}{x_{i+1} - x_{i-1}} \quad (2.14)$$

$$r_y(i) = \frac{y_{i+N_x}^* - y_{i-N_x}^*}{y_{i+N_x} - y_{i-N_x}} \quad (2.15)$$

$$r_z(i) = \frac{z_{i+N_x N_y}^* - z_{i-N_x N_y}^*}{z_{i+N_x N_y} - z_{i-N_x N_y}}, \quad (2.16)$$

in the X , Y and Z direction. x_i , y_i , and z_i are the x -, y -, z -coordinates of the i^{th} grid point. x_i^* , y_i^* and z_i^* are the x -, y -, z -coordinates of the i^{th} grid point after applying the MVF (Fig. 2.3).

Actually, a precomputed Voronoi tessellation [91,139] should be used in order to calculate exactly the adaptation ratios of the width of each blob of the grid. However, the proposed adaptation method permits a very fast calculation of the approximated blob-width adaptation factors during the reconstruction process without any additional precomputation loads.

In a second step, the ratio of the footprint of the i^{th} blob before and after the adaptation is calculated depending on the actual source and detector position. This can be performed for spherically symmetric basis functions by calculating

$$r_f(i) = \sqrt{\left(r_x^2(i) \cos^2(\varphi_i^*) + r_y^2(i) \sin^2(\varphi_i^*)\right) \cos^2(\theta_i^*) + r_z^2(i) \sin^2(\theta_i^*)}, \quad (2.17)$$

where φ_i^* is the angle in the XY -plane between the X -axis and the line going through the X -ray source and the modified center of the i^{th} basis function (Fig. 2.3). A volume-dependent adaptation of the blob-footprint with the factor $r_f(i)$ leads to a footprint in the coordinate system of a blob with the origin at the blob center, that takes care of the divergence of the MVF. Moreover, a similar volume-dependent adaptation is needed to assess the change of the blob-footprint over the detector pixel. This is achieved by scaling the width of the footprint of the i^{th} basis function in the detector coordinate system by the factors

$$r_u(i) = \sqrt{r_x^2(i) \sin^2(\varphi_i^*) + r_y^2(i) \cos^2(\varphi_i^*)} \quad (2.18)$$

$$r_v(i) = r_z(i), \quad (2.19)$$

in the u and v direction respectively (Fig. 2.3). Finally, the weight calculation in Eq. 2.13 becomes

$$A_{ji}^s = r_f(i)L \int_{v_1(j)}^{v_2(j)} \int_{u_1(j)}^{u_2(j)} r(u,v) F_{m,a,\alpha} \left(\sqrt{\left[\frac{u - u_0^*(i)}{r_\phi^*(i) r_u(i)} \right]^2 + \left[\frac{v - v_0^*(i)}{r_\zeta^*(i) r_v(i)} \right]^2} \right) dudv, \quad (2.20)$$

where A_{ji}^s are the new volume-dependent weights to use for calculating the forward projections in Eq. 2.3.

The chapter presents an MC iterative 3D CT reconstruction method with main proposed application in cardiac CT. Using the *a priori* knowledge that smoothness and regularity are constraints that most organic objects in this world are subject to, it makes sense to require the given MVF to be regular and smooth. For the regularity constraint, all the i^{th} grid points have to satisfy the following spatial conditions before and after an MVF is applied:

$$\begin{cases} x_{i-1} < x_i < x_{i+1} \\ y_{i-N_x} < y_i < y_{i+N_x} \\ z_{i-N_x N_y} < z_i < z_{i+N_x N_y}, \end{cases} \quad (2.21)$$

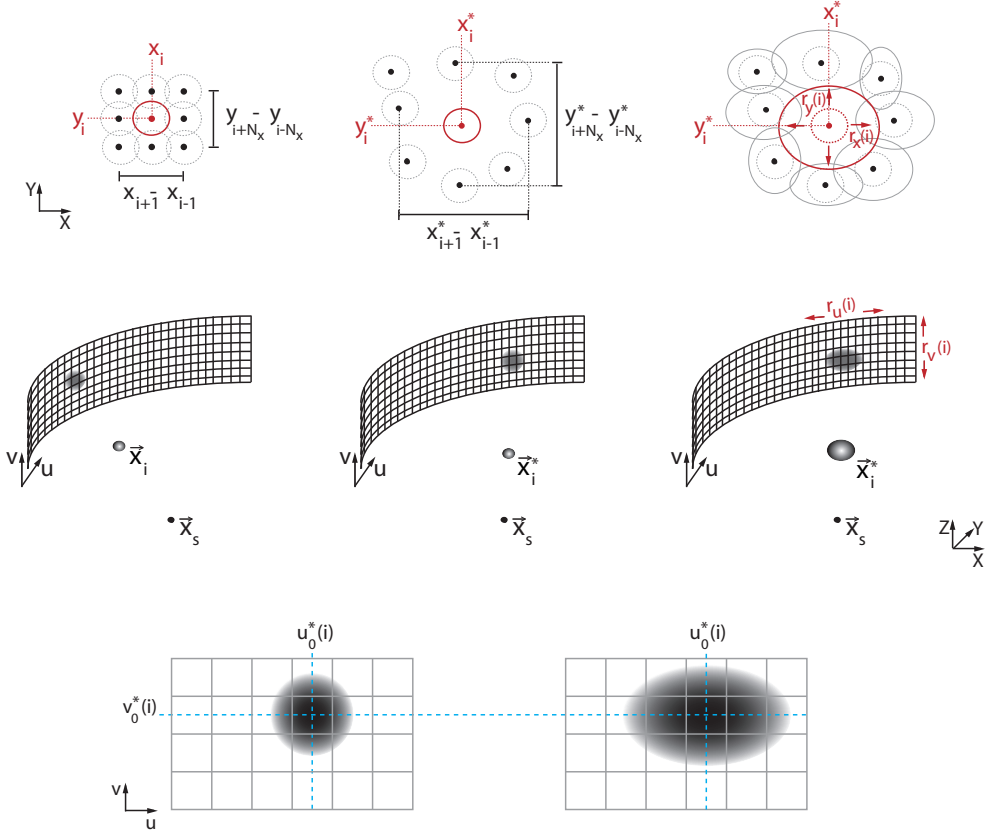


Figure 2.3. Sketch of the volume-dependent adaptation of the footprint of a blob in a focus-centered detector geometry. In the top row, the blob i , in a regular grid (left), in a non-equidistant grid after applying a divergent MVF (center), and in a non-equidistant grid after applying a divergent MVF and a volume-dependent adaptation of its footprint (right), are sketched. In the middle row, the corresponding density plots of the footprints of this blob on the detector are shown. In the bottom row, a zoom of the footprint of the blob i on the detector after applying a divergent MVF (left), and after applying a divergent MVF and a volume-dependent adaptation of its footprint (right), are shown. Here, the center of the footprint on the detector is at position $[u_0^*(i), v_0^*(i)]$.

this means that the three blob-width ratios r_x , r_y , and r_z in Eq. 14, Eq. 15 and Eq. 16 will be always strictly positive, otherwise the given irregular MVF will lead to non-anatomical motions. In short, the divergent MVF can expand or reduce the volume of the blobs but never delete one or more of them.

2.2.4 Motion-compensated image reconstruction with cardiac gated SART

The Simultaneous Algebraic Reconstruction Technique (SART) [4] is used for investigating the volume-adapted weights calculation. However, this model can be applied to any iterative reconstruction algorithm such as the ART [25] or Maximum Likelihood [60] methods. The SART is a commonly used modification of ART, which increases the reconstruction speed. Here, an entire cone-beam projection is back projected into the image. In the ART method, the backprojection step of iteration n , the difference between the calculated projection, $\tilde{p}_j^{(n)}$, and the measured projection, p_j , is used to update the coefficient, $\mu_i^{(n)}$ using the following equation

$$\mu_i^{(n+1)} = \mu_i^{(n)} + \lambda_n \frac{p_j - \tilde{p}_j^{(n)}}{\sum_i a_{ji}^2} a_{ji}, \quad (2.22)$$

where the relaxation parameter, $0 < \lambda_n < 2$, controls the speed of convergence.

Here, the backprojection does not have a voxel-dependent contribution that scales with the distance of a voxel to the source and detector, or with the voxel volume. The weights, a_{ji} , are chosen to be

$$a_{ji} = A_{j,i}^s / [r_\phi^*(i) r_\zeta^*(i) r_f(i) r_u(i) r_v(i)]. \quad (2.23)$$

In helical cone-beam CT, projections are usually truncated in the direction of the rotation axis [58]. This truncation leads to artifacts in iterative helical cardiac cone-beam reconstructions. The problem can be solved by introducing an aperture weight, w_j^a , for each detector pixel, j , in the back projection as has been used for FBP reconstructions [57]. The aperture weighting function is the same for all projections and only depends on the distance of a detector pixel, j , from the XY -plane defined by the source position. For the reconstructions presented in this work, a \cos^2 aperture weighting function is used, which reads

$$w_j^a = \begin{cases} \cos^2 \left(\frac{qH - (z_d^+ - z_j)}{H(q+1)} \frac{\pi}{2} \right), & z_d^+ - qH \leq z_j \leq z_d^+ + H \\ 1, & z_d^- + qH \leq z_j \leq z_d^+ - qH \\ \cos^2 \left(\frac{qH - (z_j - z_d^-)}{H(q+1)} \frac{\pi}{2} \right), & z_d^- - H \leq z_j \leq z_d^- + qH \\ 0, & \text{else} \end{cases} \quad (2.24)$$

where H is the height of a detector pixel, z_d^+ (z_d^-) is the axial coordinate of the detector end in the positive (negative) axial direction, z_j is the axial coordinate of the detector pixel j , and q is the number of rows on each side that are furnished with an aperture weight. An example of the aperture weight of a blob on the rotation axis is shown in Fig. 2.4.

If an iterative cardiac-gated reconstruction has to be performed, an additional cardiac gating window weight, w_j^c , is introduced for each projection p_j , in the reconstruction algorithm in order to select data belonging to the same heart phase. A list of N_r R-peaks at angular CT system positions ϕ_k^R is determined from the patient's electrocardiogram (ECG) recorded synchronously with the projection data,

these angular positions are converted to the corresponding projection indices that were recorded at these angles. From the list of R-peaks, the centers ϕ_k^P of the gating windows, the so-called phase points, can be determined using, for example, a fixed percentage $P \in [0, 1)$ of the RR interval. The same percentage is used for all heart cycles (Fig. 2.4).

$$\phi_k^P = \phi_k^R + P (\phi_{k+1}^R - \phi_k^R) \quad \forall k = 1, \dots, N_p. \quad (2.25)$$

$N_p = N_r - 1$ phase points are obtained. A gating function with a width w_k is centered at each phase point ϕ_k^P . The width w_k of the gating function determines the amount of projection data used from each cycle for the reconstruction and primarily determines the temporal resolution. It can be used to balance motion blurring, SNR, and artifact level.

In this work, an optimized window width [86] is used. It guarantees an optimal temporal resolution since only the data from the smallest possible gating window around a phase point are used for the reconstruction. The effect of various gating function shapes on the images quality has been investigated in [86]. For the 3D reconstructions presented in this chapter, a rectangle with smooth edges (bump shape) is used for the cardiac-gated reconstructions, and reads

$$\text{bump}_\nu(j, \phi_k^P, w_k) = \begin{cases} 1, & |j - \phi_k^P| \leq (1 - \nu) \frac{w_k}{2} \\ \frac{1}{2} \left[1 - \sin \left(\frac{\pi}{w_k \nu} \left(|j - \phi_k^P| - \frac{w_k}{2} \right) \right) \right], & \left| \frac{2|j - \phi_k^P| - w_k}{2} \right| < \frac{w_k \nu}{2} \\ 0, & \text{else} \end{cases} \quad (2.26)$$

j is the index of a projection, $\nu \in [0, 1]$, the bump shape has non-zero values on an interval of $(1 + \nu) w_k$. Where w_k is the full width at half maximum of the bump shape.

For all heart cycles, the cardiac weighting function w_j^c can be written as

$$w_j^c = \sum_{k=1}^{N_p} \text{bump}_\nu(j, \phi_k^P, w_k). \quad (2.27)$$

One update of the SART algorithm requires to sum simultaneously over all the projections in one subset S_m . The projections in the subsets have a constant angular increment inside each gating window, and the order of the subsets is determined randomly. A random sequence is used because it was found to perform very similar to more sophisticated ordering schemes like the one proposed in [28]. With the selection of ordered subsets, and using the cardiac and the aperture weighting functions shown above, the SART method becomes an ECG-gated aperture weighted SART (gated AWSART) method, which can be written as

$$\mu_i^{(n+1)} = \mu_i^{(n)} + \frac{\lambda_n}{\sum_{j \in S_m} a_{ji} w_j^c w_j^a} \sum_{j \in S_m} \frac{p_j - \tilde{p}_j^{(n)}}{\sum_i a_{ji}} a_{ji} w_j^c w_j^a. \quad (2.28)$$

In our experiments the $\text{bump}_{0.4}$ shape has been used, because this shape gives little motion blurring while suppressing streaks efficiently at the same time [86].

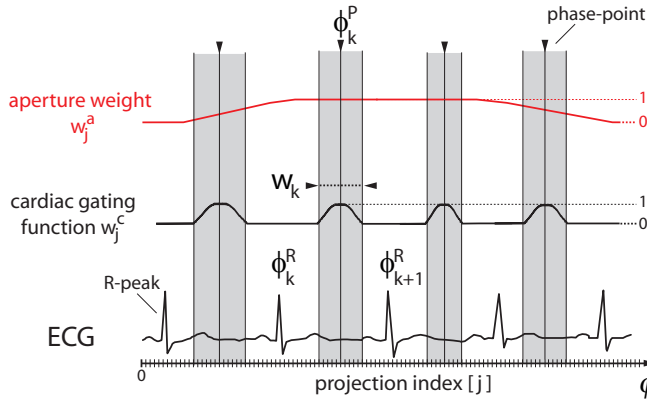


Figure 2.4. The aperture weight w_j^a of a blob on the rotation axis and the cardiac gating function w_j^c . Only the projections inside the gray intervals are used for the iterative cardiac-gated image reconstruction.

2.2.5 Software phantoms and simulations

In order to demonstrate the feasibility of the MC iterative reconstruction with the proposed volume-dependent footprint calculation, two phantoms are subjected to three different motion trajectories. The first phantom consists of a bone sphere inside a bigger concentric water sphere, the center of the spheres is placed at the origin. Instead, the second phantom consists of two concentric bone spheres with different radius and absorption density, placed inside a bigger water sphere. For the first phantom, two different motion model are used. The two applied trajectories are a cyclic diagonal translation of the two spheres (Fig. 2.5(a)), i.e., all the grid points move identically along a diagonal in all directions in space, so a divergence free MVF is produced; and a cyclic change of the radius of the bone sphere (Fig. 2.5(b)), i.e., the total volume stays constant, but the water and bone sphere volume depend on time. This second motion leads to a divergent MVF. The phantom with cyclic diagonal translation of the two spheres (Fig. 2.5(a)) is an approximation of the cardiac motion of the coronary arteries which is dominated by a 3D translation (Fig. 2.6(a)). While the phantom with the cyclic change of the radius of the bone sphere (Fig. 2.5(b)) is an approximation of the volume of contrast agent change within a chamber of the heart (Fig. 2.6(b)). Finally, for the second phantom a more complex asymmetric motion trajectory is applied. It consists to a cyclic diagonal translation of the two inner bone spheres, with a contemporaneous cyclic change of the radius of the smaller bone sphere (Fig. 2.5(c)). Even this third motion is divergent due to the pulsation motion of the smaller bone sphere. The used cyclic motion-model is a simple sinusoidal movement, and its chosen cycle time corresponds to a heart rate of 64 beats per minute (bpm). The MVF for the three cases are known exactly (in Fig. 2.7, the MVF components for the phantom with motion trajectory in Fig. 2.5(c) are shown). For the image acquisition, a simulated helical cone-beam CT scanner with assumed point-like

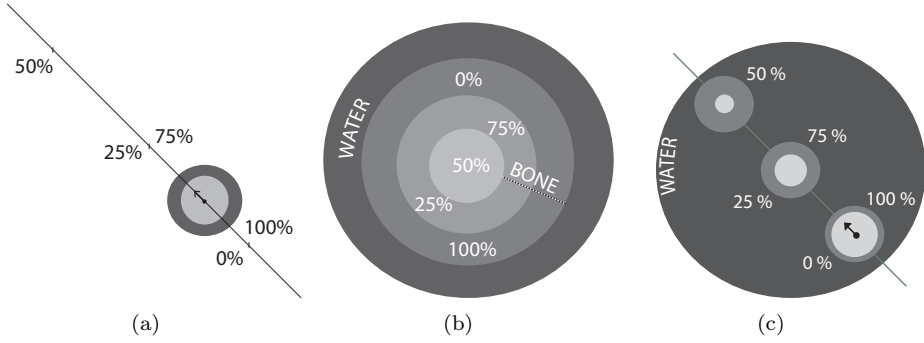


Figure 2.5. The three trajectories used in this work for the phantoms study. (a) describes the cyclic diagonal translation of the two spheres, (b) describes the cyclic change of the radius of the bone sphere, while (c) describes the cyclic diagonal translation of the two inner bone spheres, with a contemporaneous cyclic change of the radius of the smaller bone sphere. The percentages indicate the different phase points inside the motion period. The first motion trajectory leads to an homogeneous MVF, instead the second and the third trajectories lead to a divergent MVF.

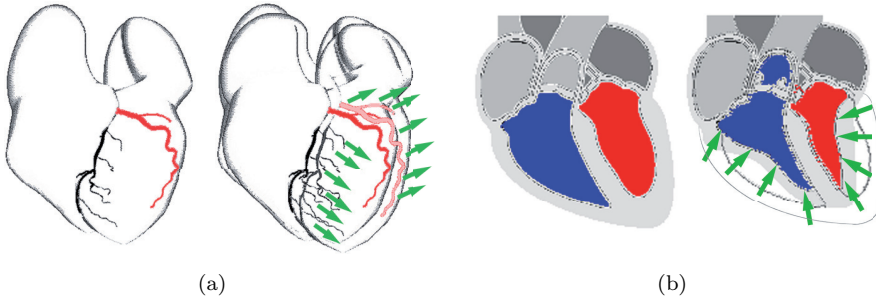


Figure 2.6. Sketch of a divergent and non-divergent MVF in a beating heart. (a) shows the systolic motion (left) and the systolic and diastolic motions superimposed (right), of the coronary arteries. This motion is dominated by a 3D translation, and the relative MVF can be considered non-divergent. Instead, (b) shows the ventricular diastole (left) and the ventricular diastole and systole motions superimposed (right). The volume of contrast agent change within the right (blue) and left ventricles (red) can lead to a divergent motion. The green arrows represent the MVFs of the two motion cases.

X-ray source is used. Moreover, the same reconstructions are performed with noisy measurements, and the noisy projection data sets are supplied with a Poisson noise in such a way that a non attenuated ray deposits $3.0 \cdot 10^5$ photons per projection angle in each detector element. Finally, the phantoms are reconstructed at a phase point of 25% which is the phase of highest motion. In Table 2.1 all the phantoms and simulation parameters are summarized.

	Phantom in Fig. 2.5(a), 2.5(b)		Phantom in Fig 2.5(c)	
Trajectories	Sine amplitude	4 mm	Sine amplitude (pulsation)	3 mm
	Sine cycle time	64 bpm	Sine ampl. (translation)	6 mm
	# motion cycles	13	Sine cycle time	64 bpm
Materials			# motion cycles	13
	Bone sphere radius	15 mm	Small bone sphere radius	10 mm
	Water sphere radius	25 mm	Big bone sphere radius	16 mm
	Bone sphere density	700 HU	Water sphere radius	34 mm
			Small bone sphere density	700 HU
AWSART recon.			Big bone sphere density	350 HU
	# subsets	90	# subsets	90
	# views per subset	100	# views per subset	100
	# iterations	30	# iterations	20
	λ	0.8	λ	0.8
Helical CT scanner	Cubic grid size	0.47 mm ³	Cubic grid size	0.47 mm ³
	# Detector rows	16	# Detector rows	16
	# Detector columns	672	# Det. columns	672
	Rotation time	0.42 s	Rotation time	0.42 s
	Detector height	21.9 mm	Detector height	21.9 mm
	d_{cs}	570 mm	d_{cs}	570 mm
	d_{cd}	470 mm	d_{cd}	470 mm
	Pitch	2.88 mm	Pitch	2.88 mm
	# views per turn	1160	# views per turn	1160
	# rotations	30	# rotations	35

Table 2.1. Parameters for the simulations. The d_{cd} describes the distance of the center of rotation from the focus-centered detector.

2.3 Results

For reasons of comparison, MC gated AWSART reconstructions with and without the proposed volume-dependent adaptation of the blobs-footprint are performed for the phantoms subject to divergent and divergent-free motion in Fig. 2.5, and the results are presented in Fig. 2.8 and Fig. 2.9. Moreover, a reconstruction with the MC aperture weighted cardiac reconstruction (MC AWCR) method [136] is presented as

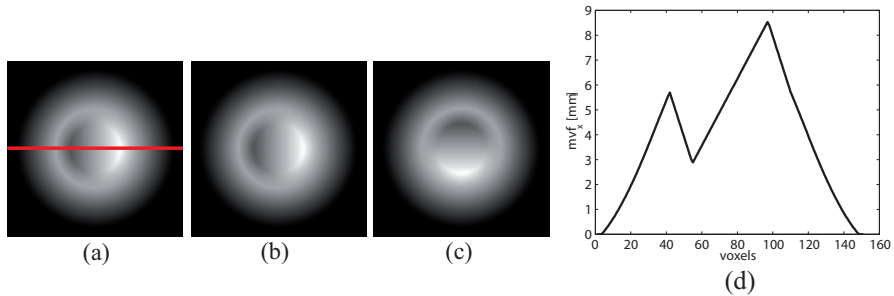


Figure 2.7. The divergent MVF for the phantom with asymmetric motion in Fig. 2.5(c). The MVF presented above is relative to the motion between the reference phase point of 25% and the phase point of 5%. In (a) the x-component (coronal view), in (b) the y-component (axial view), and in (c) the z-component (coronal view) of the MVF are shown, respectively. The red line in (a) indicates the mvf_x values, which are shown in (d).

well. The reconstructed images are shown in Fig. 2.10 and Fig. 2.11. In Table 2.2 and 2.3, image quality measures of the reconstructed images in Fig. 2.8 and Fig. 2.10 are presented. In details, in Table 2.2, the mean absolute difference (MAD) and the normalized correlation coefficient (NCC) computed between the phantoms images (at 25% RR) and the reconstructed images with and without the proposed volume-dependent adaptation of the blobs-footprint are presented. These are given as

$$MAD = \frac{1}{N} \sum_{i=1}^N |\mu_i^{Re} - \mu_i^{Ph}|, \quad (2.29)$$

$$NCC = \frac{\sum_{i=1}^N [(\mu_i^{Re} - \bar{\mu}^{Re})(\mu_i^{Ph} - \bar{\mu}^{Ph})]}{\sqrt{\sum_{i=1}^N (\mu_i^{Re} - \bar{\mu}^{Re})^2} \sqrt{\sum_{i=1}^N (\mu_i^{Ph} - \bar{\mu}^{Ph})^2}} \cdot 100\%, \quad (2.30)$$

where μ_i^{Re} and μ_i^{Ph} represent the absorption coefficients at the i^{th} grid point in the reconstructed images and in the phantom, respectively, and $\bar{\mu} = \sum_{i=1}^N \mu_i / N$. A MAD (NCC) close to 0 (100%) means that the two volumes have a very high similarity. Furthermore, even the mean and the standard deviation (STD) values measured inside a homogeneous bone region are shown. In Table 2.3, the same image quality measures are computed between the phantoms images (at 25% RR) and the gated AWSART, the gated MC AWSART, and the MC AWCR images are presented. Finally, the results of the reconstructions performed with noisy measurements are shown in Fig. 2.12 and Fig. 2.13.

Motion Vector Field	Method	MAD [HU]	NCC [%]	Mean[\pm STD] [HU]
No diverg. (Fig. 2.5(a))	MC gat. AWSART _{nvs}	25.76	99.38	700.92[\pm 0.17]
	MC gated AWSART	25.76	99.38	700.92[\pm 0.17]
Divergent (Fig. 2.5(b))	MC gat. AWSART _{nvs}	34.99	98.94	676.27[\pm 23.27]
	MC gated AWSART	26.20	99.10	703.03[\pm 0.51]
Divergent (Fig. 2.5(c))	MC gat. AWSART _{nvs}	49.95	99.20	607.17[\pm 5.98]
	MC gated AWSART	35.09	99.35	708.47[\pm 1.22]

Table 2.2. Image quality measures. The mean absolute difference (MAD) and the normalized correlation coefficient (NCC) between the phantoms images and the reconstructed images with (MC gated AWSART) and without (MC gat. AWSART_{nvs}) the proposed volume-dependent adaptation of the blobs-footprint shown in Fig. 2.8 are presented, respectively. Furthermore, the mean and the standard deviation values are calculated inside the red circles in Fig. 2.8.

2.4 Discussion

The proposed volume-adapted calculation of weights takes care of the change of the blobs volume. The divergent MVF is incorporated in the model and the images reconstructed are streak artifact free (Fig. 2.8(f),(h),(j) and (l)). This can also be derived from the line scans presented in Fig. 2.9(a) to (f), where the reduction of Hounsfield value variation is visualized for homogeneous phantom areas. In Fig. 2.8(a) to (d), the images reconstructed with and without the blob-volume adaptation for the case

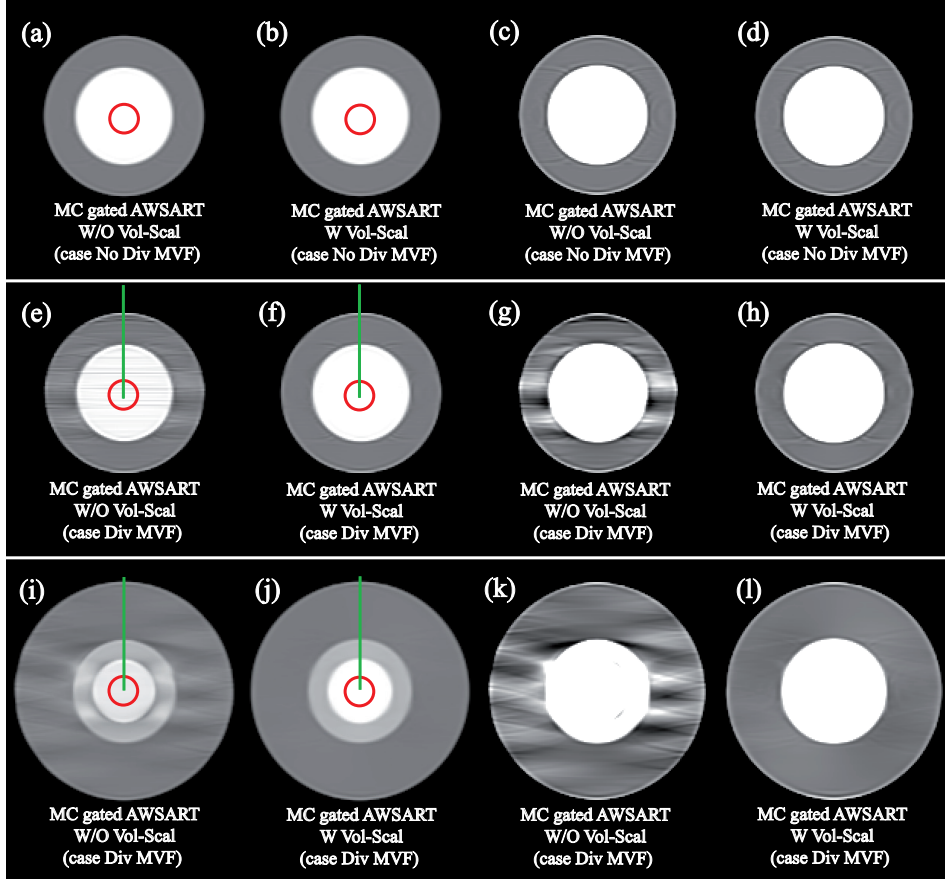


Figure 2.8. Coronal view of the MC gated AWSART reconstructed images (at 25% phase point) with (W) and without (W/O) the proposed volume-dependent adaptation of the blobs-footprint performed for the phantom with divergent-free (top row) and divergent (middle and bottom rows) MVF. The green lines indicate the μ -values, which are shown in Fig. 2.9. The red circles indicate the homogeneous bone region used for the computation of the image quality measures listed in Table 2.2. In (a), (b), (e), (f), (i) and (j) the images are shown with Level=0 HU and Window=1400 HU, instead in (c), (d), (g), (h), (k) and (l) the same images are shown with Level=0 HU and Window=300 HU.

of divergent-free MVF are shown. As discussed before, the divergent-free MVF, does not change the grid geometry, therefore the volume of each blob does not change. Our method of volume-adapted calculation of weights takes care of this, in fact all the compensation factors in Eq. 2.17, Eq. 2.18 and Eq. 2.19 are unity in case of divergent-free MVF applied on the grid. Hence, for phantom subject to divergent-free motion, to use

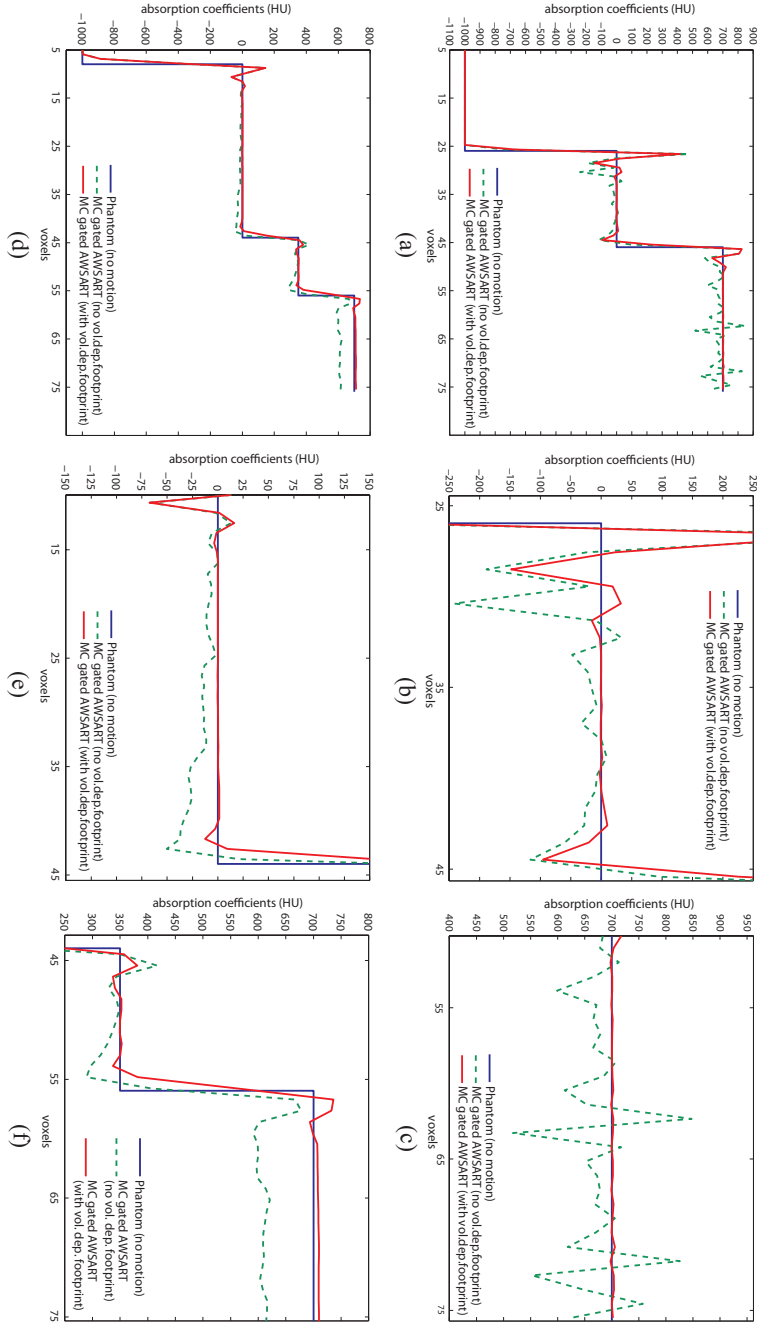


Figure 2.9. Absorption coefficients of the MC gated AWSART reconstructed images with and without the proposed volume-dependent adaptation of the blobs-footprint performed for the phantoms with divergent MVF, respectively, along the lines indicated in Fig. 2.8(e) and in Fig. 2.8(f) (top row), and along the lines indicated in Fig. 2.8(i) and in Fig. 2.8(j) (bottom row). In order, on the top row, in (a) the half phantom profile is shown, in (b) a close-up of the water region (0 HU) is shown, and in (c), a close-up of the bone region (700 HU) is shown. While, on the bottom row, in (d) the half phantom profile is shown, in (e) a close-up of the water region (0 HU) is shown, and in (f), a close-up of the bone spheres region (350, 700 HU) is shown.

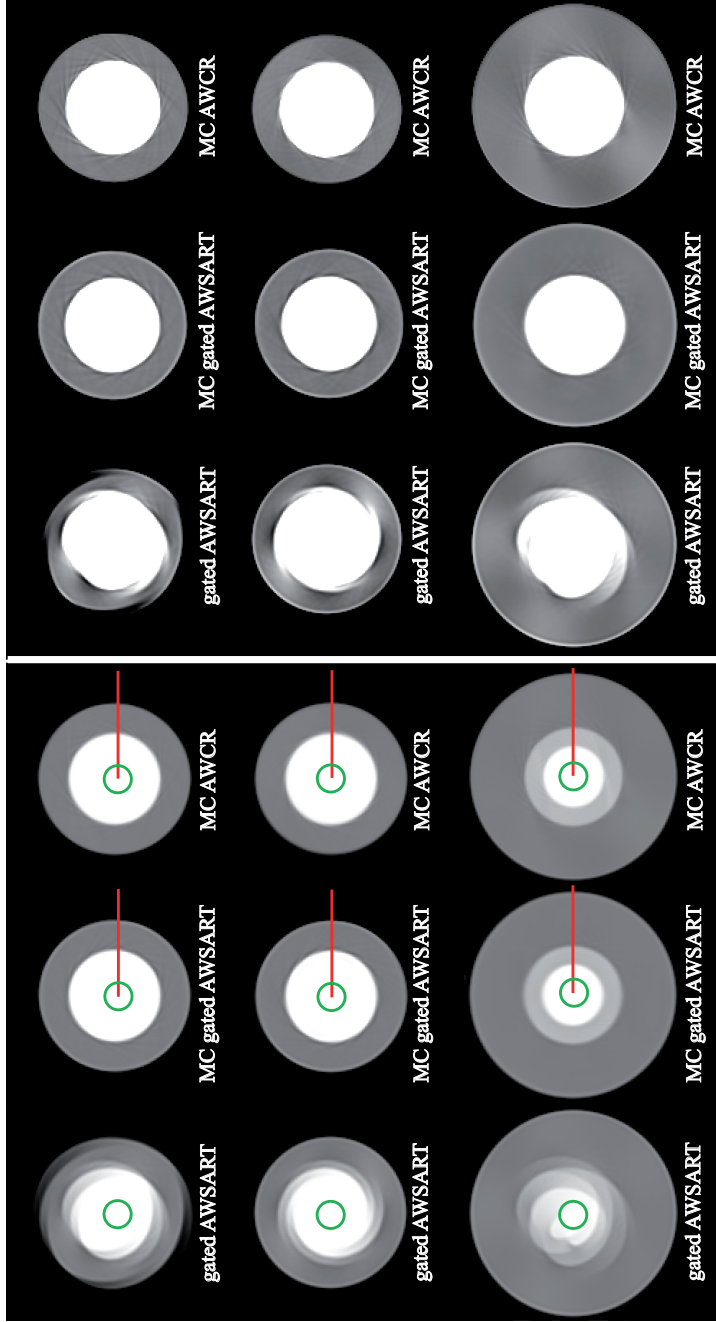


Figure 2.10. Axial view of the reconstructed images (at 25% phase point) of the phantom subject to a cyclic diagonal translation motion (top row), to a cyclic change of the radius of the bone sphere (middle row), and to a cyclic diagonal translation and pulsation motions (bottom row). On the left side the images are presented with Level=0 HU and Window=1400 HU, while on the right side the same images are presented with Level=300 HU. In order, on each row, the images are presented reconstructed with the gated AWSART method (left), the MC gated AWSART method (center), and with the MC AWCRC method (right). The red lines indicate the μ -values, which are shown in Fig. 2.11. The green circles indicate the homogeneous bone region used for the computation of the image quality measures listed in Table 2.3.

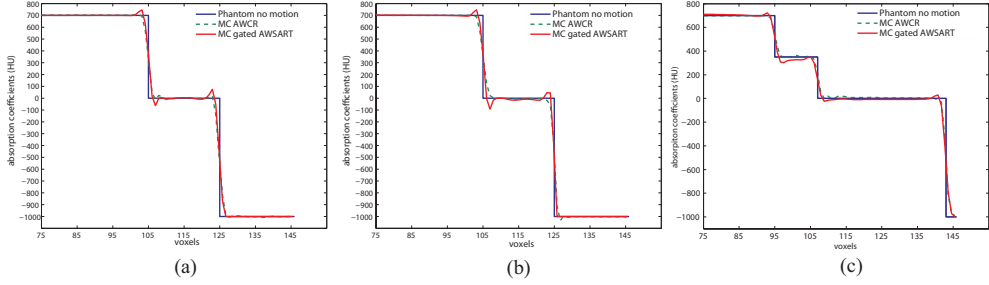


Figure 2.11. Absorption coefficients of the phantom without motion, of the MC AWCR reconstructed image, and of the MC gated AWSART reconstructed image, respectively, along the red lines indicated in Fig. 2.10. In figure (a), the absorption coefficients for the case of the phantom with a cyclic diagonal translation motion are shown, in figure (b), the absorption coefficients for the case of the phantom with a cyclic change of the radius of the bone sphere are shown, while in figure (c) the absorption coefficients for the case of the phantom with a cyclic diagonal translation and a pulsation motions are shown.

Motion Vector Field	Method	MAD [HU]	NCC [%]	Mean[\pm STD] [HU]
No diverg. (Fig. 2.5(a))	gated AWSART	56.36	97.48	705.16[\pm 0.98]
	MC gated AWSART	25.76	99.38	700.90[\pm 0.16]
	MC AWCR	11.20	99.55	702.23[\pm 0.06]
Divergent (Fig. 2.5(b))	gated AWSART	34.55	98.67	699.32[\pm 0.76]
	MC gated AWSART	26.20	99.10	702.47[\pm 0.35]
	MC AWCR	12.30	99.38	700.22[\pm 0.11]
Divergent (Fig. 2.5(c))	gated AWSART	40.63	99.07	694.61[\pm 4.06]
	MC gated AWSART	35.09	99.35	707.93[\pm 1.55]
	MC AWCR	18.21	99.42	698.49[\pm 0.12]

Table 2.3. Image quality measures. The mean absolute difference (MAD) and the normalized correlation coefficient (NCC) between the phantom images and the gated AWSART, the MC gated AWSART, and the MC AWCR reconstructed images in Fig. 2.10 are presented, respectively. Furthermore, even the mean and the standard deviation values are calculated inside the green circles in Fig. 2.10.

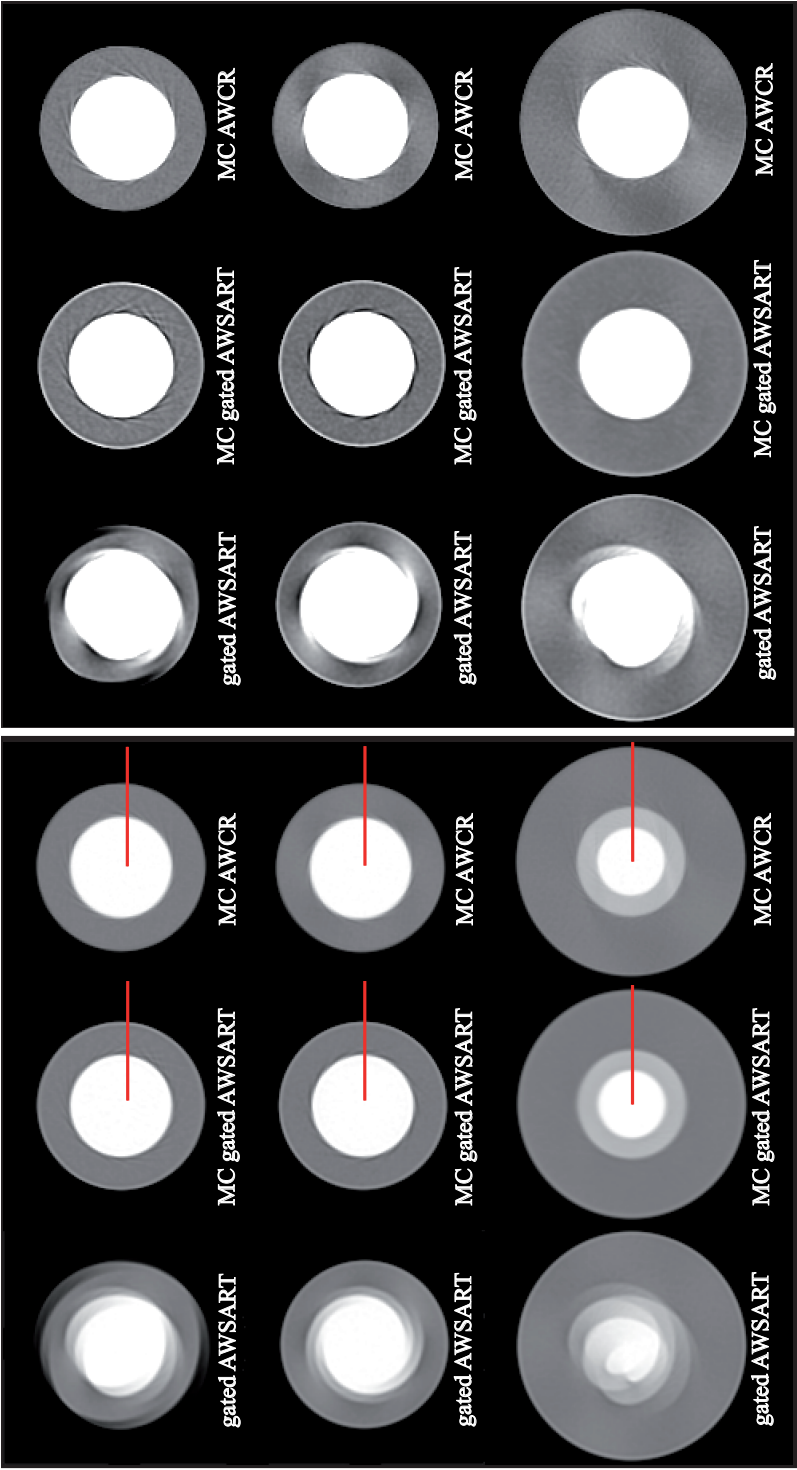


Figure 2.12. Like the Fig. 2.10, but here the reconstructed images are achieved by using noisy projections data sets. The red lines indicate the μ -values, which are shown in Fig. 2.13.

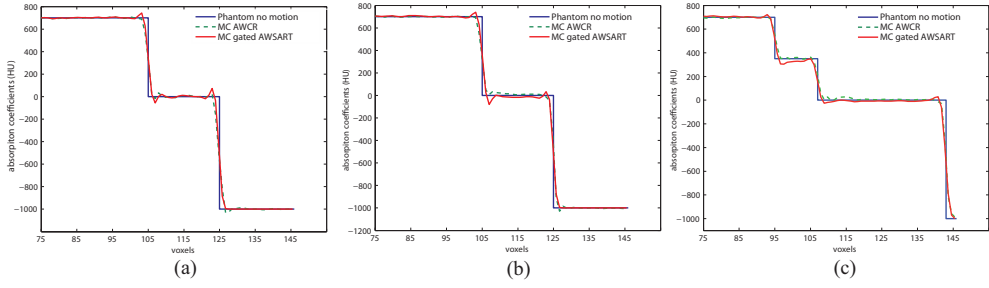


Figure 2.13. Like the Fig. 2.11, but here the absorption coefficients along the red lines indicated in Fig. 2.12 are shown.

the MC gated AWSART method with or without the proposed scaling of the volume of the blobs will lead to identical image quality results (Table 2.2). The results obtained in the three phantom cases, show, how the iterative MC reconstruction method using the correct motion fields and the proposed volume-adapted blob-footprint calculation allows to obtain almost motion artifact free images (Fig. 2.10, 2.11). Finally, in all the three cases, the quality of the images reconstructed with the MC gated AWSART method is almost identical to the image quality obtained with the MC AWCR method (Table 2.3). Remaining differences can be due to the approximation of the proposed blob-volume adaptation and to the discretization of the MVF used. The differences as slight over- and undershoot at sharp object boundaries is well known in the application of iterative reconstruction methods in X-ray tomography [146]. Even in case of noisy measurements, the proposed MC iterative reconstruction method shows robust performance and achieves an image quality almost similar to the one obtained with the MC analytical method (Fig. 2.12, 2.13).

As said in the introduction, an MC image reconstruction is feasible only if an MVF of the moving object is available. In cardiac CT, the exact calculation of the heart's MVF is a non-trivial problem. Even if several cardiac motion estimation methods have been proposed in literature, this issue is still under research [5, 43, 98, 124, 136]. In clinical application, the approximate knowledge of the MVFs could be cause of several inconsistencies in the MC reconstructed images. For example, an erroneous MVF could lead to MC reconstructed images with residual blurring artifacts. Moreover, an incorrect cardiac MVF estimation could lead to MC cardiac images with several unexpected anatomical incongruencies (*e.g.* broken or misaligned coronary arteries segments). The scope of this work was to test the correctness and robustness of a novel MC iterative reconstruction method with volume adapted blobs as basis functions by using a given exact MVF. The next step will be the study of proper cardiac MVF estimation methods to apply for MC iterative reconstructions with clinical patient data sets.

2.5 Conclusions

In this chapter, a three-dimensional method was presented for reconstructing moving objects from cone-beam X-ray projections using an iterative reconstruction algorithm taking a given MVF into account. For the image representation, adapted blobs are used as basis functions. An efficient method to calculate the line integrals through an adapted blob is proposed to solve the problem of how to compensate for the divergence in the MVF on a grid of basis functions. Two phantoms with three different known motion patterns were reconstructed, with excellent results. The proposed method can be used for the computation of 3D cardiac CT images in heart phases of strong motion. In the next chapters 3-5, this new method will be evaluated in clinical cardiac cases. In order to achieve consistent results, accurate motion estimation methods will be applied.

Motion-compensated iterative reconstruction of a region of interest in cardiac cone-beam CT

The fear of infinity is a form of myopia that destroys the possibility of seeing the actual infinite, even though it in its highest form has created and sustains us, and in its secondary transfinite forms occurs all around us and even inhabits our minds.

— GEORG CANTOR (1845 – 1918)

Abstract — A method for motion compensated iterative CT reconstruction of a cardiac region-of-interest is presented. The algorithm is an ordered subset maximum likelihood approach with spherically symmetric basis functions, and it uses an ECG for gating. Since the straightforward application of iterative methods to CT data has the drawback that a field-of-view has to be reconstructed, which covers the complete volume contributing to the absorption, region-of-interest reconstruction is applied here. Despite gating, residual object motion within the reconstructed gating window leads to motion blurring in the reconstructed image. To limit this effect, motion compensation is applied. Hereto, a gated 4D reconstruction at multiple phases is generated for the region-of-interest, and a limited set of vascular landmarks are manually annotated throughout the cardiac phases. A dense motion vector field is obtained from these landmarks by scattered data interpolation. The method is applied to two clinical data sets at strongest motion phases. Comparing the method to standard gated iterative reconstruction results shows that motion compensation strongly improved reconstruction quality.

3.1 Introduction

Cardiovascular diseases are the major cause of mortality and morbidity in most of the developed countries. Coronary artery disease is one of the main cardiovascular diseases.

Owing to recent advances in imaging hardware, diagnostic quality of coronary computed tomography (CT) has improved [31], and the role of CT in the (non-invasive) diagnosis of coronary arteries is expanding. Cone-beam computed tomography (CBCT) has proven to be useful in providing detailed morphological images of the coronary arteries. Still, the heart pulsation continues to be a limiting factor in cardiac CT. Electro-cardiogram (ECG) gated [26, 45, 47, 57, 86, 122] or triggered [29, 36] reconstruction methods can mitigate this problem, but never remove it completely. The standard gated CT reconstruction method assumes that the heart is stationary within the cardiac time window, which is an approximation.

If the motion of the object during acquisition can be recovered, motion compensation can be applied during image reconstruction to remove blurring due to cardiac motion [5, 39, 92, 98, 112, 136]. In addition, such an approach can potentially limit the radiation dose, as information from all of the acquired phases can be used for the reconstruction. For cardiac CT, estimating the heart motion vector field (MVF) is non-trivial issue and several methods have been proposed in literature. A first common step in many MVF estimation methods is to reconstruct a gated 4D dataset, i.e. a time sequence of 3D images.

Automatic MVF estimation methods have been proposed by Blondel et al. [5] and Jandt et al. [43]. Both presented a motion compensated (MC) reconstruction method that employed a 3D coronary centerline model to estimate the MVF of the coronary vessel tree from rotational X-ray projections. Stevendaal et al. [136] proposed a whole heart MVF estimation by applying model-based segmentation and shape tracking. Prümmer et al. [98] proposed a 4D FDK-like algorithm that used image registration techniques for heart motion estimation. Taguchi et al. [123, 124] proposed an iterative projection-based method that exploits a block-matching algorithm [83] to estimate the heart MVF from a 4D cardiac image data set. Schirra et al. [113] presented an MC analytical reconstruction method, where a rigid image registration was applied during quiescent cardiac phases to determine the MVF of calcified lesions of the coronary arteries. Here, temporal interpolation in parameter space was used in order to estimate motion during strong motion phases.

For coronary stent reconstruction, a manual MVF estimation method based on detecting 2-D markerball centers of the stent in projection image data has been proposed by Perrenot et al. [95]. Stevendaal et al. proposed [136] an MC ROI analytical reconstruction by using an MVF obtained by manually identifying a limited number of right coronary artery (RCA) landmarks.

Generally, MVF estimation methods yield an irregular distribution of measurements. To obtain a dense MVF, the measurements need to be resampled. The nearest-neighbor by inverse distance weighting (NNIDW) [116] and the thin-plate-spline (TPS) [6] interpolation methods can be used to interpolate or extrapolate a dense MVF to the entire image domain [133].

This chapter presents a method for MC gated iterative CT reconstruction of a

cardiac region-of-interest (ROI). The cardiac MVF is derived from a limited set of manually indicated landmarks. A method's landmarks localization error-sensitivity study is carried out. The maximum landmark position indication-error is determined which can be tolerated without degrading the MC reconstructed images by motion blurring. In order to obtain a dense MVF at the resolution of the regular reconstruction grid, the NNIDW and the TPS interpolation are applied, and results are compared. Reconstruction results for two clinical cases are shown and compared to standard gated iterative reconstruction results. Moreover, a motion-compensated filtered back-projection reconstruction method [136] is used, and the analytical and iterative reconstructed images are compared.

The chapter is organized as follows: Section 3.2 describes the MC iterative reconstruction algorithm, the MVF estimation and the scattered data interpolation methods. The experiments and results on the clinical data sets are presented in Sec. 3.3 and discussed in Sec. 3.4. Finally, conclusions are drawn in Sec. 3.5.

3.2 Method and materials

3.2.1 Introduction

In the following subsections MC iterative reconstruction is presented. First, the basic iterative algorithm is introduced (subsection 3.2.2). Subsequently, in subsection 3.2.3, it is described how a motion vector field can be incorporated in the iterative ROI reconstruction framework, and an efficient forward- and back-projection model for MC iterative reconstruction is presented. Finally, a manual method for MVF estimation of cardiac landmarks is described. In this subsection, a brief overview on the TPS and the NNIDW methods is given.

3.2.2 Basis functions and the iterative statistical reconstruction method

Transmission tomography aims at the reconstruction of a density distribution f of the object scanned. The continuous function f can be represented as a linear combination \tilde{f} of a limited set of basis functions b , placed on a 3D grid with N equidistant grid points, \vec{x}_j :

$$\tilde{f}(\vec{x}) = \sum_{j=1}^N \mu_j b(\vec{x} - \vec{x}_j), \quad (3.1)$$

where $N = N_x N_y N_z$ and N_x , N_y , and N_z are the number of grid points in x , y , and z directions, respectively. The set of numbers μ_j are the coefficients of expansion which describe the function \tilde{f} relative to the chosen set of basis functions $b(\vec{x} - \vec{x}_j)$. Lewitt [69] investigated how different sets of basis functions can influence the quality of the images. Spherically symmetric volume elements are alternatives to the more conventional voxels for the reconstruction of volume images. In the reconstructions presented in this chapter, the Kaiser-Bessel basis functions [68] are used. These spherically symmetric basis functions (also called blobs) are spatially limited and effectively

frequency limited. The standard parameters are used for the Kaiser-Bessel basis functions, which satisfy the frequency criteria described in [76]. Blobs as basis functions have many advantages compared with simple cubic voxels, *e.g.* their appearance is independent of the source position [68].

For the iterative ROI reconstruction presented in this contribution, an aperture weighted cardiac modified version of the iterative ordered subsets convex maximum likelihood (OSML) algorithm [50] is used. The OSML method is an ordered subset modification of the convex ML method [60], in which one update of the OSML method requires the sum over only a subset S_m of all projections simultaneously. The OSML reconstruction method takes the Poisson statistics of the measured photons into account. In a general CT acquisition, the various projections, i , measuring photon counts, Y_i , are independent. The log-likelihood function $L(\mathbf{u})$, with the absorption coefficient, μ_j , at position j can be written as

$$L(\mathbf{u}) = \sum_i (-d_i e^{\sum_j A_{ij} \mu_j} - Y_i \sum_j A_{ij} \mu_j) + c_1, \quad (3.2)$$

where \mathbf{u} is the image vector $\mathbf{u} = (\mu_1, \mu_2, \dots, \mu_j)$, d_i is the expected number of photons leaving the source towards the i -th projection. A_{ij} are the elements of the system matrix, and c_1 is an irrelevant constant that does not depend on \mathbf{u} . The function $L(\mathbf{u})$ has to be maximized to find the optimally reconstructed image. As described in Kamphuis et al. [50], an approximate solution of maximizing Eq. 3.2 leads to the following iterative step ($n \mapsto n+1$) in the OSML method:

$$\mu_j^{n+1} = \mu_j^n + \lambda \mu_j^n \frac{\sum_{i \in S_m} A_{ij} [d_i e^{-\langle A_i \mu^n \rangle} - Y_i]}{\sum_{i \in S_m} A_{ij} \langle A_i \mu^n \rangle d_i e^{-\langle A_i \mu^n \rangle}}, \quad (3.3)$$

with $\mu_j^n > 0$, and forward projections $\langle A_i \mu^n \rangle = \sum_j A_{ij} \mu_j^n$. The relaxation parameter, λ , is included to control convergence speed.

An aperture weighted cardiac modified version (AWCOSML) of the iterative algorithm based on Eq. 3.3 can be written as

$$\mu_j^{n+1} = \mu_j^n + \lambda \mu_j^n \frac{\sum_{i \in S_m} w_i^c w_i^a A_{ij} [d_i e^{-\langle A_i \mu^n \rangle} - Y_i]}{\sum_{i \in S_m} w_i^c w_i^a A_{ij} \langle A_i \mu^n \rangle d_i e^{-\langle A_i \mu^n \rangle}}, \quad (3.4)$$

where w_i^c (w_i^a) is the cardiac (aperture) weight for the measurement i [149]. Nielsen et al. [86] investigated the effect of various cardiac gating function shapes on image quality; following their results a rectangle with smooth edges is used in this evaluation. The reference phase point ϕ_k^P which define the k -th center of the gating windows with $1 \leq k \leq K$, is determined from the patient's ECGs, which are recorded in parallel with the CT acquisition.

In helical CT object points enter and leave the cone. Empirically, it was found that this leads to artifacts which can be reduced by means of introducing an aperture weighting function w_i^a in the iterative reconstruction update formula [57, 149]. The aperture weighting function is the same for all projections and only depends on the distance of a detector pixel, i , from the XY -plane defined by the source position. For

the reconstructions presented in this work, a \cos^2 aperture weighting function is used. Once all subsets are processed, one iteration is completed. Each subset S_m contains projections that have a constant angular increment inside each gating window, and the sequence of the subset is determined randomly.

The reconstruction process can be controlled by the relaxation parameter λ . Based on empirical evaluation, $\lambda = 0.8$ is chosen, which gave reasonable results. An important aspect for all iterative reconstruction methods is the manner in which the basis function is used for the interpolation in the forward- and back-projection.

3.2.3 MC iterative reconstruction of a cardiac region of interest

The proposed MC iterative reconstruction method requires an estimated MVF for all phases. For a cardiac reconstruction the MVF is represented by displacement vectors $\vec{m}_j(\vec{x}_j(\phi_r^P), \phi_r^P, \phi)$ of the corresponding grid point $\vec{x}_j(\phi_r^P)$ from a reference heart phase ϕ_r^P to a new position $\vec{x}_j^*(\phi)$ in an arbitrary heart phase ϕ by

$$\vec{x}_j^* = \vec{x}_j^*(\phi) = \vec{x}_j(\phi_r^P) + \vec{m}_j(\vec{x}_j(\phi_r^P), \phi_r^P, \phi). \quad (3.5)$$

Inserting the MVF of Eq. 3.5 into Eq. 3.1 yields

$$\tilde{f}^*(\vec{x}) = \sum_j \mu_j b(\vec{x} - \vec{x}_j^*). \quad (3.6)$$

As shown in Eq. 3.4, in order to perform the forward- and back-projection steps, the A_{ij} contribution of each blob to the detector pixel, i , have to be determined. Ziegler et al. [147] proposed a method for calculating the A_{ij} weights. In the first step, the center of each blob is projected onto the detector. The footprint of a blob, which consists of all parallel line integrals through the volume element, is magnified and centered at the projected blob-center on the detector. The magnification of the volume element is given by the ratio of the source-detector to source-blob distance. In a last step, the convolution of the footprint with the detector pixels is performed, which yields the weights A_{ij} .

In case of MC reconstruction of a moving object (*e.g.* the heart), the motion of the blob itself and the change of its volume caused by the existence of a divergent MVF (Eq. 3.5) is neglected. The non-vanishing divergence of the MVF results in a non-equidistant set of grid points. In case of MC reconstruction, a modified forward and back projection model is required which adapts the individual blob size in such a way that the representation of the image becomes more homogeneous [39] (see Chp. 2). In the next section 3.3, the applicability and performance on clinical data is shown.

Iterative reconstructions are computationally intensive, especially in case of high resolution image reconstruction over the entire FOV. In many clinical cases, the ROI is smaller than the volume that is irradiated. For example, in coronary cone-beam CT imaging, the ROI is often reduced to the main coronary vessels. Due to the reduced volume, ROI reconstruction is an efficient solution to increase the speed of iterative or analytical image reconstructions. For filtered back-projection (FBP) reconstruction methods [9, 51, 128], an ROI reconstruction is possible without any

extra efforts. Generally, an iterative reconstruction requires that an FOV has to be reconstructed that covers the whole volume, which contributed to the absorption.

In order to determine the sinogram of the ROI only, which is taken for the MC iterative ROI reconstruction, the method proposed by Ziegler et al. in [149] is used. The RCA of two clinical data sets was chosen as ROI for the reconstructions presented in this chapter.

3.2.4 Motion estimation by manual tracking of anatomical landmarks

In this subsection, the manual MVF estimation approach is described.

To determine the MVF, first a 4D ROI image data set is generated using a retrospectively gated FBP reconstruction [57]. Here, the 3D ROI images are reconstructed at equidistant phase points ϕ_k^P throughout the entire cardiac cycle with the smallest possible gating window width [74]. In this work, the MC gated reconstruction is performed in a phase of strong cardiac motion (*e.g.* systole). To detect a suitable fast motion phase within the RR interval, a *motion map* [75, 113] technique can be applied. The *mean absolute difference* is evaluated between subsequent volumes of the 4D ROI image data set of each patient to determine the motion map.

For single coronary segment manual motion tracking can be carried out. It is performed by scrolling through all the slices of the volume data set and identification of well known landmarks, *e.g.* *ostium*, *marginal acute branches* (*MAc-1,-2*), and *interventricular posterior branch* (*PDA*). This procedure is repeated for all data sets reconstructed at different heart phases. The displacement vectors from the chosen reference phase to all the other phases are determined for these landmarks. The MVF at the corners of the ROI are set to zero, in order to suppress projection of blobs outside the ROI sinogram. Finally, these motion fields are used as input control points for a TPS warping [6], which yields a dense MVF \vec{m}_j .

A well known drawback of the manual motion tracking is the frequent poor visibility of the anatomical landmarks. In fact, landmark visibility depends on many different factors as for example: the noise level, motion artifacts in phases of fast cardiac motion, and the grade of experience of the observer. In the clinical cases presented here, manual landmark tracking was not feasible in fast heart motion phases. Therefore, to fill this MVF estimation gap in these phases, the RCA's landmarks positions were determined by cubic spline interpolation [113]. The landmarks positions tracked inside the volumes reconstructed at slow motion phase points are used as knots.

The second step is to resample the MVF from the limited set of points irregularly placed inside the chosen ROI [133]. A resampling is necessary to extend the MVF to all the positions \vec{x}_j of the reconstruction regular grid. To select a suitable scattered data interpolator, the *a priori* knowledge on the cardiac motion, *e.g.* that it should be smooth, can be exploited. Different available scattered data interpolation methods satisfy this smoothness condition, i.e. they are continuously differentiable. Among these the most known is the nearest-neighbor by inverse distance weighting (NNIDW) [116]. The NNIDW interpolation method requires a metric operator to evaluate the distance between the interpolated grid point \vec{x}_j and a number of nearest

neighbors. Subsequently, these distances to the power of p are used to determine the inverse distance weights useful for the interpolation [116].

Another potential interpolant is the TPS. Proposed by Bookstein in [6], the TPS satisfies the smoothness condition and can be used for data interpolation. The TPS interpolation requires as an input that at least 3 control points have to be given.

In the following section, both the above mentioned scattered data interpolation methods are applied in a clinical case and the results are compared.

3.3 Experiments and results

The MC iterative ROI reconstruction method was applied to two clinical cardiac cases. Both data sets were acquired on a Brilliance 40(64) CT scanner (Philips Healthcare, Cleveland, OH, USA); the scanning parameters are listed in Table 3.1. The ROI has been chosen with a radius of 25 mm (case A) and 32.5 mm (case B), and the corresponding ROI's sinograms are shown in Fig. 3.1.

Case	A	B
Pitch [mm]	5	8
Relative Pitch	0.2	0.2
Collimation	40×0.625 mm	64×0.625 mm
Rotation time [s]	0.42	0.42
Tube voltage [keV]	120	120
Anode current [mA]	333	333
Mean heart rate [bpm]	55	56
Minimum heart rate [bpm]	53	54
Maximum heart rate [bpm]	58	59
Reconstruction Phase %RR	20	20

Table 3.1. CT scanning and reconstruction parameters.

In order to study the effect of motion compensation, the MC AWCOSML method is compared with a non-compensated AWCOSML method. The iterative reconstructions are performed using 15 subsets, each one filled with 500 projections (case A) and 600 projections (case B). The order of the subsets is determined randomly. A simple cubic grid of blobs is used (0.5 mm), and relaxation parameter was set to $\lambda=0.8$.

To perform an MC gated iterative reconstruction at a reference phase point of strong cardiac motion a motion map is used for both cases (Fig. 3.2). The *end systole* and the *diastasis* are clearly visible in regions between [35, 45]% RR and [65, 80]% RR. For both cases, the reference phase was selected at $\phi_r^P=20\%$ RR (systole) with a fixed gating window width $w_k = 40\%$ RR. The 4D ROI images data were generated by an aperture weighted cardiac reconstruction (AWCR) method [57] at phase points within the range from 0 to 40% RR in steps of 5% RR with a fixed gating window width of 22% RR.

The MVF is determined from these images from phase to phase by manual landmark tracking and motion field interpolation as described in subsection 3.2.4. In the clinical case A only four RCA's landmarks (RCA's *ostium*, *MAc-1*, *MAc-2*, and *PDA*) were well visible and were used to reconstruct the RCA (Fig. 3.3), while in the second case B only two clearly visible RCA's landmarks (RCA's *ostium* and *MAc-1*) were

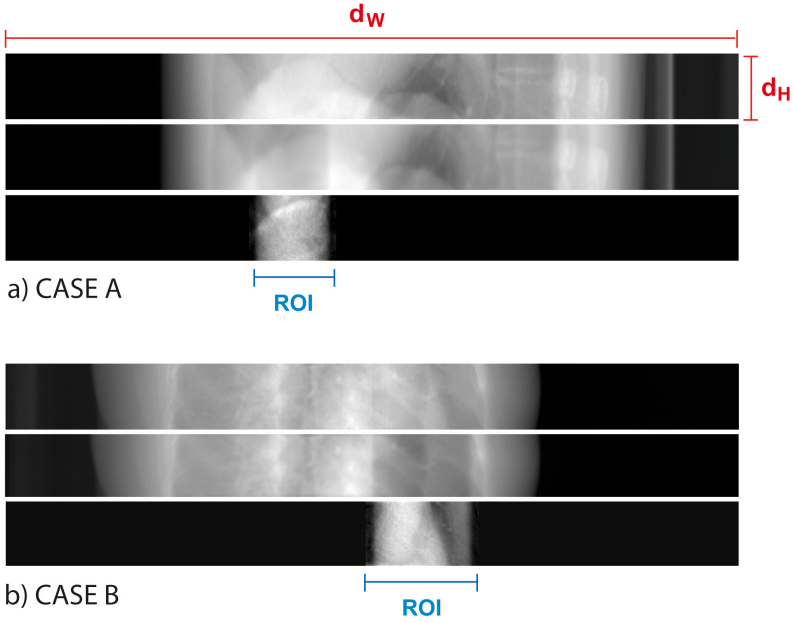


Figure 3.1. A view of the ROI of the clinical cases A and B. Top: complete FOV of one complete projection of the heart in the clinical case. Middle: complete FOV with ROI removed. Bottom: ROI projection.

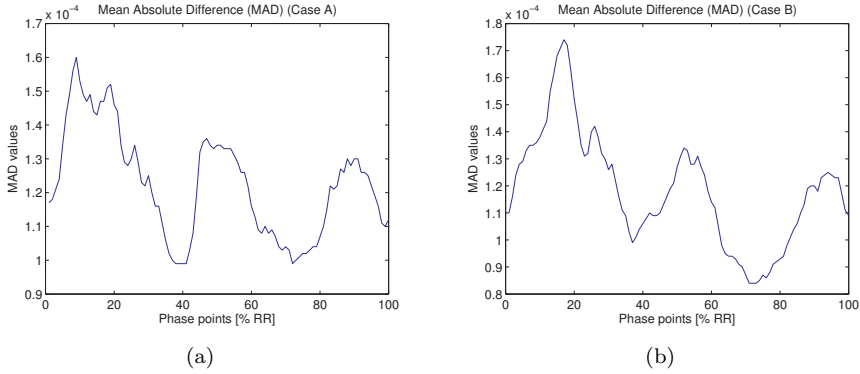


Figure 3.2. The motion maps of the two clinical cases A and B. The mean absolute differences ((a),(b)) evaluated between the subsequent volumes of the corresponding 4D ROI image data sets, are presented.

used to reconstruct the same coronary vessel (Fig. 3.4).

As first experiment, an error-sensitivity study is carried out, in order to determine the maximum landmark localization-error which can be tolerated without degrading the reconstructed images. This can be done by adding an increasing random error to

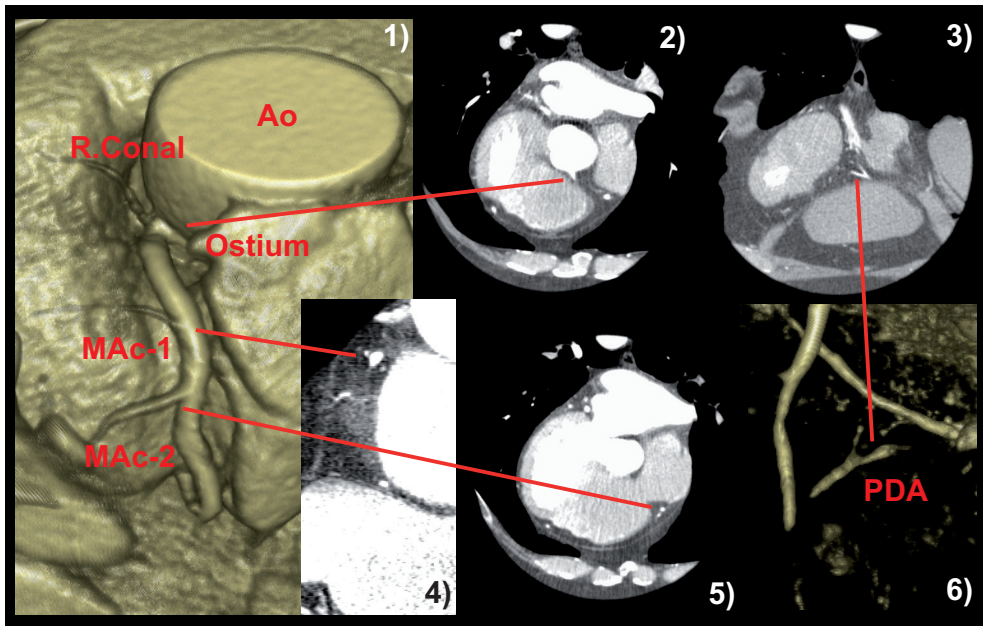


Figure 3.3. Manual RCA's landmarks motion tracking. In 1) and 6) the 3D volume rendering of the RCA vessel is shown. In 2),3),4) and 5) the corresponding landmarks on different views of a full FOV AWCR reconstruction are shown. Legend: Ao=Aorta, R. Conal=Right Conal branch, Ostium=RCA's ostia, MAc1-2=Marginal Acute branches, and PDA=Interventricular posterior branch. (Case A, AWCR method, at 75% RR, Level=0 HU, Window=500 HU).

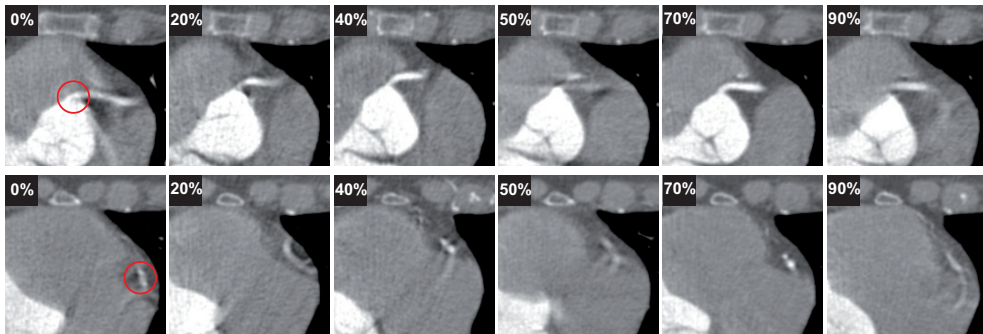


Figure 3.4. Two different axial views of the 4D ROI volumes data set. Top: an axial view where the RCA's ostium is visible. Bottom: an axial view where the RCA's first marginal acute branch (MAc-1) is visible. The red circles indicate the ostium and MAc-1 positions. (Case B, AWCR method, at [0,20,40,50,70,90] %RR, Level=200 HU, Window=900 HU).

the observed landmarks position as long as a blurred MC reconstruction is produced. Due to the lower motion of the *Aorta*, the RCA's *ostium* is generally well visible in the whole RR interval. The corresponding landmark position is left unchanged. Differently, at phases of stronger cardiac motion, the *MAc-1* is blurred and a landmark observation-error can likely take place.

Three different simulations are carried out. At each cardiac phase within the chosen gating window, the corresponding *MAc-1* landmark position is separately randomly displaced along the positive x,y, and z direction. For each direction, eight different error-displacement bins are tested: [0, 0.5], [0.5, 1], [1, 1.5], [1.5, 2.5], [2.5, 5], [5, 7.5], [7.5, 10], and [10, 15] mm. Given these modified landmark positions, a TPS interpolation is applied to recover a dense MVF \vec{m}_j . Subsequently, for each direction and for each error-displacement bin, an MC AWCRC method [136] is applied to generate the corresponding reconstruction. Finally, the reconstructed images are shown in Fig. 3.5.

In a second experiment, the TPS and the NNIDW scattered data interpolation methods are applied to case B, in order to recover its dense MVF \vec{m}_j from the above correctly indicated landmarks. For the NNIDW interpolation method, six nearest neighbors are selected for each grid point \vec{x}_j , the euclidean metric is chosen as distance function, and a power parameter $p = 2$ is used. The MC AWCOSML reconstructed images, where the MVF is calculated with the TPS and the NNIDW interpolation methods are compared in Fig. 3.6 and Fig. 3.7.

The proposed MC AWCOSML method is validated on both clinical cases. Here, the MC reconstructions are compared with the images produced performing a non-compensated AWCOSML method. The MVFs required for the corresponding MC reconstructions are determined by TPS interpolation. The reconstruction results after 15 iterations are shown for case A in Fig. 3.8, and for case B in Fig. 3.10. In Figures. 3.9 and 3.11 the 3D volume rendered images are presented for case A and B, respectively.

For the sake of comparison, the same clinical cases are reconstructed with the MC AWCRC method. Hence, the analytical and iterative reconstructed images are compared in Fig. 3.12. In Table 3.2, quantitative image quality measures evaluated inside the red circles in the reconstructed images in Fig. 3.12 are presented.

Case	Method	Mean[\pm STD] [HU]	SNR
A	MC AWCRC	83.2[\pm 32.5]	33.3
	MC AWCOSML	88.3[\pm 27.4]	39.7
B	MC AWCRC	103.2[\pm 19.2]	57.5
	MC AWCOSML	95.3[\pm 16.2]	67.6

Table 3.2. Image quality measures. The MC AWCRC and MC AWCOSML images mean, standard deviation (STD), and signal-to-noise ratio (SNR) values are determined inside the red circles (radius=15 mm) in Fig. 3.12.

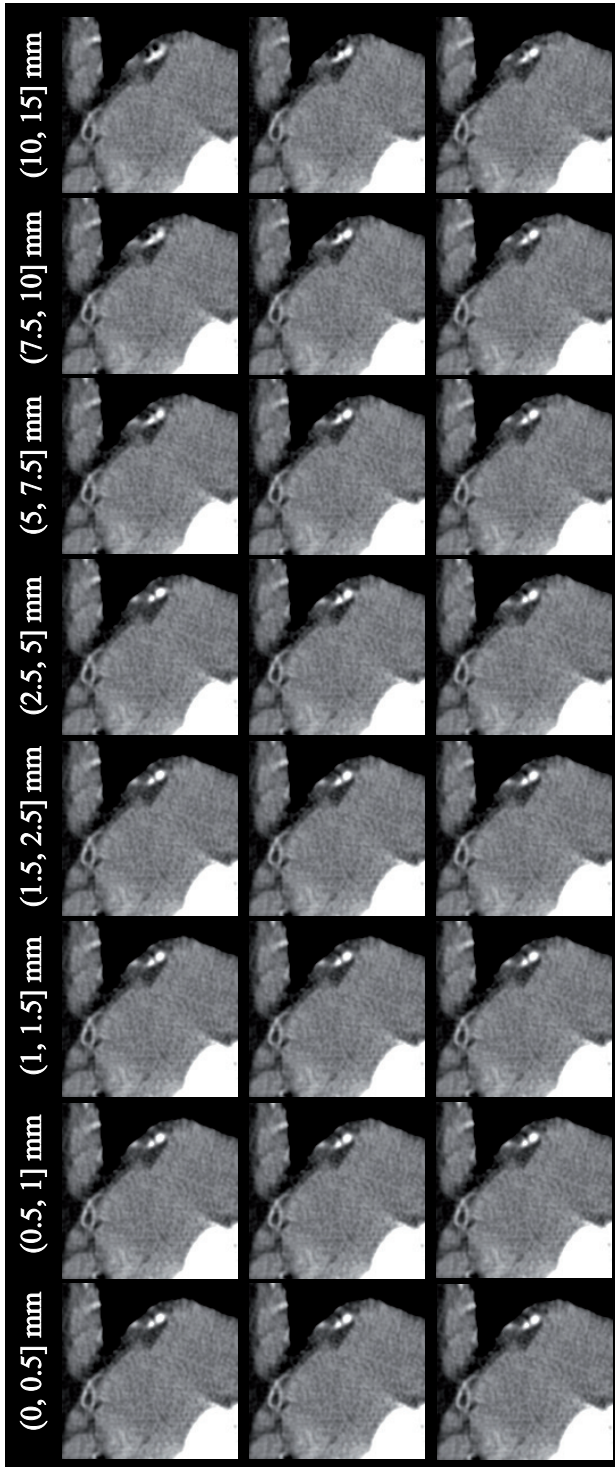


Figure 3.5. Manual landmarks localization error. The axial views containing the *MAc-1* landmark, respectively for each error-displacement bin applied to the *MAc-1* landmark position, on x (upper row), y (middle row) and z (bottom row) positive direction, are presented. (Case B, MC AWCRC method, at phase point 20% RR, gating window width of 40% RR, Level=150 HU, Window=500 HU)

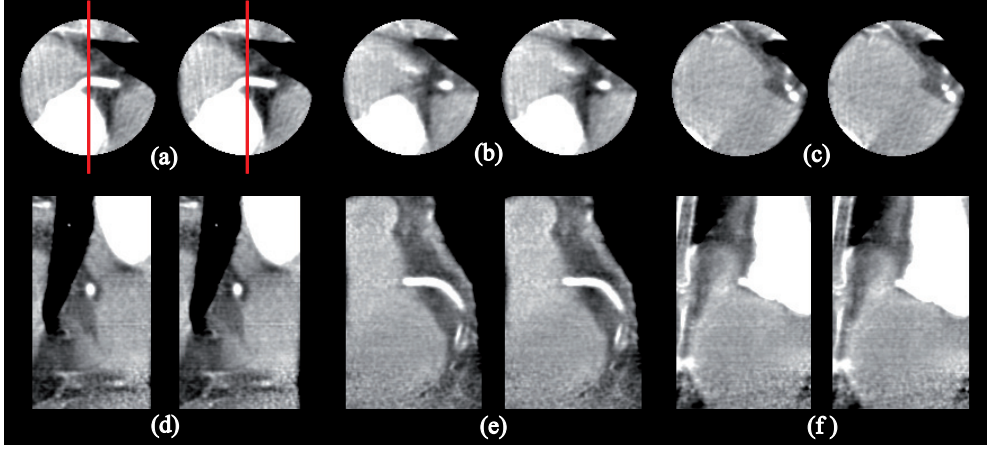


Figure 3.6. Axial (a,b,c), coronal (e), and sagittal (d,f) views. The MC AWCOSML reconstructed images, where the MVF is determined with the TPS (left) and the NNIDW (right) interpolation methods, are shown. (Case B, at phase point 20% RR, gating window width of 40% RR, 15 iterations, Level=0 HU, Window=500 HU).

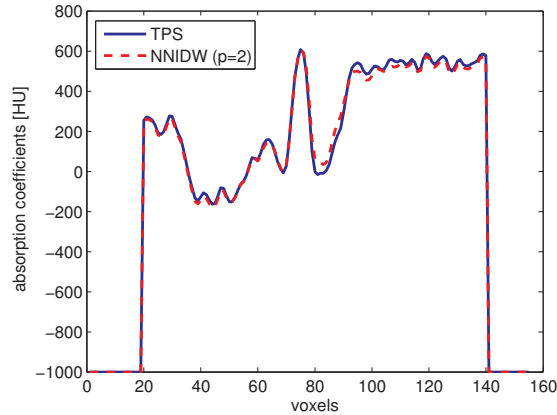


Figure 3.7. Absorption coefficients of the MC AWCOSML reconstructed images, where the MVF is determined with the TPS (blue) and the NNIDW (dashed red) interpolation methods, respectively, along the red lines indicated in Fig. 3.6(a).

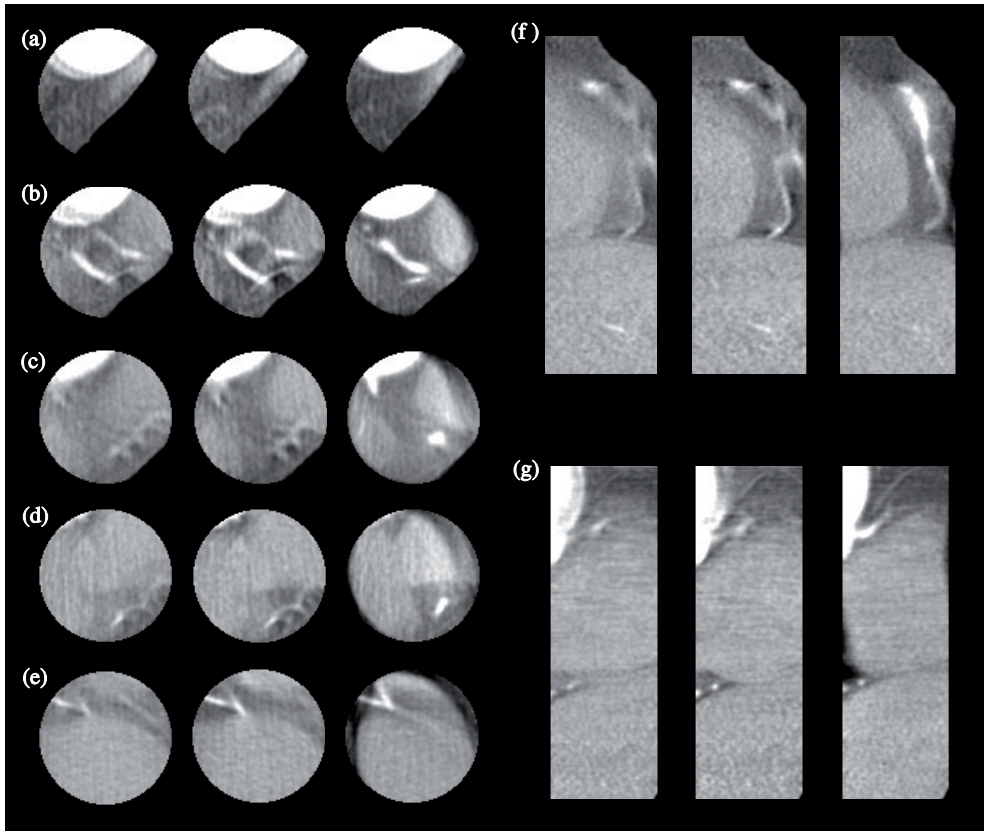


Figure 3.8. Axial (a,b,c,d,e), coronal (f) and sagittal (g) views. Images reconstructed with the AWCOSML with gating window width of 40% RR (left), the AWCOSML with gating window width of 22% RR (center), and the MC AWCOSML with gating window width of 40% RR (right) are shown. (Case A, at phase point 20% RR, 15 iterations, Level=0 HU, Window=500 HU).

3.4 Discussion

Owing to cardiac motion, cardiac CT image quality of gated reconstructions strongly depends on the cardiac phase. The larger the gating window the better the image's SNR, because more projections contribute to the reconstruction results. However, a wider gating window produces more motion artifacts. Also, at certain cardiac phases of rapid motion, cardiac CT reconstruction quality is seriously compromised. In the cases presented in this chapter, a reconstruction without MC at systole (20% RR) yields blurred images.

Utilizing MC in the reconstruction, it is shown on two example clinical data sets that motion blurring is almost removed. Sharp images can be obtained, even in a phase of strong motion reconstructed with a large gating window.

In order to generate the initial 4D volume data sets that were used to estimate

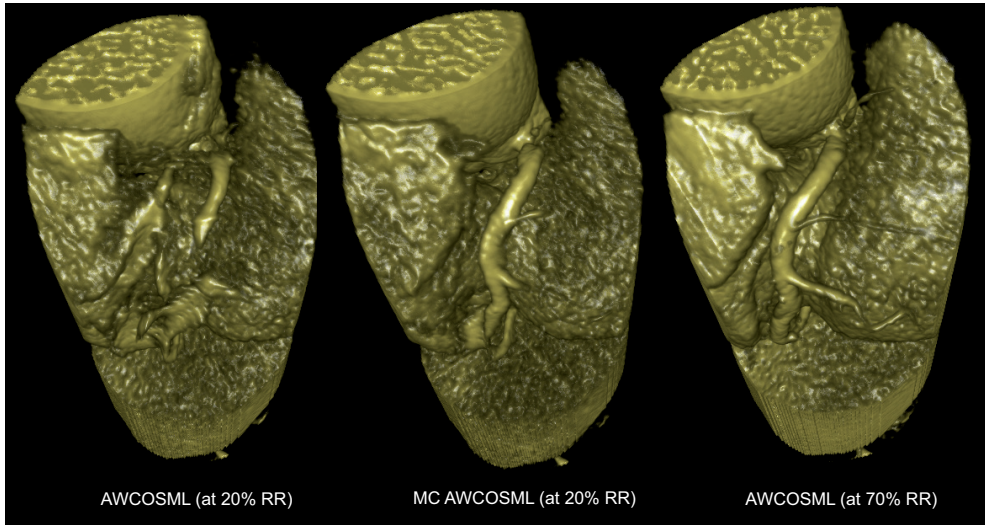


Figure 3.9. 3D volume rendering of the reconstructed volumes of case A. In order, the volume reconstructed with the AWCOSML method at a reference phase of 20% RR (left), the MC AWCOSML method at a reference phase of 20% RR (center), and the AWCOSML method at a reference phase of 70% RR (right), are presented. (Gating window width of 40 % RR, 15 iterations).

the MVF, a gating window width of 22% RR was used [74]. In contrast, for the final volume reconstructions, in order to show the positive impact of the MVF on image quality, a wider gating window width of 40% RR was used.

The first inspection about the landmarks localization error-sensitivity of the proposed method (Fig. 3.5) shows as a localization error less or equal to 5 mm (corresponding to 10 times the voxel size) does not affect the final MC reconstructed image. Even a larger error can be tolerated, though it should not exceed 7.5 mm. In Fig. 3.5 it is shown that a *MAc-1* landmark localization error in x or y direction larger than 7.5 mm yields images where the RCA's *MAc-1* is blurred.

In this contribution, given a limited set of observer-indicated landmarks, the TPS and the NNIDW scattered data interpolation methods are used to determine the dense cardiac ROI MVF. In accordance with Stevendaal et al. [133], in this paper similar results are achieved using both interpolants (Fig. 3.6). Consequently, from the absorption profiles presented in Fig.3.7, only very small differences are observable. Moreover, since limited sets of landmarks are used, the computation times of both methods are comparable. In conclusions, both scattered data interpolation techniques can be applied for the MVF resampling, without affecting the quality of the MC reconstructed images.

Therefore, a clinical validation of the proposed MC statistical iterative method is carried out, and results are compared with traditional ECG-gated iterative reconstructions.

In the first clinical case, using only a simple gated reconstruction, some anatom-

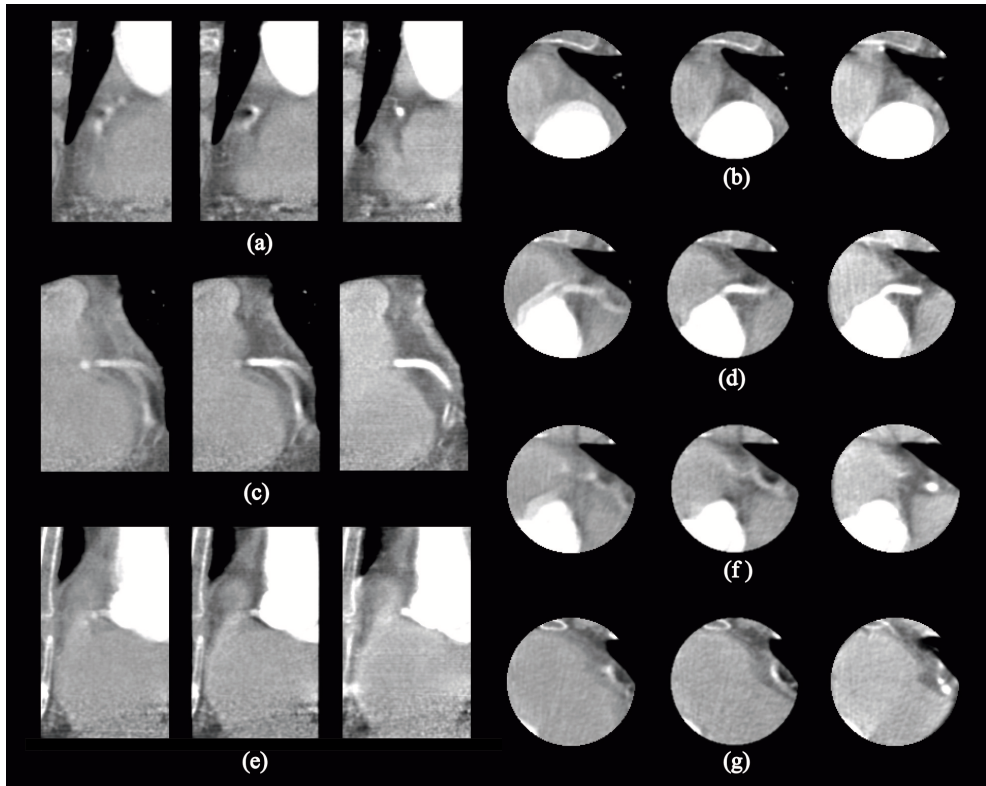


Figure 3.10. Axial (b,d,f,g), coronal (c), and sagittal (a,e) views. The AWCOSML with gating window width of 40% RR (left), the AWCOSML with gating window width of 22% RR (center), and the MC AWCOSML with gating window width of 40% RR(right) reconstructed images are shown. (Case B, at phase point 20% RR, 15 iterations, Level=0 HU, Window=500 HU).

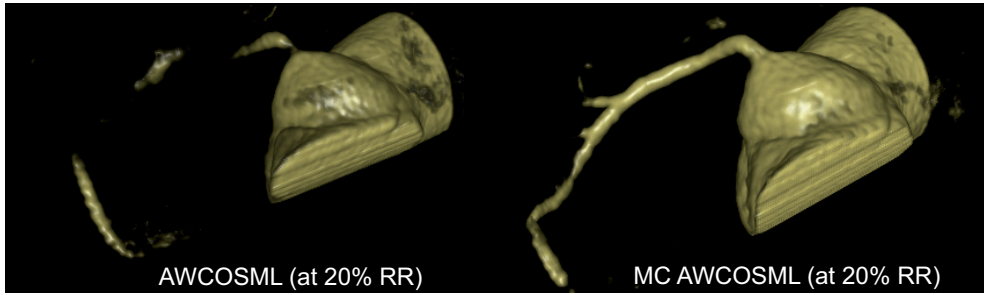


Figure 3.11. 3D volume rendering of the reconstructed volumes of case B. The AWCOSML (left) and the MC AWCOSML (right) reconstructed images are shown. (Phase point 20% RR, gating window width of 40 % RR, 15 iterations).

ical RCA's features as its *ostium* and its *marginal acute branches* were practically invisible or strongly blurred (Fig. 3.8,3.9). By adding the MC framework, most features were recovered. In Fig. 3.8(b) the *MAc-1* branch is clearly visible. Even the *MAc-2* vessel is clearly visible in the Fig. 3.8(d). The *Aorta* is very sharp in Fig. 3.8(a) and the RCA's outlet is well visible in Fig. 3.8(c) and Fig. 3.8(g). Finally the RCA's *PDA* and the complete RCA vessel are clearly visible in Fig. 3.8(e) and in Fig. 3.8(f), respectively. In Fig. 3.9 the 3D volume rendering of the images reconstructed with the AWCOSML method at 20% RR, the MC AWCOSML method at 20% RR, and with the AWCOSML method at 70% RR for the case A are shown. From these images it can be observed how the MC reconstruction can strongly reduce the blurring artifact in the reconstructed images. In fact, the MC reconstruction at 20% RR produces an RCA vessel that is consistent with the one obtained with a simple AWCOSML method at the quiet phase of 70% RR. Even the secondary vessels are clearly visible.

Similar results are achieved for the second clinical case (Fig. 3.10). In Fig. 3.10(a), a sagittal view of the chosen ROI is presented. Here, the AWCOSML method leads to blurred images where the *Aorta* is very sharp, but a section of the RCA is almost invisible. Instead, the MC AWCOSML method leads to a motion-free reconstructed image where both the *Aorta* and the RCA vessel section are clearly observable. The false RCA's shrinkages which are present in the non-compensated reconstructions could lead to diagnostic inaccuracies. In Fig. 3.10(c), a coronal view of the RCA vessel is presented. Again, due to the residual cardiac motion within the reconstruction gating window, the standard AWCOSML reconstructions produce images representing two different motion states of the RCA vessel. Even though, the AWCOSML reconstruction with the narrowest gating window width of 22% RR looks sharper, the absorption reduction caused by the motion artifact could lead again to an ambiguous diagnosis of the RCA vessel condition. Moreover, due the two RCA vessels achieved, the correct position of the vessel at the chosen reference phase is still unknown. The MC AWCOSML reconstruction, introducing the whole ROI motion information inside the reconstruction framework, allows to use all projections which contribute to the absorption value of each blob in the reconstruction grid. In the MC reconstructed images the above absorption reduction is avoided, the correct motion

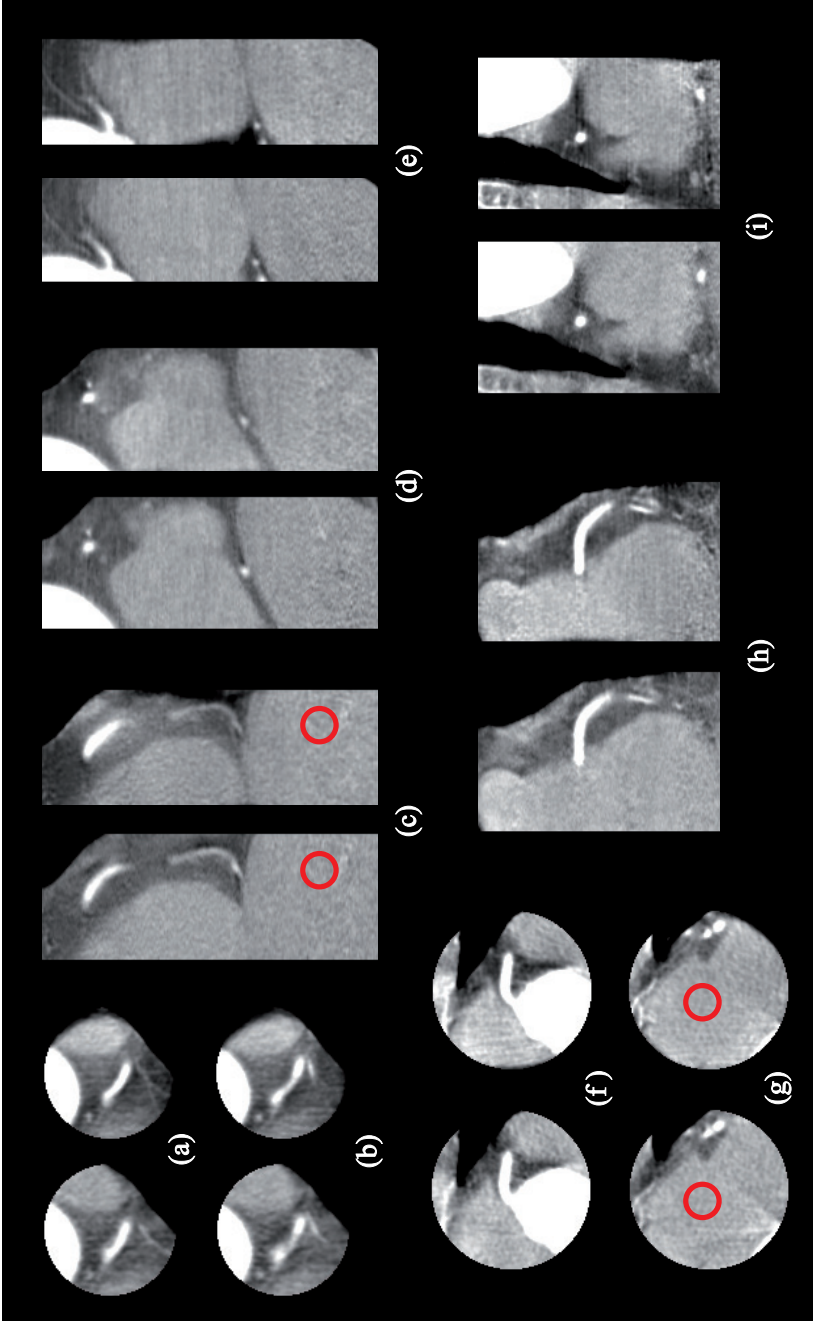


Figure 3.12. Axial (a,b), coronal (c), and sagittal (d,e) views of the case A, and axial (f,g), coronal (h), and sagittal (i) views of the case B. The MC AWCOSML (left) and the MC AWCOSML (right) reconstructed images are shown. For reasons of comparison, in the MC AWCOSML reconstructed images, the identical cylindrical ROIs which are used for the iterative reconstructions are cut out. (Phase point 20% RR, gating window width of 40% RR, 15 iterations, Level=0 HU, Window=500 HU).

state is represented, and the exact RCA vessel position is obtained (Fig. 3.10(c)). Similar conclusions can be achieved for the reconstructed images in Fig. 3.10(d-e). Here, the AWCOSML reconstructions lead to strongly blurred images with a stenotic RCA's *ostium*. Instead, the MC AWCOSML reconstruction produces an image where the correct RCA's *ostium* with any stenosis is shown (Fig. 3.10(d-e)). In Fig. 3.10(f) it is clearly visible as the AWCOSML method fails to recover the RCA vessel section, which instead is clearly visible in the MC AWCOSML reconstruction. Finally, in Fig. 3.10(g) it is noticeable as the AWCOSML reconstructions produce strongly blurred images of the RCA's *MAc-1*, which instead it is clearly observable in the MC AWCOSML reconstructed image. The 3D volume rendering images, confirm the blurring artifact reduction achieved by the MC AWCOSML (Fig. 3.11). This leads to significantly better image quality than achieved with AWCOSML.

Finally, from the reconstructed images presented in Fig. 3.12, it is observable that the MC iterative and the MC analytical reconstruction methods lead to almost similar results without motion artifacts. At the used number of iterations the resulting image quality is comparable. In accordance with Ziegler et al. [148,149], a higher SNR resulting from statistical iterative reconstructions can be observed (Table 3.2). Here, the motion compensated reconstruction and statistical iterative image reconstruction show their combined advantages.

Though, strong improvement, can be achieved based on manual landmarks tracking, the fact that the current method requires interaction, and that a successful MC reconstruction depends on the level of experience of the observer is a limitation of the proposed method. Albeit for the clinical cases proposed in this chapter, it was previously shown that small errors on the landmarks tracking do not affect the final reconstruction results too much. An automatic MVF estimation methodology will be preferable for clinical applications. Obviously, the next step will be to integrate fully automatic local motion estimation into this framework. From the study presented in this work it can be concluded, that this method may either be based on automatic landmark tracking or on image based ROI registration. Temporal and spatial continuity can be achieved by interpolation.

However, the manual approach as proposed in this chapter, can be very useful for individual vessel segments. With limited user interaction in a number of cardiac phases, a significant improvement in image quality can be achieved. This can be useful for segments which contain suspicious structures and in which standard reconstruction results yield limited quality. For example in segments case of hardly visible soft plaques, the parallel SNR improvement and motion artifact reduction can be used to reduce ambiguous diagnosis without performing a second examination.

3.5 Conclusions

A MC gated iterative ROI reconstruction method was presented that leads to strong image quality improvements compared to a gated iterative ROI method. The method was successfully tested on two clinical cases. The gain in speed, typical in ROI reconstruction, is not compromised owing to motion compensation. The integration of the MC framework with the gating approach allows to achieve images with reduced

motion blurring and a higher SNR. The main application of the method proposed is seen in cardiac CT, *e.g.* for coronary vessel segment reconstructions. The next step will be the implementation of semi- and fully-automatic image-based MVF estimation methods.

Cardiac motion-corrected iterative cone-beam CT reconstruction using a semi-automatic minimum cost path-based coronary centerline extraction

There are two possible outcomes: If the result confirms the hypothesis, then you've made a measurement. If the result is contrary to the hypothesis, then you've made a discovery.

— ENRICO FERMI (1901 – 1954)

Abstract — In this chapter a method which combines iterative computed tomography reconstruction and coronary centerline extraction technique to obtain motion artifact-free reconstructed images of the coronary arteries is proposed and evaluated. The method relies on motion-vector fields derived from a set of coronary centerlines extracted at multiple cardiac phases within the RR interval. Hereto, start and end points are provided by the user in one time-frame only. Using an elastic image registration, these points are propagated to all the remaining cardiac phases. Consequently, a multi-phase three-dimensional coronary centerline is determined by applying a semi-automatic minimum cost path based extraction method. Corresponding centerline positions are used to determine the relative motion-vector fields from phase to phase. Finally, dense motion-vector fields are achieved by thin-plate-spline interpolation and used to perform a motion-corrected iterative reconstruction of a selected region of interest. The performance of the method is validated on three patients, showing the improved sharpness of cardiac motion-corrected gated iterative reconstructions compared to the results achieved by a classical gated iterative method. The results are also compared to the manual coronary artery motion estimation method proposed in the previous chapter.

4.1 Introduction

Cardiovascular disease (CVD) is one of the leading causes of death worldwide [145]. In 2005 about 30% of global deaths were caused from CVD (including cardiac infarctions and apoplectic strokes). If the current trend will not be opposed, by 2020 about 20 million deceases will be caused by this disease [73].

Acute coronary events are caused by spontaneous rupture of non-calcified plaques. Non-invasive monitoring of patients that have these non-calcified plaques can be helpful for diagnosis and the treatment [10,64]. In the last decade, due to the technological progress in computed tomography (CT) imaging devices, the imaging of coronary arteries with CT has become a rapidly emerging application for diagnosis and therapy guidance of coronary arteries diseases [31].

Three-dimensional (3D) electrocardiogram (ECG)-gated CT reconstructions are used [26,45,57,86,122] to provide images of a chosen cardiac time window. Hereto, an ECG of the patient is recorded simultaneously with the CT acquisition. Subsequently, cardiac gating techniques are applied to improve the effective temporal resolution and to minimize cardiac motion artifacts. Nevertheless, due to the rather fast heart motion compared to the scanner rotation time, residual motion artifacts are still visible in the ECG-gated CT reconstructed images.

If the cardiac motion information is included in the reconstruction model, and a cardiac motion-corrected (MC) reconstruction is carried out [5,39,40,92,112,135], motion artifacts in the reconstructed images can be strongly reduced, even if the cardiac window includes phases of fast cardiac motion (*e.g.* systole). Moreover, since information from all the aquired cardiac phases can be used for the reconstruction, such a method can potentially reduce the radiation dose to the patient.

Owing to the strong motion of the coronary arteries, specialised methodologies are required to track their movement along the cardiac cycle. In prior works, manually indicated anatomical landmarks [40,95] have been used to assess the coronary artery motion field. However, automatic coronary centerlines extraction methods [5,42,43,77,111] appear to be a more accurate solution to determine the unknown MVF of tiny structures as the coronary arteries. Indeed, given the coronary centerlines at different phases within the RR interval, the relative MVFs correspond to the displacement of the centerline points from phase to phase. Obviously, in order to calculate the MVFs, corresponding points along the coronary centerlines have to be detected. In [43], Jandt et al. applied a 3D-3D correspondence measure to determine corresponding points along the extracted multi-phase 3D coronary centerlines.

At phases of fast cardiac motion, where due to strong motion artifacts the above coronary centerline extraction methods are likely to fail, a temporal interpolation can be used to estimate the position of the centerline points. Hereto, the centerlines extracted at adjacent cardiac phases can be used as interpolation knots. Subsequently, given the previously determined coronary centerline MVF, a suitable interpolator, as *e.g.* the thin-plate-spline (TPS) [6], can be applied to obtain a dense MVF for the whole chosen time window [40,43,112,133]. In the last step, the determined MVF can be used to perform an MC region of interest (ROI) reconstruction.

Iterative reconstruction methods [25,60], have proven to be a good alternative to classical analytical reconstruction methods [85,93,126]. Iterative methods are able

to reconstruct objects with different acquisition geometries, and even in situations where the data elements are noisy or where only a moderate amount of data is available. However, the well known large computation time of iterative reconstructions continues to be a non-trivial issue which limits their use for clinical applications. In recent works [37, 149] it was shown that ROI reconstruction can lead to a strong reduction of the iterative reconstruction's computation time.

In this chapter, an MC reconstruction method for coronary arteries is proposed which combines iterative ROI reconstruction method and a coronary centerline extraction technique. Since the right coronary artery (RCA) moves more than twice faster than the left coronary artery (LCA) over the cardiac cycle [2, 32, 137], a ROI containing the RCA is selected and reconstructed. The method proposed by Metz et al. [77] is applied to extract the coronary artery centerlines from a given four-dimensional (4D) CT data set. Hereto, the start and end-point of the vessel segment of interest are indicated in one of the volumes of the 4D CT data set and propagated to the other timepoints by means of a non rigid image registration method [54, 55, 59]. Subsequently, the MVF for the coronary centerlines is determined from a selected reference phase to all other phases within the chosen reconstruction gating window. A dense MVF over the whole chosen ROI is achieved using TPS interpolation. Using this MVF, an MC ECG-gated modified version of the Simultaneous Algebraic Reconstruction Technique [39] is applied to produce motion artifact-free images of the RCA for three patients. The MC iterative reconstruction results are visually and quantitatively compared to the corresponding images resulting from a classical non motion-corrected ECG-gated iterative reconstruction method. Moreover, the results are also compared to results obtained with the manual coronary artery motion estimation method [40] introduced in previous chapter.

The chapter is organized as follows: in Section 4.2 all components of the proposed MC reconstruction algorithm are presented. The results on the clinical data sets are shown in Sec. 4.3 and discussed in Sec. 4.4. Finally, conclusions are given in Sec. 4.5.

4.2 Methodology

In the following subsections the components of the proposed MC reconstruction framework are presented. First, the 4D CT acquisition method is briefly described (4.2.1). Then, in subsection 4.2.2 a semi-automatic coronary artery centerline extraction method for local MVF estimation is described. Finally, the MC iterative algorithm used is introduced (4.2.3). The method's workflow is summarized by the diagram in Fig. 4.1. Solid rectangles represent algorithms, dashed rectangles indicate human user-interaction, and oval shapes represent both input data and output results of the algorithms.

4.2.1 4D ROI image reconstruction

The proposed method requires a 4D image data set in order to determine an MVF of the chosen ROI. In this contribution, 4D reconstruction is achieved by using an aperture weighted cardiac reconstruction (AWCR) method [57]. Hereto, the patient's

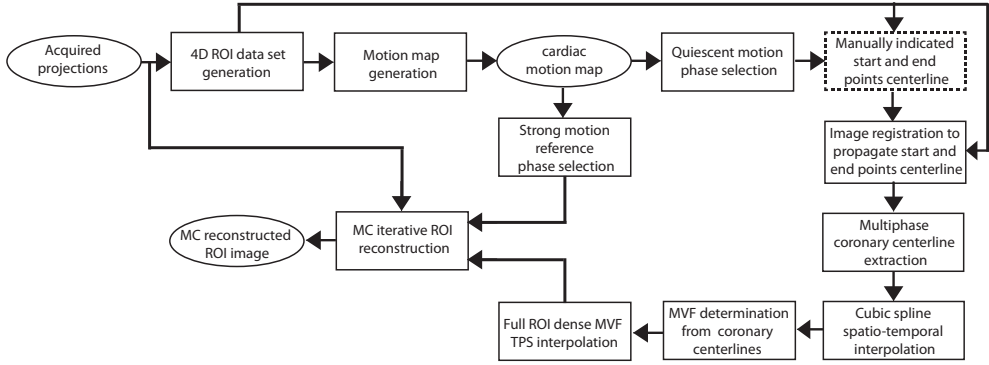


Figure 4.1. Workflow for the proposed MC iterative ROI reconstruction.

ECG is recorded simultaneously with the acquisition of the projection data to determine a list of N_r R-peaks at angular CT system positions ϕ_k^R , where k denotes the heart cycle index inside the recorded ECG. These angular positions are converted to the corresponding projection indices that were recorded at these angles. From the list of R-peaks, the centers ϕ_k^P of the gating windows, the so-called *phase points*, can be determined using, for example, a fixed percentage $P \in [0, 1)$ of the RR interval. The same percentage is used for all cardiac cycles,

$$\phi_k^P = \phi_k^R + P (\phi_{k+1}^R - \phi_k^R) \quad \forall k = 1, \dots, N_p. \quad (4.1)$$

$N_p = N_r - 1$ phase points are obtained. A gating function with a width w_k is centered at each phase point ϕ_k^P . Hence, only projections which lie inside this gating window are used to reconstruct the image. 3D AWCR images are reconstructed at equidistant phase points throughout the entire cardiac cycle. For each reconstruction, an automatic method proposed by Manzke et al. [74] is applied to select the smallest possible gating window width which provides sufficient angular coverage of projections for the reconstruction at each phase point.

In this chapter, MC iterative ECG-gated reconstructions are performed at phases of strong cardiac motion. To select suitable fast and quiet cardiac motion phases within the RR interval, a *motion map* (MM) [30, 40, 75, 113] is derived by calculating the *mean absolute difference* (MAD) between subsequent volumes of the 4D data set. The MAD is given by

$$MAD_l = \frac{1}{N} \sum_{i=1}^N |I^l(\vec{x}_i) - I^{l+1}(\vec{x}_i)|, \quad (4.2)$$

where $N = N_x N_y N_z$ and N_x , N_y and N_z are the number of image grid points in the x , y and z direction respectively, $I^l(\vec{x}_i)$ is the intensity of the image at voxel position \vec{x}_i , and l denotes the timepoint index inside the 4D ROI data set. In cases of limited motion, two subsequent timepoint images are very similar and therefore the MAD will be small.

4.2.2 Local motion estimation by semi-automatic coronary centerline extraction

Estimation of an MVF is a pre-requisite for MC cardiac CT reconstruction. For a cardiac reconstruction the MVF can be represented by displacement vectors $\vec{m}_i(\vec{x}_i(P_r), P_r, P)$ of the corresponding grid point $\vec{x}_i(P_r)$ from a reference heart phase P_r to a new grid position $\vec{x}_i^*(P)$ in an arbitrary heart phase P by

$$\vec{x}_i^* = \vec{x}_i^*(P) = \vec{x}_i(P_r) + \vec{m}_i(\vec{x}_i(P_r), P_r, P), \quad (4.3)$$

The MVF for the chosen cardiac ROI is determined by extracting the centerline of the RCA at each phase inside the chosen reconstruction gating window width. The centerline of the coronary artery segment of interest is determined by a minimum cost path approach [77]. The start and end-point of the vessel segment of interest are manually defined in one of the time-frames of the 4D CT data.

Subsequently, these start and end-points are propagated to the other time-frames using an elastic registration approach [54]. As an image dissimilarity metric, the sum of squared differences is used. The deformation field is represented by B-splines bases [109, 129]. To minimize the dissimilarity metric an adaptive stochastic gradient descent optimizer is used [54]. Trilinear interpolation is applied to determine image values at off-grid positions. The adaptive stochastic optimizer employs stochastic sampling to randomly select a subset of image samples at each optimization's iteration. Finally, a multi-resolution approach is applied to avoid a local minimum. Hereto, the images are smoothed using Gaussian blurring with a standard deviation dependent on the resolution level, followed by a downsampling step, to reduce memory consumption. The (isotropic) B-spline control point spacing is also dependent on the resolution level.

Given the multi-phase pairs of start and end-points, the corresponding coronary artery centerline is determined using the method proposed by Metz et al. in [77]. Here, the Dijkstra's algorithm [18] is used to find the path having minimum cumulative costs through a cost image. This cost image is derived from the input ROI image and is based on a frequently used vesselness measure [24], and on a priori information about the intensity in which the coronary arteries appear in CT images, *viz.* as bright tubular structures in a darker environment [77].

Due to the frequent presence of strong motion blurring artifacts, this coronary centerline extraction method is likely to fail to extract an accurate centerline in the volumes reconstructed at fast cardiac motion phases. To fill the centerlines estimation gap at these phases, the coronary centerlines points are determined by cubic spline interpolation [113]. The centerline positions extracted from the volumes reconstructed at the closest phases with low motion are used as interpolation knots.

At this point, a 4D coronary centerlines data set is available. Since the coronary centerlines positions extracted by the described method are not equally spaced, a 3D-3D correspondency between the multi-phase centerlines points is not readily available. Assuming that the start and end centerline points correspondence has correctly been achieved by the registration method, and assuming that the vessels length does not change significantly during the cardiac cycle, a possible solution to find a 3D-3D correspondence among multi-phase extracted centerlines positions is to apply

a spatial resampling. Cubic spline interpolation is applied to the 4D coronary centerlines data set in order to determine equally spaced centerline points. Here, the initially extracted coronary centerline points are used as interpolation knots.

Subsequently, these equidistant centerline positions are used to determine the corresponding displacement vectors from a chosen reference phase P_r to all the arbitrary phases P within the chosen ECG-gating window (Eq. 4.3). A dense MVF for the complete cardiac ROI is estimated by fitting a TPS [6] through the centerline displacements. Thereby, 8 additional control points with zero displacements are placed at the corners of the ROI, in order to suppress image grid points that leave the ROI and are projected outside its sinogram.

4.2.3 Motion-corrected iterative cardiac CT ROI reconstruction

Once an MVF is determined, an MC cardiac reconstruction can be performed at a chosen reference phase using the acquired cone-beam projection data.

The main goal of volumetric analytical and iterative reconstruction algorithms is to produce a 3D representation of the absorption distribution f of the scanned object. The correspondence between the discrete and continuous versions of the density function f can be established using a limited set of basis functions b placed on a 3D grid with N equidistant grid points, \vec{x}_i :

$$\tilde{f}(\vec{x}) = \sum_{i=1}^N \mu_i b(\vec{x} - \vec{x}_i), \quad (4.4)$$

where \tilde{f} indicate the discrete density function, and the set of numbers μ_i are the coefficients of expansion which describe the function \tilde{f} relative to the chosen basis set $b(\vec{x} - \vec{x}_i)$. In [69] a detailed investigation on how different sets of basis functions can influence the quality of the images is presented.

In this work, the Kaiser-Bessel basis functions (also called blobs) are used [68]. These spherically symmetric basis functions are spatially and frequency limited, and have many advantages compared to classical voxels, *e.g.* their appearance is independent of the source position [68]. The standard parameters are used for the Kaiser-Bessel basis functions ($m=2$, $a/g=2.00$, and $\alpha=10.4$, with grid increment g), which satisfy the frequency criteria described in [76].

The forward projection, \tilde{p}_j^n , through an intermediate image at iteration n , can be written for a detector pixel, j , as

$$\tilde{p}_j^n = \sum_{i=1}^N A_{ji} \mu_i^n \quad j = 1, 2, \dots, M. \quad (4.5)$$

This means, that in the forward projection, the contribution, A_{ji} , of each blob to the detector pixel, j , has to be determined. Ziegler et al. [147] proposed a method for calculating the A_{ji} weights. In the first step, the center of each blob is projected onto the detector. The footprint of a blob, which consists of all parallel line integrals through the volume element, is magnified and centered at the projected blob-center on the detector. The magnification of the volume element is given by the ratio of

the source-detector to source-blob distance. In a last step, the convolution of the footprint with the detector pixels is performed, which determines the weights A_{ji} .

Generally, in an iterative reconstruction method, the image is iteratively updated by backprojecting the difference (or ratio) between a calculated projection \tilde{p}_j^n and the corresponding measured projection p_j . In this work, an aperture weighted cardiac modified version of the Simultaneous Algebraic Reconstruction Technique [4] (gated AWSART) is used [149].

For an ECG-gated AWSART, one iterative step ($n \mapsto n + 1$) can be summarized by the following equation:

$$\mu_i^{n+1} = \mu_i^n + \frac{\lambda}{\sum_{j \in S_m} a_{ji} w_j^c w_j^a} \sum_{j \in S_m} \frac{p_j - \tilde{p}_j^n}{\sum_i a_{ji}} a_{ji} w_j^c w_j^a, \quad (4.6)$$

where a_{ji} indicates a backprojection weight [147], and w_j^c denotes a cardiac gating window weight, which is introduced for each projection p_j in the reconstruction algorithm in order to select data belonging to the same cardiac phase. In [86] a study on the effect of various gating function shapes on the image quality was shown. For the iterative reconstructions presented in this work, a rectangle with smooth edges (bump) shape is applied [86].

In helical cone-beam CT the object points can enter and leave the cone, this can produce artifacts in the reconstructed images. Empirically, it was found that these artifacts can be reduced by adding an aperture weighting function w_j^a , for each detector pixel, j , in the back projection formula [57, 149]. For the reconstructions presented in this contribution, a \cos^2 aperture weighting function is used [39, 57, 149].

All the measured projections are collected in different ordered subsets S_m . Once all subsets are processed, one iteration is completed. The ordering scheme chosen for the subsets S_m significantly affects the convergence speed of the algorithm. In this work, the projections of each subset S_m are selected equiangularly within each gating window, and the subset sequence is determined randomly [28].

The reconstruction process can be controlled by the relaxation parameter λ . It is selected to be $\lambda = 0.8$, which in previous works [39, 40, 147] has shown to lead to good results.

In case of blob-based MC iterative reconstruction of a moving object (*e.g.* the heart, the lungs), the projection model proposed in [147] neglects the motion of the blob itself and the change of its volume caused by the existence of a divergent MVF (Eq. 4.3). The non-vanishing divergence of the MVF results in a non-equidistant grid with several gaps between the blobs. In a prior work, Isola et al. [39] have shown as these gaps could produce streak artifacts in the MC reconstructed images. Hence, to reduce these artifacts, Isola et al. [39] proposed an MC modified version of the gated AWSART method (MC gated AWSART), where initially each blob center is moved accordingly to its MVF as given in Eq. 4.3, then an efficient blob adaptation is performed by changing the individual blob-size and its footprint on the detector depending on the neighboring blobs positions. This method is applied for the MC reconstructions presented in this chapter.

The well known large computation time of iterative reconstruction continues to be a limiting factor which still limits its application in clinical fields. This issue

is dramatically increased when a high resolution image reconstruction is required. Basically, the long computation time of an iterative reconstruction is caused from its necessity that a field-of-view (FOV) has to be reconstructed that covers the whole absorbing volume. Only then the calculated forward projections will be identical to the projections measured by the scanner. Since in many clinical cases, the ROI is smaller than the volume that is irradiated, *e.g.* coronary arteries angiographies, an ROI reconstruction [37, 149] can be an efficient solution to speed up the iterative image reconstructions.

In this work, the iterative ROI reconstruction framework proposed by Ziegler et al. [149] is applied.

4.3 Experiments and results

In this section, experiments on clinical data are performed to evaluate our proposed MC iterative reconstruction method. The results are compared with standard non motion-corrected gated AWSART reconstructed images, and with results obtained with a manual coronary artery motion estimation method.

4.3.1 Clinical cases and helical cone-beam CT scanners

The MC iterative ROI reconstruction method is applied to three clinical cardiac cases (A-C). Projection data are acquired using a Brilliance 40(64) CT scanner (Philips Healthcare, Cleveland, OH, USA). Heart rate statistics of the patients and parameters of the CT acquisition and reconstruction are listed in Table 4.1. In each clinical case, a suitable ROI is selected that is large enough to contain the RCA of the three patients (Table 4.1). Then, for the selected ROI, the AWC method is performed at phase points within the range 0 to 100% RR in steps of 5 % RR with a fixed gating window width of 22 % RR. Then, the mean absolute difference (MAD) is calculated between the subsequent reconstructed images of the 4D ROI data set. The determined MMs for all the investigated clinical cases are shown in Fig. 4.2.

4.3.2 Manually indicated start-end coronary centerline points

Given the previously determined MMs, the fast cardiac motion phases $P_r = 50\%$, 50% , and 55% RR are selected as iterative reconstruction reference phases for the case A, B and C, respectively. For all image reconstructions a gating window width of 40% RR is used. In all three cases, the volume reconstructed at the cardiac resting phase 40% RR (end systole) is chosen to select the pairs of start-end centerline points. Here, the RCA's *ostium* from the *aorta* and the *interventricular posterior branch* (PDA) are selected as starting and ending coronary centerline points, respectively.

In our implementation to non-rigidly register the manually indicated points to all other phases, the adaptive optimizer randomly selects 2000 image-samples at each optimization's iteration. The stochastic gain settings are automatically estimated by this optimizer. For the multi-resolution approach 4 levels are used. The images are smoothed using Gaussian blurring with standard deviation dependent on the resolution level, followed by a downsampling step, to reduce memory consumption. The

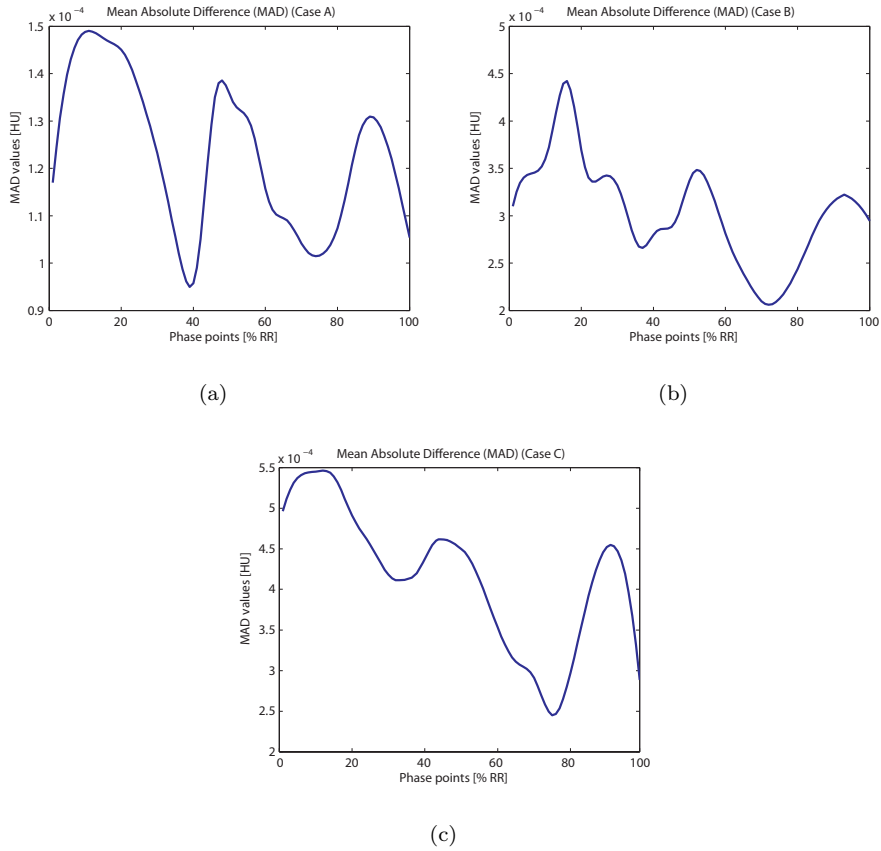


Figure 4.2. The MMs of the three clinical cases A, B and C. The MADs ((a),(b),(c)) are presented. For a smoother representation of the MAD curves, a cubic spline interpolation was used.

Table 4.1. CT scanning, AWSART reconstruction, and patient parameters

Clinical case	A	B	C
Table feed [mm]	5.0	8.0	8.0
Relative pitch	0.2	0.2	0.2
Collimation[mm]	40×0.625	64×0.625	64×0.625
Rotation time [s]	0.42	0.42	0.42
Tube voltage [keV]	120	120	120
Anode current [mA]	333	333	476
Mean heart rate [bpm]	55	56	61
Minimum heart rate [bpm]	53	54	53
Maximum heart rate [bpm]	58	59	65
ROI radius [mm]	25	33	34
Reference phase [%RR]	50	50	55
Gating window width [%RR]	40	40	40
# Subsets	300	205	300
# Views per subset	100	100	100
# Iterations	15	15	15
λ	0.8	0.8	0.8
Cubic grid size [mm]	0.3	0.3	0.3

(isotropic) B-spline control point spacing is also dependent on the resolution level. At each resolution level 500 optimization iterations are performed. All the image registration’s settings are listed in Table 4.2.

Resolution	Gaussian blurring STD [voxel unit]	Downsampling factor	Control point spacing [mm]
0	4	8	80
1	2	4	40
2	1	2	20
3	0	1	10

Table 4.2. Parameters of the image registration multi-resolution approach. The Gaussian blurring standard deviation (STD) is given in voxel units, and a down-sampling factor of 1 equals the original image.

Since a reconstruction gating window width of 40% RR is used, 8 3D-3D registrations are needed. The computation time per registration was approximately 2 minutes on a desktop computer (2.66 GHz Intel Core2 Quad CPU, 3.25GB RAM).

4.3.3 Coronary motion-vector field estimation

Once the start and end point are available at each phase within the chosen reconstruction gating window, the method described in subsection 4.2.2 is applied to determine the corresponding RCA centerlines at the relatively quiet cardiac phases.

For the coronary artery centerlines extraction the parameters settings which have been found to be optimal by Metz et al. in [77] are utilized. The computation time per coronary centerline extraction was approximately 1 minute. The resulting centerlines at different quiet cardiac phases within [30-70]% RR for patient case B are shown in Fig. 4.3 (blue lines). For the clinical cases presented here, coronary centerlines extraction is not feasible in fast heart motion phases (*e.g.*, in case B at phase points 50

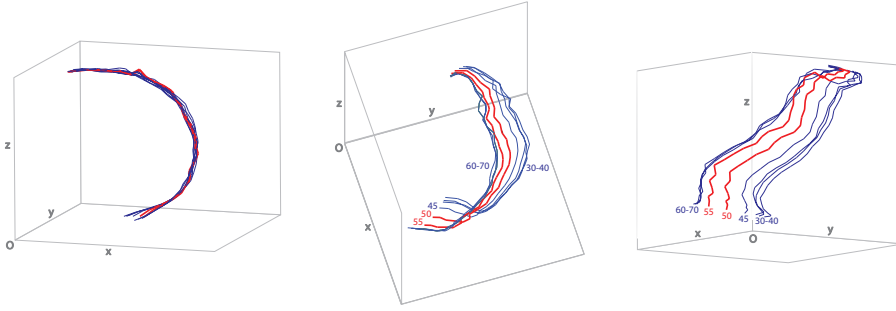


Figure 4.3. Three different views of a tracked 4D RCA centerline at phase points within the $[30-70]\%$ RR interval (case B). The blue lines indicate the RCA centerlines extracted at quiet cardiac phases by the minimum cost path-based approach (phase points within $[30-45]\%$ and $[60-70]\%$ RR). While, the red lines correspond to the cubic spline interpolated centerlines at the strong motion cardiac phases 50 and 55% RR.

and 55% RR). Therefore, the centerlines at these phases are determined by cubic spline interpolation [113] (red lines, Fig. 4.3). Subsequently, a cubic spline interpolation-based spatial-resampling is applied to recover corresponding equally-spaced points along the extracted coronary centerlines. Here, a spatial sampling interval of one voxel size (0.3 mm) is used. Then, these equidistant centerlines positions are used to determine the motion vectors of the coronary centerlines from the selected reference phase P_r to all the other phases P within the chosen ECG-gating window. Finally, a TPS warping is applied to produce a dense MVF for the complete cardiac ROI. This MVF is used to perform the MC iterative reconstructions presented in the following subsection. Due to the limited number of points, altogether spatio-temporal cubic spline interpolation and TPS warping took approximately 1 minute for each cardiac phase within the gating window.

4.3.4 Clinical validation

The gated AWSART and the MC gated AWSART reconstructed images and the corresponding 3D volume rendered images after 15 reconstruction iterations are presented in Fig. 4.4, 4.5 and 4.6. Moreover, the corresponding multi-planar reformatting (MPR) [10] images for the three clinical data sets are given in Fig. 4.7.

For clinical case A in Fig. 4.4, the AWSART gated reconstruction method fails to produce motion blurring artifact-free images of the RCA. As an example, in Fig. 4.4(a) and (j) the *ostium* of the RCA from the *aorta* and its *right conal branch* are clearly visible in the MC gated AWSART reconstructions (right) but strongly blurred in the AWSART gated reconstructed images (left). The same conclusions can be drawn for the reconstructed images in Fig. 4.4(f)-(i). Here, an RCA section and the complete vessel are very sharp in the MC reconstructions (right) and poorly visible in the non motion-corrected reconstructed images (left). Finally, the 3D volume ren-

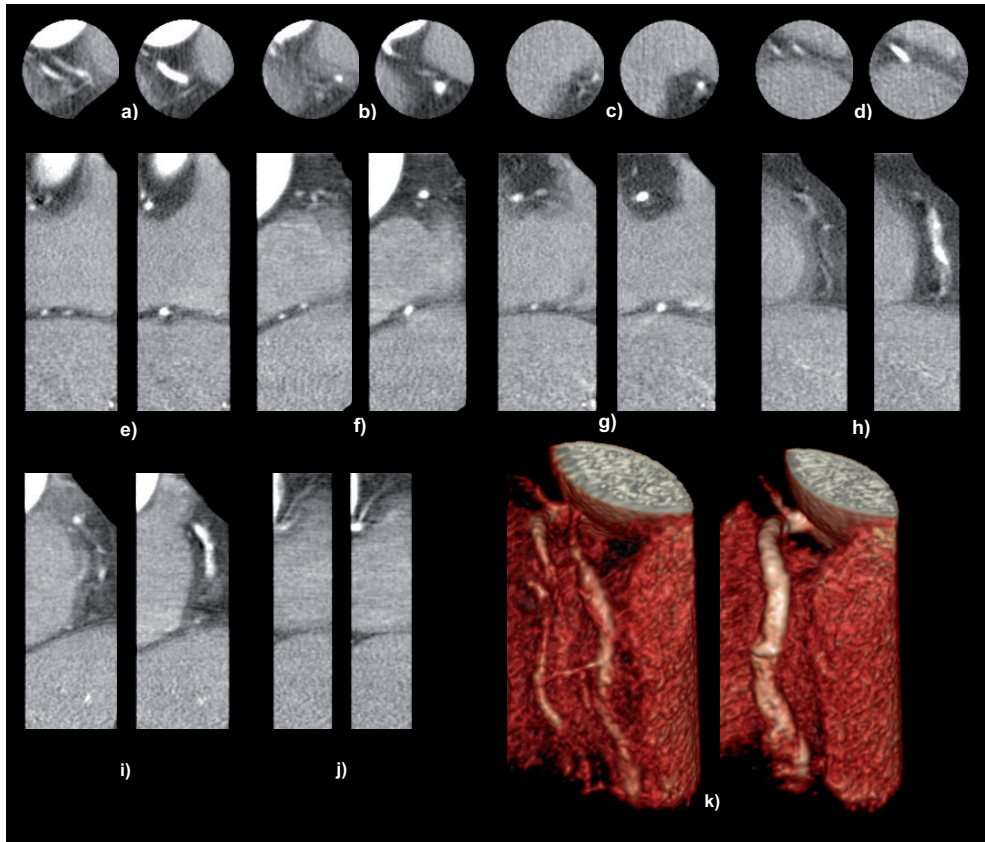


Figure 4.4. The axial (a-d), coronal (e,g,h), and sagittal (f,i,j) views and the corresponding 3D volume rendering (k). In order, the gated AWSART (left column) and the MC gated AWSART (right column) reconstructed images are shown. (Case A, at phase point 50% RR, gating window width of 40 % RR, 15 iterations, ROI's radius=25 mm, level=0 HU, window=500 HU).

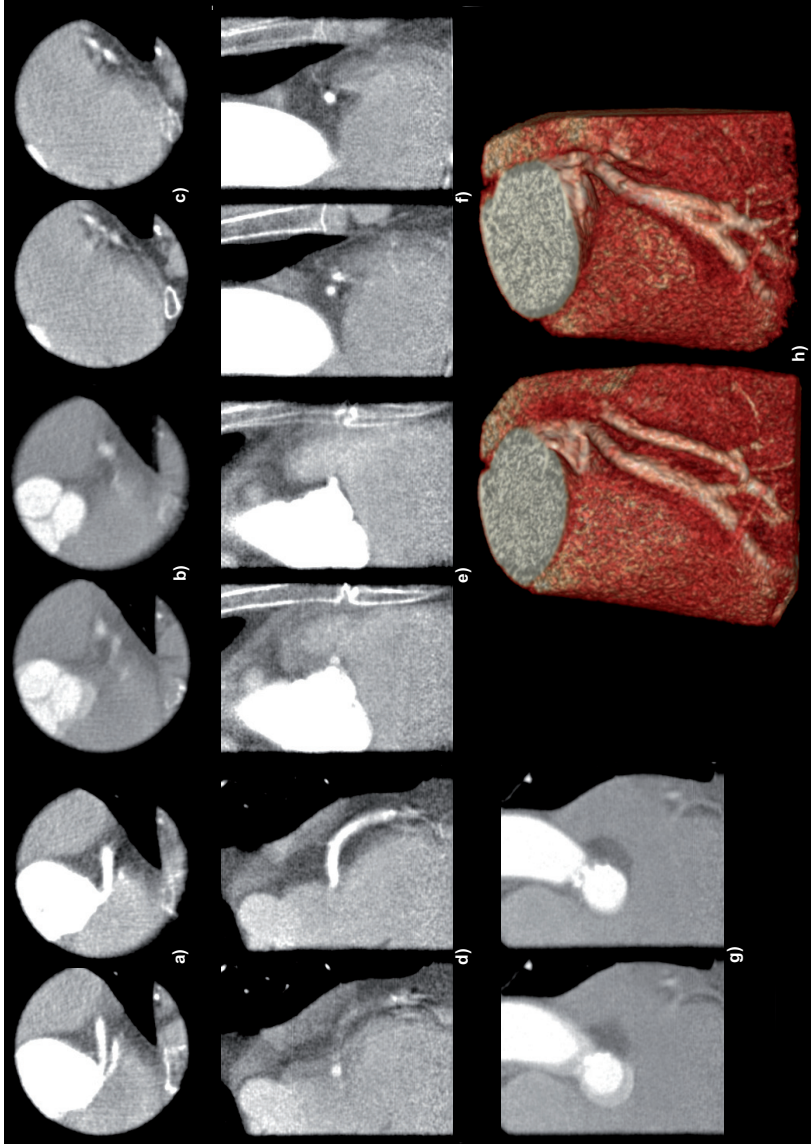


Figure 4.5. The axial (a-c), coronal (d-f), and sagittal (g-i) views and the corresponding 3D volume rendering (h). In order, the gated AWSART (left column) and the MC gated AWSART (right column) reconstructed images are shown. (Case B, at phase point 50% RR, gating window width of 40 % RR, 15 iterations, ROI's radius=33 mm, level=0 HU, window=500 HU in (a,d,e,f), and level=0 HU, window=1100 HU in (b,c,g)).

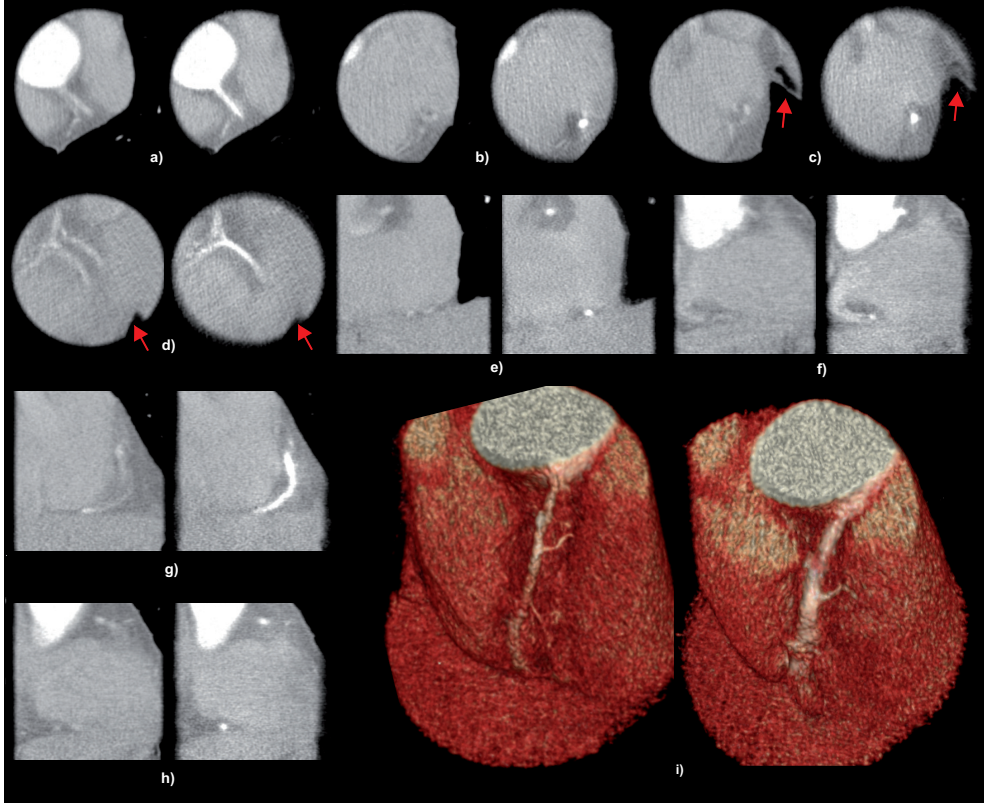


Figure 4.6. The axial (a-d), coronal (e) and sagittal (f-h) views and the corresponding 3D volume rendering (i). In order, the gated AWSART (left column) and the MC gated AWSART (right column) reconstructed images are shown. The red arrows indicate regions where the proposed motion estimation method fails to produce a good approximation of the local motion.(Case C, at phase point 55% RR, gating window width of 40 % RR, 15 iterations, ROI's radius=32 mm, level=100 HU, window=1000 HU).

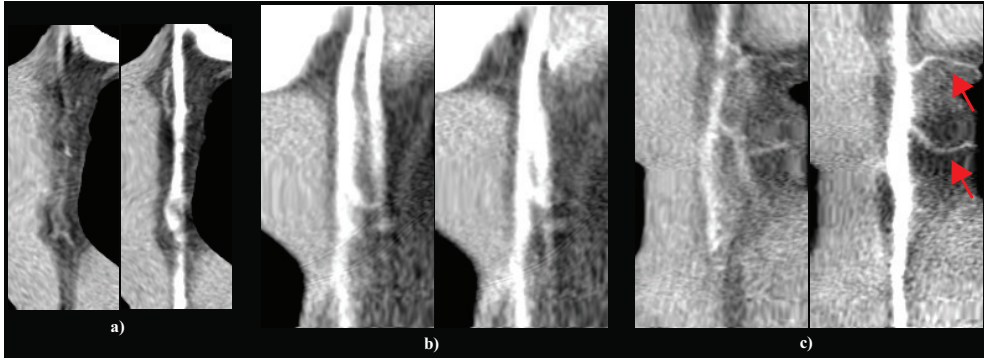


Figure 4.7. The MPR images of the gated AWSART (left) and MC gated AWSART (d) reconstructions showing the RCA vessel of the three clinical case A (a), B (b) and C (c) are shown. In (c), the red arrows indicate the RCA's marginal acute branches. (Level=0 HU, window=500 HU).

dering in Fig. 4.4(k) confirms the reduction of motion artifacts while using the MC gated AWSART method (right) compared to the corresponding AWSART gated reconstructed image (left) in which the motion artifacts are still visible.

Similarly, the effect of motion compensation on the reconstructed image quality is clearly visible for case B in Fig. 4.5 as well. Most noticeable is the improved image sharpness. Moreover, while an inconsistent ghost RCA is visible in the AWSART gated reconstructed images in Fig. 4.5 (a) and (f) (left), the MC reconstruction method results in a coherent RCA motion state where only a single coronary vessel is visible (Fig. 4.5 (a) and (f) (right)). The RCA's *marginal acute branch* is clearly visible in the MC reconstructions in Fig. 4.5 (c), while the non motion-corrected image looks strongly blurred (Fig. 4.5 (c) (right)). The coronary's *ostium* and the complete vessel in the MC images in Fig. 4.5 (d)-(e) (right) look sharper than the ones visible in the non motion-corrected images (Fig. 4.5 (d)-(e) (left)). Moreover, in Fig. 4.5 (b) and (g) (right) a sharper *aortic valve* and *aorta* are visible in the MC reconstructed images.

Finally, for clinical case C the RCA is recovered and well visible after MC reconstruction. This last clinical case also shows a weakness of the current approach. Although, the motion artifacts are reduced noticeably in all the presented images (Fig. 4.6), in some slices as *e.g.* Fig. 4.6(c)-(d) (right), residual motion artifacts still remain (red arrows). This is because the TPS extrapolation in the construction of the MVF fails to correctly represent the motion of cardiac regions which are relatively far away from the extracted RCA centerlines. Nevertheless, it is important to point out that the object of interest (i.e., the RCA) is clearly visible in all the MC reconstructed images. In Fig. 4.6(a)-(h) (left), the AWSART gated reconstructed images are strongly affected by the motion artifact and the coronary vessel is almost invisible. On the contrary, the corresponding MC gated AWSART reconstructed images (Fig. 4.6(a)-(h) (right)) show a very sharp *aorta* and RCA. Moreover, a ghost

PDA is visible in the non motion-corrected reconstruction in Fig. 4.6(d) (left), while in the MC reconstructed image, the same branch is well visible (Fig. 4.6(d) (right)). The RCA's *ostium* from the *aorta* in the MC gated AWSART image in Fig. 4.6(e)-(f) (right) looks sharper compared to the corresponding gated AWSART image in Fig. 4.6(e)-(f) (left). Finally, the 3D volume rendering in Fig. 4.6(i) shows that the MC framework allows to recover the patient's coronary artery better compared to the corresponding uncompensated ECG-gated reconstruction.

Similar conclusions can be drawn from the multi-planar reformatting (MPR) [10] images of the three clinical cases given in Fig. 4.7. The red arrows in Fig. 4.7(c) indicate the RCA's marginal acute branches which are not visible in the corresponding non-motion corrected MPR image.

4.3.5 Image quality assessment

In order to analyze the quality of the images more quantitatively, an image sharpness metric proposed by Wee et al. [142] is used. This statistical approach uses eigenvalues in image sharpness metric determination to provide robust assessment in the presence of various noisy conditions. Firstly, the input image is normalized by its energy to minimize the effects caused by image contrast. Secondly, the covariance matrix is computed from this normalized image before it is diagonalized using Singular Values Decomposition to obtain a series of eigenvalues. Since information on blur and additive random noise is carried by the least dominant eigenvalues, the image sharpness of the normalized image is determined by the trace of the first largest eigenvalues. Due to its formulation, the metric value decreases when there is an increment in image blurriness [142].

In this contribution, the image sharpness metric of the reconstructed images is calculated using the first 6 largest eigenvalues. In Fig. 4.8 the ratios between the image sharpness metric values of gated AWSART and MC gated AWSART reconstructed images of the three clinical cases A, B and C are presented, respectively.

The conclusions which were drawn from a visual inspection of the reconstructed images can be confirmed: the MC gated AWSART reconstructed images present a higher image sharpness compared to the gated AWSART reconstructions. Indeed, from the image sharpness ratios presented in Fig. 4.8, it is clearly visible as the non motion-corrected images present lower sharpness measures which lead to ratios smaller than unity.

4.3.6 Manual and semi-automatic coronary arteries motion estimation

In this subsection the proposed semi-automatic and a manual coronary artery motion estimation method [40] (Chapter 3) are compared. The MPR images of the corresponding MC gated AWSART reconstructions of the clinical case A are given in Fig.4.9. From the presented images, it can be observed that when using the semi-automatic motion estimation methodology better results are obtained (Fig. 4.9(a)-(b) (right)). Moreover, a manual motion estimation [40] requires that one experienced observer looking for a set of well known RCA's landmarks spatial positions through-

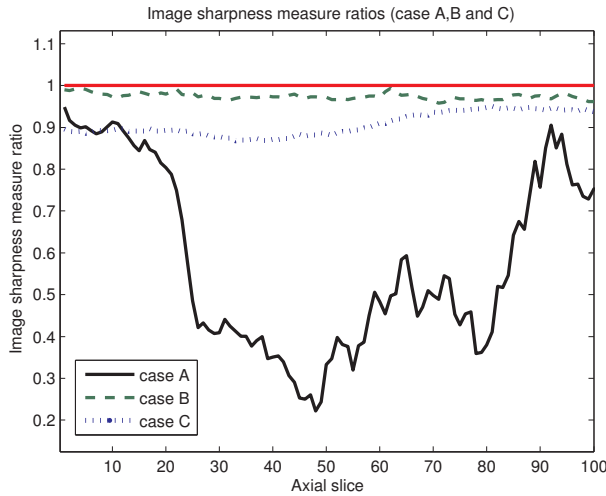


Figure 4.8. Image sharpness measure ratios of the clinical cases A (black line), B (dashed green line) and C (dotted blue line), respectively. Here, the image sharpness metric is determined for 100 axial slices of the gated AWSART and MC gated AWSART reconstructions containing the whole RCA. The red line indicates unity.

out the whole 4D image data set. This manual indication process can be very tedious, prone to errors, slow, and observer-dependent.

4.4 Discussion

In this chapter, a motion corrected ECG-gated iterative coronary artery reconstruction method was presented which uses a semi-automatic minimum cost path-based coronary centerline extraction to derive the motion vector field of the region of interest. Performance was visually assessed by comparing the resulting image quality in three clinical cases reconstructed with and without motion compensation, respectively. Furthermore, an image sharpness metric was evaluated to provide a more quantitative comparison of the reconstructed images.

The method requires a limited amount of user interaction to select the cardiac phase of reconstruction, and to manually indicate the start and end point of coronary centerline of interest in a chosen time-frame of the 4D data set. All other steps of the algorithm are fully automatic. The method lends itself to be applied for individual coronary vessel segment reconstruction. In the three clinical cases presented here, a general decrease of the motion artifacts was achieved using the proposed MC gated AWSART reconstruction method. The coronary artery of interest looks sharper which can be clearly noticed in Fig. 4.4-4.7 (right). Non motion-corrected ECG-gated iterative reconstructed images are strongly affected by motion artifact and the main coronary artery and its secondary branches are almost invisible (Fig. 4.4-4.7 (left)). In

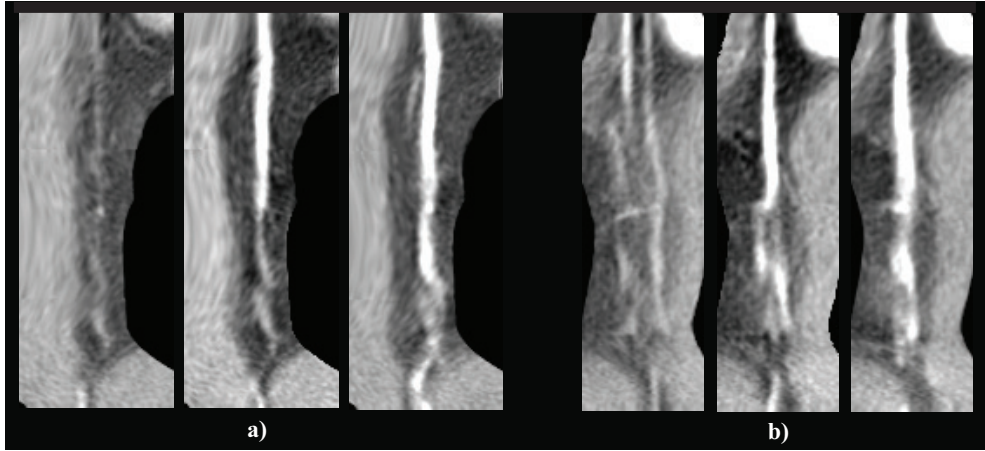


Figure 4.9. The MPR images of the gated AWSART (left), the MC gated AWSART (MVF estimated by manually landmarks indication) (center) and the MC gated AWSART (MVF estimated by coronary extraction) reconstructions are shown. In order a coronal (a) and sagittal (b) slices showing the RCA vessel of the clinical case A are given. (Level=0 HU, window=500 HU).

accordance to these qualitative observations, the quantitative image sharpness evaluations have confirmed that a general blurring artifact reduction is achieved inside the MC gated AWSART images (Fig. 4.8). Compared to a manual coronary artery motion tracking [40] (Chapter 3), the proposed semi-automatic coronary centerline extraction method has proved to be a faster and objective solution which did not require any landmarks human-indication (Fig. 4.9).

Although our method shows promising results, it also has some limitations. First, since the MVF of the ROI was determined from extracted RCA centerlines at multiple timepoints, the proposed method yielded only local improvements in the reconstructed images. For example, in case C the motion artifact was strongly reduced using TPS extrapolated MVF in the regions surroundings the extracted RCA centerlines (Fig. 4.6 (a)-(h) (right)). However, the same MVF failed to correctly represent the motion of cardiac regions which were relatively far away the extracted centerlines. This was proven by the appearance of motion artifacts visible in the MC reconstructed images in (Fig. 4.6 (c)-(d) (right), red arrows).

Second, the proposed MC iterative method consists of two steps. In the first step, the cardiac MVF is estimated by a semi-automatic minimum cost path-based coronary centerline extraction approach. The determined MVF is used to perform an MC iterative reconstruction in a second step. In a recent theoretical work, Schomberg [114] proposed a single-pass methodology which could allow the determination of the MVF directly during the reconstruction process. The success of a concept like this needs to be evaluated for the case of X-ray tomography using clinical data.

4.5 Conclusions

A coronary centerline extraction technique can be an efficient tool to determine the motion of the coronary artery of interest. Based on the estimated motion information, an MC ECG-gated iterative ROI reconstruction method was presented which effectively reduces motion artifacts in the reconstructed coronary CT images. Although iterative reconstructions are in general time-consuming, it was shown that their application is still feasible when only applied to a ROI. Visual and quantitative assessment of the method on three clinical cases confirm its potential.

Fully automatic non-rigid registration-based local motion estimation for motion-corrected iterative cardiac CT reconstruction

All truths are easy to understand once they are discovered; the point is to discover them.

— GALILEO GALILEI (1564 – 1642)

Abstract — A method for motion-corrected iterative CT reconstruction of a cardiac region of interest is proposed. Given a precomputed (non-motion compensated) gated 4D ROI image data set, a fully automatic elastic image registration is applied to recover a dense cardiac displacement field of the ROI from a chosen cardiac reference phase to a number of phases within the RR interval. Here, a stochastic optimizer and multi-resolution approach are adopted to speed up the registration process. Subsequently, motion-compensated iterative reconstruction using the determined motion field is carried out. For the image representation volume-adapted spherical basis functions (blobs) are used in order to take the volume change caused by a divergent motion vector field into account. The method is evaluated on phantom data and in four clinical data sets at a strong cardiac motion phase. Comparing the method to standard gated iterative reconstruction results shows that motion compensation strongly improves the image quality in these phases. A qualitative and quantitative accuracy study is presented for the estimated cardiac motion field. For the first time a blob-volume adaptation is applied on clinical data, and in the case of divergent motion it yields improved image quality.

5.1 Introduction

Cardiovascular computed tomography (cardiovascular CT) is increasingly used for diagnosis and therapy planning of cardiovascular disease. In cardiovascular CT the reconstructed images are analysed to detect possible abnormalities in cardiac anatomy or function. Early detection and evaluation of stenotic segments in the coronary arteries is an important clinical application of cardiac CT imaging, as it can be used for diagnosing coronary artery disease and guiding therapy options to prevent acute myocardial infarctions.

Up to now, ECG-gated CT reconstruction methods [26, 45, 47, 57, 86, 122] are the gold standard for the diagnosis of cardiovascular diseases. These techniques lead to images with reduced motion artifacts at the expense of an increased radiation dose to the patient and a limited temporal resolution. The ECG is used to select only the projections acquired during a time window centered in a chosen quiescent cardiac phase. For cardiac cone-beam CT, Manzke et al. [74] proposed an adaptive method to determine the optimal ECG-gating window width without user interaction. This method guarantees that all voxels receive data over an interval of at least π during the backprojection. In this way, the temporal resolution is optimized since only data from the smallest possible time window width is selected. Furthermore, this algorithm leads to a trade-off between temporal resolution and improved image signal-to-noise ratio (SNR), obtained using over scan data. For cardiac C-arm CT, an ECG-gated image reconstruction method is also feasible [62], but the slower rotation speed of the C-arm scanner leads to a temporal spread of the ECG-gated projections that is much higher compared to that produced by a clinical CT scanner. Within the automatically (or manually) determined time window the heart is assumed stationary. The frequent appearance of motion blurring artifacts in the reconstructed images proves this assumption to be violated.

A potential solution to reduce motion artifacts due to the heart pulsation is motion-compensated (MC) CT reconstruction [5, 39, 40, 71, 92, 98, 112, 136]. A fundamental pre-requisite for MC reconstruction is the knowledge of the three-dimensional (3D) object motion vector fields (MVF) from a reference phase of the heart pulsation to all other phases within the RR interval.

Several cardiac motion estimation methodologies have been proposed in literature [5, 40, 43, 95, 124, 136]. Usually, these methods attempt to find a correspondence between a limited number of automatically tracked or manually indicated anatomical landmarks from a given four-dimensional (4D) cardiac image data set. This procedure provides a sparse and irregular distribution of displacement vectors. To determine a dense MVF for the whole regular reconstruction grid, resampling is necessary. Generally, a spatial resampling interpolation method (e.g. Thin-plate-spline [6] or Nearest Neighbor by inverse distance weighting [116]) is used for this purpose. In order to improve accuracy, the estimation of a dense MVF directly from the image data would be of interest. This can for example be achieved using image registration techniques [14, 33, 55, 59, 70, 71, 98, 113], which have been frequently applied in the domain of motion analysis.

Elastic (or non-rigid) image registration techniques (EIR) based on B-spline basis functions [129] have been used extensively in biomedical imaging applications for the

monomodal or multimodal registration of pairs of clinical images [55, 59, 109], or for recovering directly a dense MVF of a chosen cardiac region of interest (ROI) [65]. In recent work, Prümmer et al. [98] proposed a 4D FDK-like algorithm that used a non-rigid 3D-3D image registration method for heart motion estimation.

The main drawback of EIR techniques is their long computation time, mainly caused by the calculation of the derivative of the similarity criterion for all degrees of freedom during each iteration of the optimization step. To solve the EIR problem, two classes of optimizers can be considered: *deterministic* methods [41, 97] that assume an exact knowledge of the criterion and its derivatives; and *stochastic* methods [52, 102, 118] which assume that only an approximation of the cost function is known. A popular search technique is the stochastic gradient descent method by Robbins-Monro [102]. Recently, with this approach, Klein et al. [55] have shown that the EIR computation time can be strongly decreased, without affecting the rate of convergence, accuracy, or robustness.

Iterative reconstruction algorithms are able to reconstruct images of transmission CT scans even in situations where the data elements are noisy and where only a sparse number of projections is available. Generally, iterative reconstruction methods may be divided into two groups. The first group including the algebraic reconstruction technique (ART) [25], solves a system of linear equations and does not take in account the statistics of the measurements. To the second group belong all the statistical iterative reconstruction methods, such as the convex Maximum Likelihood method (ML) [60], which take care of the photon statistics in the measurement, resulting in a higher SNR of the reconstructed images compared to the analytical reconstruction methods [85, 93, 126].

A well known drawback of conventional iterative reconstruction methods is the necessity that a field-of-view (FOV) has to be reconstructed that covers the whole volume, which contributed to the absorption. In the case of a high resolution reconstruction, this imposes very large memory and computation requirements during reconstruction. ROI reconstructions [149] can mitigate this problem.

In this chapter a method for MC iterative CT reconstruction of a cardiac ROI is proposed. Given a precomputed (non-motion compensated) gated 4D ROI image data set, a fully automatic elastic image registration is applied to recover a dense MVF of the ROI from a chosen cardiac reference phase to a number of phases within the RR interval. To speed-up the whole registration algorithm a stochastic Robbins-Monro optimization method and a multiresolution approach [82, 132] are adopted.

The method is evaluated on a dynamic cardiac phantom and on four clinical data sets performing reconstructions at a strong cardiac motion phase, and images of the right (RCA) and left (LCA) coronary arteries, of the left ventricle (LV), and of the aortic and mitral valves are presented.

This chapter is organized as follows: Section 5.2 describes in detail the implementation of the proposed motion compensation framework. Section 5.3 presents the results of the experimental validation of the method. Section 5.4 and 5.5 contain the discussion and conclusion, respectively.

5.2 Methodology

5.2.1 Introduction

The method for correcting the motion in cardiac CT is based on three subsequent steps: As a first step, the projection data are acquired in low-pitch helical acquisition mode together with the ECG and are reconstructed at different phase points. As a second step, the motion-vector field is calculated from the reconstructed images with the help of fully automatic elastic image registration. Finally, a motion-corrected iterative reconstruction is carried out for a reference phase using those projections, which cover the part of the cardiac cycle for which the motion-vector field has been determined. These steps are described in the following sections 5.2.2–5.2.5.

5.2.2 Generation of 4D image data sets

As an input for the determination of the motion-vector field, a 4D image data set is required. The images can be obtained by a low-pitch helical acquisition mode together with the ECG and a reconstruction at different cardiac phase points. This can be achieved, e.g., by an aperture weighted cardiac reconstruction (AWCR) [57].

In order to perform a 4D image reconstruction, the projection data have to be reconstructed at different phase points within the cardiac cycle. A list of N_r R-peaks at angular CT system positions $\phi_k^{R_p}$ is determined from the patient's electrocardiogram (ECG) recorded synchronously with the acquisition of the projection data. From the list of R-peaks, the phase points at angular positions ϕ_k^P can be determined using, for example, a fixed percentage $P \in [0, 1)$ of the RR interval. The same percentage is used for all heart cycles.

$$\phi_k^P = \phi_k^{R_p} + P \left(\phi_{k+1}^{R_p} - \phi_k^{R_p} \right) \quad \forall k = 1, \dots, N_p. \quad (5.1)$$

$N_p = N_r - 1$ phase points are obtained. A cardiac gating function with a width w_k is centered in each phase point P at angular position ϕ_k^P . The width w_k of the gating function determines which projection data from each cycle are used for the reconstruction and primarily determines the temporal resolution. In general, reconstructions of 3D images are performed at equidistant phase points P throughout the entire cardiac cycle with the smallest possible gating window width [74].

Due to the non-linearity of the cardiac motion during one single heart beat, and its rate variation between each beat, it can be expected that different motion blurring is observed in the gated reconstruction phases. A non-equidistant phases selection according to a typical heart motion model could lead to more homogeneous cardiac motion states. Nevertheless, to find a heart motion model which fit well to the cardiac motion of each patient is a non-trivial issue that goes beyond the scope of this work.

5.2.3 The elastic image registration (EIR) framework

The pre-requisite for performing a motion-corrected cardiac iterative reconstruction [39] of the acquired projection data is the existence of an MVF. For a volumetric cardiac reconstruction the MVF is represented by a $\mathbb{R}^3 \rightarrow \mathbb{R}^3$ mapping $\mathbf{m}(\mathbf{x}_i(R), R, P)$,

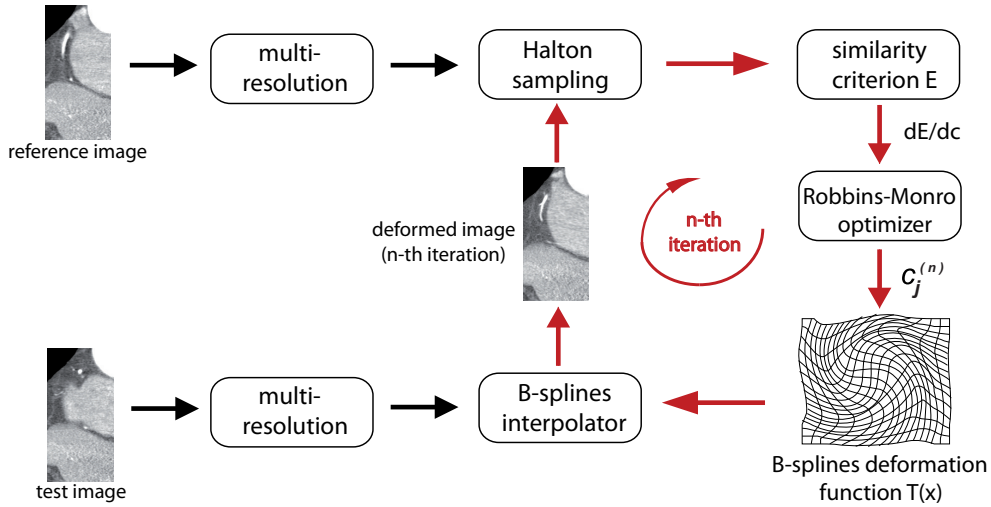


Figure 5.1. Flowchart of the EIR algorithm. First, given a set of input images at different cardiac phases, a multiresolution approach is applied and a set of gradually downsampled versions of the original images is created. Then, a B-spline interpolator is used to determine the continuous version of the discrete input images. Finally, an iterative optimization process is performed to determine the optimal B-spline coefficients c_j of the deformation function \mathbf{T} that minimize the similarity criterion E .

which displaces each grid point $\mathbf{x}_i(R)$ at a reference heart phase R to a new position $\mathbf{x}_i^*(P)$ in an arbitrary heart phase P by

$$\mathbf{x}_i^* = \mathbf{x}_i^*(P) = \mathbf{x}_i(R) + \mathbf{m}(\mathbf{x}_i(R), R, P), \quad (5.2)$$

where $R \in [0, 1]$ is the selected reference percentage of the RR interval, and $i = 1, 2, \dots, N$ with $N = N_x N_y N_z$ and N_x , N_y , and N_z are the number of grid points in x , y , and z directions, respectively.

Given a reference image f_r and a test image f_t , the EIR finds a correspondence function $\mathbf{T} : \mathbb{R}^3 \rightarrow \mathbb{R}^3$, which relates points in the test image f_t to the reference image f_r (Fig. 5.1). A minimization problem is solved to determine the deformation field \mathbf{T} which minimizes an image similarity measure that is computed for each grid position in the reference f_r and warped test $f_w(\mathbf{x}) = f_t(\mathbf{T}(\mathbf{x}))$ images. In our implementation \mathbf{T} is modeled using cubic B-splines [109, 129–131].

5.2.3.1 B-spline interpolation

The 3D deformation function \mathbf{T} is described by uniformly spaced cubic B-spline:

$$\mathbf{T}(\mathbf{x}) = \mathbf{x} + \sum_{\mathbf{j} \in J_c} c_{\mathbf{j}} \beta_3(\mathbf{x}/\mathbf{h} - \mathbf{j}), \quad (5.3)$$

where β_3 is a 3D tensor product of 1D centered cubic B-spline, J_c is a set of parameter indices, and $\mathbf{h} = (h_x, h_y, h_z)$ is the knot spacing. The scale parameter \mathbf{h} can be used to set the desired node spacing, which determines the level of smoothness of the deformation field \mathbf{T} . The second term in Eq.5.3 corresponds to the MVF from the reference to the test image.

5.2.3.2 Similarity measure and invertibility

Since here a mono-modal image registration is required, the *sum of squared differences* (SSD) is used as similarity measure. The SSD metric relies on the assumption that intensity representing homologous point must be the same in both images. The SSD measure is defined by

$$E_c^S = \sum_{i=1}^N (f_r(\mathbf{x}_i) - f_w(\mathbf{x}_i))^2, \quad (5.4)$$

Due to the high degrees of freedom, EIR is inherently an ill-posed problem and could lead to unrealistic folding of the deformation fields in the absence of suitable constraints [14]. Since the human organ and tissue motion is invertible, one important physical constraint for the estimated deformation \mathbf{T} is that it should be invertible as well. By the inverse function theorem [108], the invertibility is guaranteed if the Jacobian $\det J_{\mathbf{T}}(\mathbf{x}) \neq 0 \ \forall \mathbf{x}$. Moreover, since the determinant is continuous in the spatial domain, $\det J_{\mathbf{T}}$ must be positive since it is assumed that there are regions with identity transformations (i.e. $\det J_{\mathbf{T}}(\mathbf{x}) = 1 \ \forall \mathbf{x}$). Penalty functions have been often used to prevent Jacobian determinant from being negative [53, 104, 109]. For unconstrained optimization it is useful to add a penalty function $M(\mathbf{c})$ to the similarity measure E_c^S , and look for a minimum of the combined criterion

$$E_c^M(\mathbf{c}) = E_c^S(\mathbf{c}) + \gamma M(\mathbf{c}), \quad (5.5)$$

where E_c^M is the criterion to be optimized, γ is the regularization parameter, and \mathbf{c} is the vector of the parameters $c_{\mathbf{j}}$ describing the deformation function \mathbf{T} (Eq. 5.3).

For the 3D registrations presented in this chapter a *topology-preserving smooth* penalty function $M(\mathbf{c})$ proposed by Chun et al. in [12] is used, and reads

$$\begin{aligned} M(\mathbf{c}) = & \sum_{l \in \{x, y, z\}} \sum_{i, j, k} \\ & \left[p \left(\mathbf{c}_{i+1, j, k}^l - \mathbf{c}_{i, j, k}^l; \varsigma_1^{l, x}, \varsigma_2^{l, x} \right) \right. \\ & + p \left(\mathbf{c}_{i, j+1, k}^l - \mathbf{c}_{i, j, k}^l; \varsigma_1^{l, y}, \varsigma_2^{l, y} \right) \\ & \left. + p \left(\mathbf{c}_{i, j, k+1}^l - \mathbf{c}_{i, j, k}^l; \varsigma_1^{l, z}, \varsigma_2^{l, z} \right) \right], \end{aligned} \quad (5.6)$$

where $\varsigma_1^{l,r} = h_l k_l$ for $\forall r \in \{x, y, z\}$, $\varsigma_2^{l,r} = h_l k_l$ for $\forall r \neq l$ and $\varsigma_2^{l,r} = h_l K_l$ for $\forall r = l$, k_l and K_l are positive constants, and p represents the following piecewise quadratic function:

$$p(t; \varsigma_1, \varsigma_2) = \begin{cases} \frac{1}{2}(t + \varsigma_1)^2, & t < -\varsigma_1 \\ 0, & -\varsigma_1 \leq t \leq \varsigma_2 \\ \frac{1}{2}(t - \varsigma_2)^2, & \varsigma_2 < t \end{cases}, \quad (5.7)$$

where the argument t denotes a difference between two adjacent deformation coefficients.

This penalty function encourages positive Jacobian determinants by bounding the differences of two adjacent deformation coefficients in the x, y, z direction. By constraining the differences only instead of the coefficients, even large deformations $\mathbf{T}(\mathbf{x})$ with gradients within the bounds are included in the search solution space. Compared to the direct Jacobian penalty methods, this approach has the advantages to enforce the invertibility on the continuous domain, it is memory-efficient, and finally it has faster computation because no interpolation for Jacobian values is needed [12].

5.2.3.3 Fast stochastic optimization methods

As shown in Eq. 5.3, the deformation function \mathbf{T} is represented by a summation of B-spline basis functions, where c_j denote the expansion coefficients. Given our parametric deformation model in Eq. 5.3, and the combined criterion in Eq. 5.5, the solution of the registration problem can be defined as the result of the following minimization:

$$\mathbf{c} = \operatorname{argmin}_{\mathbf{c}} E_c^M. \quad (5.8)$$

To find the optimal deformation T that minimizes the cost function in Eq. 5.5, a suitable optimization method should be applied.

In this work the stochastic gradient descent of Robbins-Monro [102] (RM) is used, since it has the advantage to decrease the computation time per iteration, without affecting the rate of convergence, final precision, or robustness [55].

The RM follows the same scheme as the deterministic gradient descent [97] with the distinction that the gradient of the cost function, $\nabla_{\mathbf{c}} E_c^M(\mathbf{c}^{(n)})$, is replaced by an approximation $\nabla_{\mathbf{c}} \tilde{E}_c^M(\mathbf{c}^{(n)})$, resulting in the following update rule:

$$\Delta \mathbf{c}^{(n)} = -\rho_n \nabla_{\mathbf{c}} \tilde{E}_c^M(\mathbf{c}^{(n)}). \quad (5.9)$$

The gain factor ρ_n can be defined as a decaying function of the iteration number n and in practice the following expression is often used [55, 119]:

$$\rho_n = \frac{a}{(n + A)^\alpha}, \quad (5.10)$$

with $A \geq 1$ and the user-defined constants $a > 0$ and $0 \leq \alpha \leq 1$.

A stochastic approximation of the derivative of the similarity criterion $\nabla_{\mathbf{c}} \tilde{E}_c^M$ can be determined by using a new, randomly selected subset of voxels in every iteration of the optimization process. In this way, a bias in the approximation error is avoided. This technique, commonly called *stochastic subsampling*, has been evaluated on non-rigid registration in Klein et al. [55].

For the EIRs presented in this chapter, the selection of uniformly distributed samples follows a quasi-Monte Carlo Halton sequence [27] (Fig. 5.1).

5.2.3.4 Multiresolution elastic image registration

A multiresolution approach [82, 132] can improve the robustness and the efficiency of the EIR algorithm. First, the problem is solved at a coarse level, with subsampled images and a deformation field with reduced number of degrees of freedom. Subsequently, the results are propagated to the next finer level. This iterative procedure will expand alternately the grids of the B-spline control points of the images and of the deformation field until the finest level is reached. In this work, the multiresolution approach uses 3D B-spline *reduce/expand* operators [132] of factor of two to build the pyramid (i.e. a set of gradually reduced versions of the original images and the deformation field), which is optimal in the L2-sense. As an example, in Fig. 5.2 a 2D-2D registration of the *Lena* image is shown.

5.2.4 Extraction of the cardiac motion vector fields

Since the second term in Eq. 5.3 represents the MVF from the *reference* to the *test* image, the EIR can be used to estimate the MVF between a pair of volumes for each grid position \mathbf{x}_i . Due to the severe motion artifacts in the images reconstructed at phases of fast cardiac motion, it is advantageous to apply the EIR only between images related to phases of relatively weak motion. In this way, it is possible to avoid the accuracy degradation of the motion estimation produced by the matching errors. To determine appropriate motion phases within the RR interval, a motion map (*MM*) technique is used [74, 113].

Hence, from the determined motion map the desired strong motion reference phase R and a limited set of quiescent motion phases Q , with $Q \in [0, 1)$, are selected. A temporary reference phase R^T , with $R^T \in [0, 1)$, is chosen from the set of quiescent phases. Therefore, in order to recover the relative MVFs, a number of 3D-3D EIRs are performed between the volumes reconstructed at the phase R^T and the other quiescent phases Q selected. A continuous 4D displacement vector $\mathbf{m}(\mathbf{x}_i(R^T), R^T, P)$ from the temporary reference phase R^T to all the arbitrary phases P within the RR interval is obtained by applying a cubic-spline interpolation using as knots all the EIR's MVFs computed previously.

After the last interpolation step, the MVF $\mathbf{m}(\mathbf{x}_i(R^T), R^T, R)$ from the temporary R^T to the actual reference phase R is available. Given the determined $\mathbf{m}(\mathbf{x}_i(R^T), R^T, R)$, it is possible to recover the inverse MVF $\mathbf{im}(\mathbf{x}_i(R), R, R^T)$ in the opposite direction from the actual R to the temporary R^T reference phase, by using a fixed-point-based iterative approach [11].

The displacement vector $\mathbf{m}(\mathbf{x}_i(R), R, P)$ from the reference phase R to all the arbitrary phases P in the RR interval is determined by:

$$\mathbf{m}(\mathbf{x}_i(R), R, P) = \mathbf{im}(\mathbf{x}_i(R), R, R^T) + \mathbf{m}(\mathbf{im}(\mathbf{x}_i(R), R, R^T), R^T, P). \quad (5.11)$$

Once the vector $\mathbf{im}(\mathbf{x}_i(R), R, R^T)$ is obtained for each grid position \mathbf{x}_i at the actual reference phase R , the corresponding codomain points \mathbf{s}_i can be determined

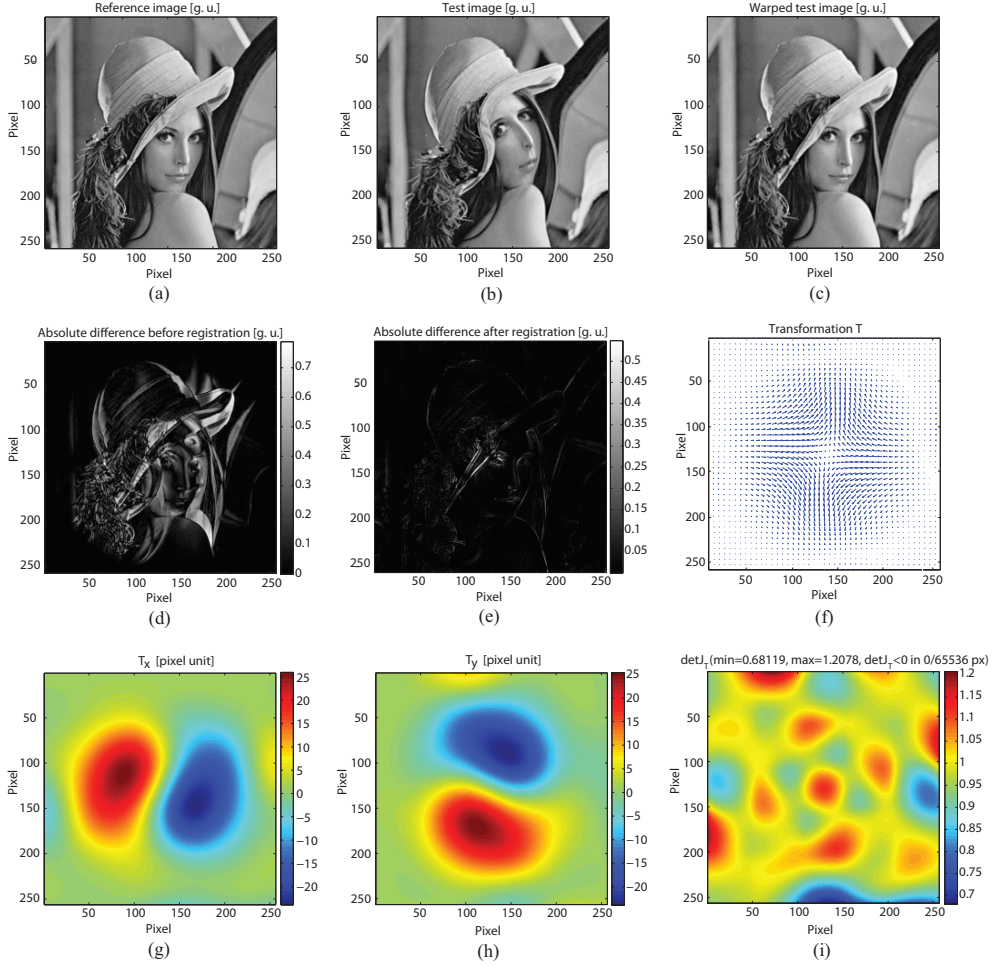


Figure 5.2. The *Lena* 2D-2D registration. In order, in the top row the reference (a), the test (b) and the warped test (c) images are shown. In the middle row the absolute difference images before (d) and after (e) the registration, and the estimated transformation T (f) are given. While, in the bottom row the x (g) and the y (h) components and the determinant of the jacobian matrix of T ($\det J_T$) (i) are presented. Here g.u.=grayscale unit. (Image size: 256×256 , deformation size: 8×8 , 3 resolution levels, RM optimizer, $a = 3500$, $A = 51$, $\alpha = 0.602$, 2000 iterations per resolution level, 2000 randomly selected voxels per iteration, topology-preserving regularizer, $\gamma = 0.001$).

on the grid at the quiescent temporary reference phase point R^T (see Fig. 5.3, middle grid). Since the vectors $\mathbf{m}(\mathbf{x}_i(R^T), R^T, P)$ are available for the only grid positions \mathbf{x}_i , in a second step a B-spline interpolation is applied to recover the $\mathbf{m}(\mathbf{s}_i(R^T), R^T, P)$ values at off-grid positions \mathbf{s}_i . Finally, the $\mathbf{m}(\mathbf{x}_i(R), R, P) = \mathbf{t}_{P,i}$ can be easily determined by summing the $\mathbf{im}(\mathbf{x}_i(R), R, R^T)$ and the $\mathbf{m}(\mathbf{s}_i(R^T), R^T, P)$ (Fig. 5.3).

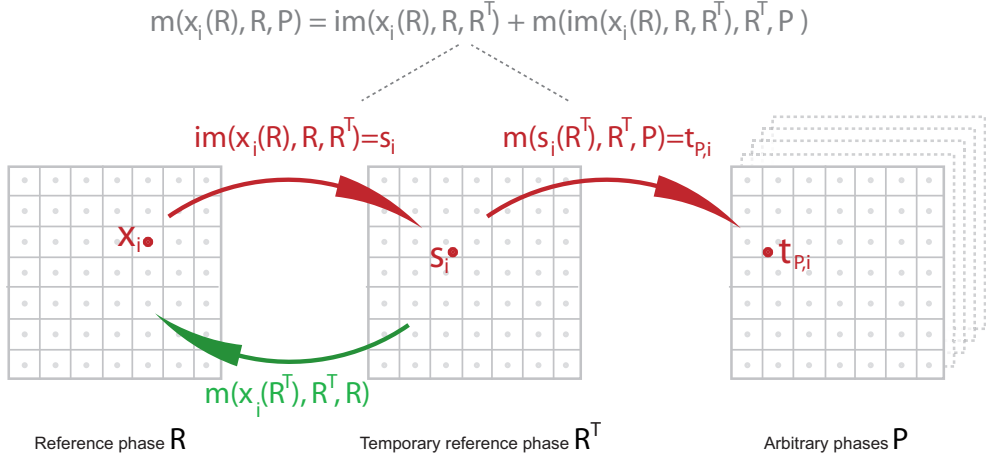


Figure 5.3. Extraction of the MVF $\mathbf{m}(\mathbf{x}_i(R), R, P)$ from the actual strong moving reference phase R to all the arbitrary phase points P within the RR interval in two steps.

5.2.5 Motion-corrected image reconstruction with SART

Once an MVF is determined, an MC cardiac iterative reconstruction can be performed for the cone-beam projection data, which are acquired with a CT scanner equipped with a rigidly coupled focus-centered 2D detector and a X-ray source moving on a helical path around the object.

Volumetric CT reconstruction algorithms determine the density absorption function f of the object irradiated using a set of 2D projections measured at different angles. A linear combination \tilde{f} of a limited set of basis functions b can be used to represent the continuous function f :

$$\tilde{f}(\mathbf{x}) = \sum_{i=1}^N \mu_i b(\mathbf{x} - \mathbf{x}_i), \quad (5.12)$$

where $\mathbf{x} = (x, y, z)$, and the basis functions b are placed on a 3D grid with N grid points. The set of parameters μ_i are the coefficients of expansion which describe the function \tilde{f} relative to the chosen basis functions $b(\mathbf{x} - \mathbf{x}_i)$. Following Lewitt [69] in this work, the Kaiser-Bessel basis functions [68] are used. These spherically symmetric

basis functions (also called blobs) are spatially limited and effectively frequency limited. The standard parameters are used for the Kaiser-Bessel basis functions, which satisfy the frequency criteria described in [76]. Blobs as basis functions have many advantages compared with simple cubic voxels, e.g. their appearance is independent of the source position [68].

The main goal of iterative CT reconstruction is to find the optimal set of coefficients μ_i that minimizes the difference (or ratio) between the measured p_j and calculated $\tilde{p}_j^{(n)} = \sum_{i=1}^N A_{ji} \mu_i^{(n)}$ projections, where A_{ji} are the elements of the system matrix, n is the iteration number, and $j = (1, 2, \dots, D)$ are the detector pixels.

For the iterative ROI reconstructions presented in this chapter, an ECG-gated aperture weighted Simultaneous Algebraic Reconstruction Technique (SART) [4] is applied. The SART method is a modified version of the ART [25], which increases the speed of reconstruction. Here an entire cone-beam projection is back projected into the image. The update formula used during the backprojection step of the ECG-gated aperture weighted SART method (gated AWSART) can be written as

$$\mu_i^{(n+1)} = \mu_i^{(n)} + \frac{\lambda_n}{\sum_{j \in S_m} a_{ji} w_j^c w_j^a} \sum_{j \in S_m} \frac{p_j - \tilde{p}_j^{(n)}}{\sum_i a_{ji}} a_{ji} w_j^c w_j^a. \quad (5.13)$$

Here, a_{ji} indicates a backprojection weight [147], and w_j^c represents a cardiac gating window weight, which is introduced for each projection p_j in the reconstruction algorithm in order to select data belonging to the same heart phase. The effect of various gating function shapes on the images quality has been previously studied [86]. For the 3D reconstructions presented in this work, a rectangle with smooth edges (bump) shape is used for the cardiac-gated iterative reconstructions [86].

In helical CT the object points can enter and leave the cone, which can lead to artifacts in the reconstructed images. Empirically, it was found that these artifacts can be reduced by adding an aperture weighting function w_j^a , for each detector pixel, j , in the back projection formula [57, 149]. For the reconstructions presented in this work, a \cos^2 aperture weighting function is used [39, 57, 149].

One update of the ECG-gated SART algorithm requires to sum simultaneously over all the projections in one subset S_m . The projections of one subset are selected at equal angles and the order is determined randomly. A random sequence is used because it was found to perform very similar to more sophisticated ordering schemes [28].

The relaxation parameter, $0 < \lambda_n < 2$, controls the speed of convergence. Based on empirical evaluation, $\lambda_n = 0.8$ is chosen, which gave reasonable results.

In this work, the MC gated AWSART method proposed by Isola et al. [39] is adopted to reconstruct the selected cardiac ROI at the chosen reference phase R .

To determine the forward projection, \tilde{p}_j , the A_{ji} contribution of each blob to the detector pixel, j , have to be determined. In case of a divergent beam, care needs to be taken to correctly sample the blobs; e.g. blobs which are close to the source, have a different contribution to forward and back projection than more distal blobs. Ziegler et al. [147] presented a blob sampling method motivated by the acquisition geometry: due to the divergent X-ray geometry, the spherically symmetric volume elements are magnified depending on their distance to the source. The convolution of

the magnified volume elements with the sensitive detector areas defines the weights A_{ji} .

However, in case of MC reconstruction of a moving object (e.g. the heart, or the lungs), the motion of the blob itself and the change of its volume caused by the existence of a divergent MVF (Eq. 5.2) is neglected. Isola et al. in [39] have shown that the non-vanishing divergence of the MVF yields a non-equidistant set of grid points, and an inconsistency in the line integral calculation which produces streak artifacts in the reconstructed images. Therefore, in case of MC reconstruction, a modified forward and back projection model was proposed which adapts the individual blob volume and its relative footprint on the detector in such a way that the representation of the image becomes more homogeneous. Phantom simulations have shown that this approach improves MC reconstruction quality [39]. An initial validation of the method on clinical data is presented in the subsection 5.3.6.

Iterative reconstruction is associated with high computational costs, especially in case of high resolution image reconstructions over the entire FOV and multiple time phases. Usually, in many clinical cases, the ROI is smaller than the volume that is irradiated, e.g. in coronary CT angiography, the ROI is often restricted to only one or more of the coronary arteries. Hence, an ROI reconstruction can be an efficient solution to increase the speed of iterative or analytical image reconstructions. For filtered back-projection (FBP) reconstruction methods [9, 51, 128], an ROI reconstruction is possible without additional efforts. To the contrary, an iterative reconstruction requires that an FOV has to be reconstructed that covers the whole volume, which contributed to the absorption. Only then the forward projections can be identical to the raw measurements. In this work, in order to recover the sinogram of only the ROI from the complete clinical raw measurements, a four-steps method as proposed by Ziegler et al. in [149] is adopted. This method consists of four consecutive steps and it is briefly described in the following. The first step includes an analytical FBP reconstruction of the whole FOV. In the second step the ROI is removed from the image of the previous step by setting the corresponding grid values to zero and performing a reprojection through this image on the same trajectory and detector geometry as the measurement. The sinogram, which results of the reprojection, is subtracted from the measurement data set in a third step. These processed projections contain the projections of the ROI only, which are taken for the iterative ROI reconstruction in a fourth step [149]. In case of MC gated iterative volume reconstruction, the last step can be replaced with an MC iterative ROI reconstruction method.

5.3 Experiments and results

To evaluate our MC reconstruction method a series of experiments was performed. First, a method validation on a dynamic cardiac phantom is given. Second, a consistency check of the estimated MVF, and a qualitative evaluation of the reconstructed images for human cases are presented. Subsequently, coronary artery reconstructions of three patients are shown. Finally, a clinical validation of the blobs volume-adaptation method proposed in [39] is given for the MC iterative reconstruction of the LV of a fourth patient.

5.3.1 CT scanning and reconstruction settings

The phantom data were simulated for a scanner with 16 detector rows of 0.75 mm projected height and a helical scan with a relative pitch of 0.2. All the human data sets were acquired on a Brilliance 40(64) CT scanner (Philips Healthcare, Cleveland, OH, USA). In order to perform ECG-gated reconstructions, an ECG of the patients was recorded simultaneously with the CT acquisition. Approximately 10 heart beats are expected in the full scan of each patient. Further scanning and reconstruction parameters are listed in Table 5.1.

Table 5.1. CT scanning and AWSART reconstruction parameters

Cases	A	B	C	D	Phantom
Pitch [mm]	5	8	8	8	2.4
Relative pitch	0.2	0.2	0.2	0.2	0.2
Collimation	40×0.625 mm		64×0.625 mm		16×0.75 mm
Rotation time [s]	0.42	0.42	0.42	0.42	0.42
Tube voltage [keV]	120	120	120	120	120
Anode current [mA]	333	333	333	333	119
Mean heart rate [bpm]	55	56	68	75	64
Minimum heart rate [bpm]	53	54	65	73	64
Maximum heart rate [bpm]	58	59	71	83	64
ROI radius [mm]	25	33	29	37	-
Reference Phase [%RR]	50	50	60	20	40
Gating wind. width [%RR]	40	40	40	40	40
# Subsets	300	205	192	274	363
# Views x subset	100	100	100	100	100
# Iterations	10	10	10	10	10
λ_n	0.8	0.8	0.8	0.8	0.8
Cubic grid size [mm]	0.3	0.3	0.3	0.3	0.5

5.3.2 Phantom study

For the simulations performed in this work, a dynamic cardiac phantom modelled with ellipsoids and two tori to simulate coronary arteries was used. The heart size was modified dynamically according to a model ventricular volume curve derived from clinical cases [140] (Fig. 5.4). This volume curve was applied to every cardiac cycle of the phantom with a constant rate of 64 bpm.

The first step of this phantom evaluation was the 4D image data set reconstruction. The AWCRT method was performed at phase points P within the range 0 to 100% RR in steps of 5 % RR with an optimized gating window width [74]. The systolic phase point $R=40\%$ RR was selected as reference reconstruction phase. This rapid motion phase corresponds to the minimum of the ventricular volume curve in Fig. 5.4(b). Consequently, here a significant temporal cubic-spline interpolation error should occur. Thus, it is interesting to investigate how much this error can actually degrade the final MC reconstruction.

In order to apply the registration process, a subset of volumes reconstructed at slow motion phases Q located in the regions between $[20,35]\%$ RR and $[50,60]\%$ RR was selected. Among these quiescent phases a temporary reference phase $R^T=30\%$ RR was chosen. Therefore, six 3D-3D registrations were performed between the tem-

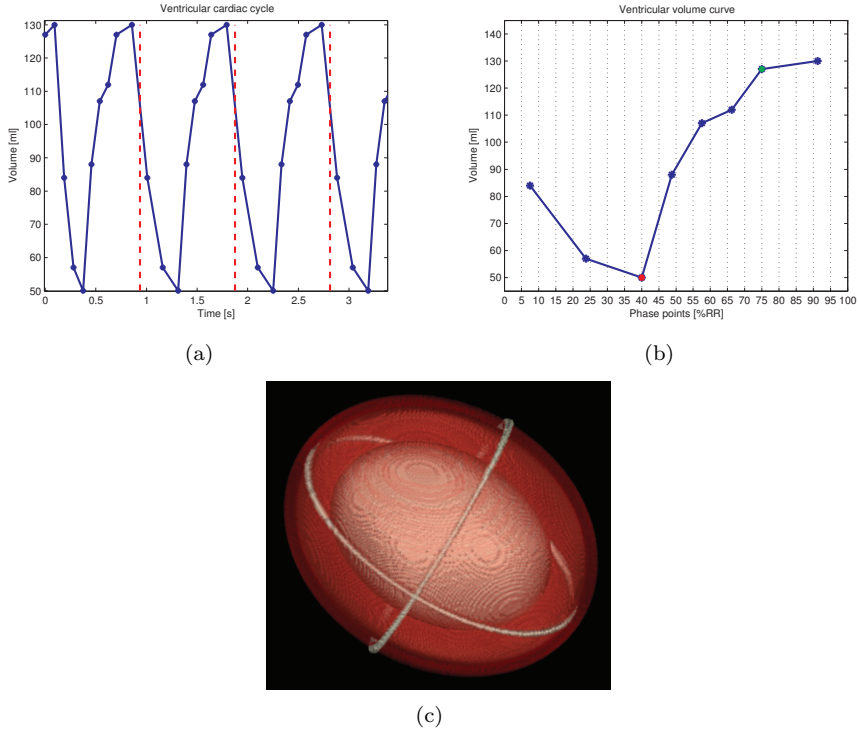


Figure 5.4. The dynamic cardiac phantom and the ventricular volume curve (see [140]). In (a), the red dashed vertical lines indicate the R-peaks, and the blue dots represent values from the model. In (b), the same volume curve values at the corresponding cardiac phases in one beating cycle are given. Here, the red and green dots indicate the systole (40% RR) and diastole (75% RR), respectively. While, in (c) a volume rendered image of the dynamic cardiac phantom is shown.

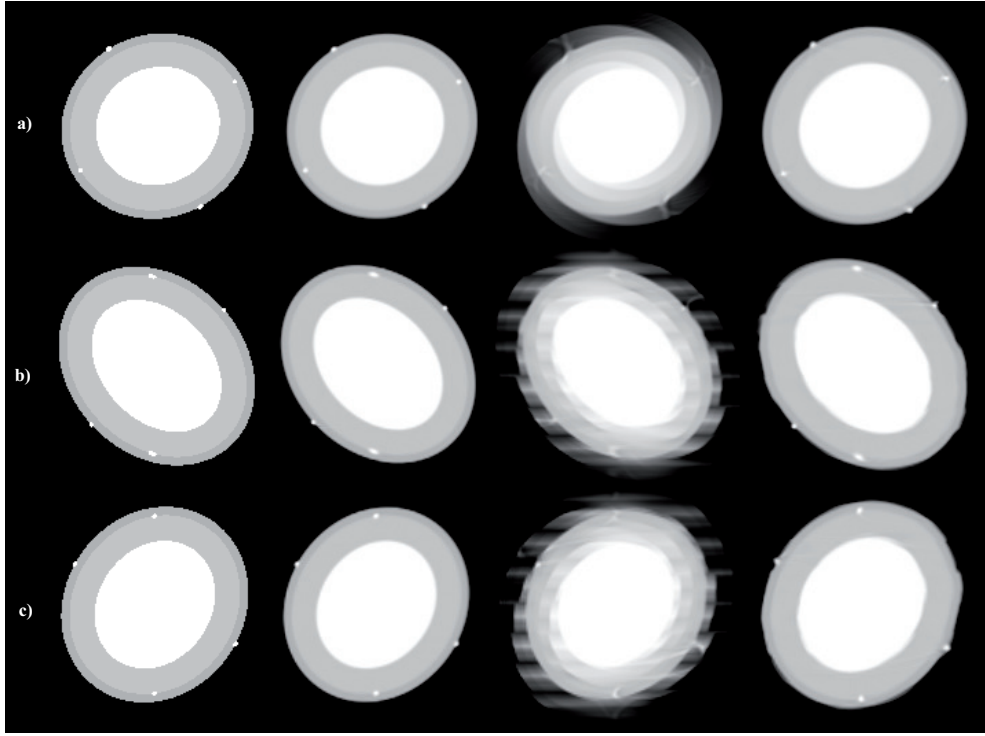


Figure 5.5. Phantom's axial (a), coronal(b) and sagittal (c) views. In order, the ground truth synthetic images at 40% RR (first column), the static (second column) and dynamic (third column) cardiac phantom's gated AWSART and the dynamic cardiac phantom's MC gated AWSART (fourth column) reconstructed images at phase point 40% RR with gating window width of 40% RR are shown. (after 10 iterations, Level=-200 HU, Window=1000 HU).

porary reference phase R^T and all the other quiescent phases Q (for the registration settings see the following subsection 5.3.3). A cubic-spline interpolation was applied to fill the MVF estimation gap at the strong motion phases 40% and 45% RR. Finally, the MVF were shifted to the actual reference phase $R = 40\% \text{ RR}$ following all the remaining steps explained in the subsection 5.2.4. Given the estimated MVF, an MC gated AWSART reconstruction was performed at phase 40% RR with a fixed gating window of 40% RR. For the sake of comparison, gated AWSART reconstructions of the static and dynamic heart phantom were performed at identical phase point and gating window width. These reconstructions are presented in Fig. 5.5, while quantitative image similarity measures are given in Table 5.2.

As shown in Fig. 5.5 (third column), the gated AWSART reconstruction performed at 40% RR with a gating window of 40% RR leads to an image where the ventricle shape and the coronary arteries are strongly blurred. To the contrary, the MC gated AWSART reconstruction in Fig. 5.5 (fourth column) produces a sharp

Table 5.2. Image similarity measures. The MAD and the normalized correlation coefficient (NCC) between the cardiac phantom ground truth images and the gated AWSART reconstructed images of the static and dynamic cardiac phantom, and the MC gated AWSART reconstructed images of the dynamic cardiac phantom in Fig.5.5 are presented. Moreover, the ventricle volume of each reconstructed heart phantom is given.

Method	Motion state	MAD [HU]	NCC [%]	Volume [ml]
Ground truth	Static	0.0	100.0%	50.0
gated AWSART	Static	4.5	99.5%	49.9
	Dynamic	64.9	90.7%	46.0
MC gated AWSART	Dynamic	33.5	92.0%	53.5

image where the ventricle shape and the vessels are well defined. By analysis of the image similarity measures in Table 5.2, it can be observed that the MC reconstruction presents better MAD and NCC values compared to the gated AWSART reconstructed image. The ground truth phantom ventricle has a volume of 50 ml at 40% RR, while in the MC reconstruction its measured volume is of 53.5 ml. This slightly bigger volume is due to the temporal cubic-spline interpolation error which has shifted the reference phase from 40% to 41% RR.

5.3.3 Cardiac motion estimation

In order to generate an *MM* a 4D ROI data set was required, hence an AWCRT method was performed at phase points P within the range 0 to 100% RR in steps of 5 % RR with an optimized gating window width [74]. Then, the mean absolute difference (MAD) was calculated between the subsequent reconstructed images of the 4D ROI data set. The determined *MMs* for all the clinical cases are shown in Fig. 5.6. The fast cardiac motion phases $R = 50\%$, 50% , 60% and 20% RR (red points in Fig. 5.6) were chosen as reference reconstruction phases for the cases A-D, respectively. In order to apply the registration process, a subset of volumes reconstructed at quiescent phases Q was selected (red intervals in Fig. 5.6). Generally, suitable cardiac slow motion phases Q are located in regions between $[0,5]\%$ RR, $[35,45]\%$ RR (*end systole*) and $[65,85]\%$ RR (*diastasis*). Among these quiescent phases a temporary reference phase R^T was selected. The phases $R^T = 70\%$, 70% , 75% and 30% RR (red stars in Fig. 5.6) were chosen for the cases A-D respectively. For the EIR step a 3-level multi-resolution approach was applied, and in each level the deformation field B-spline knot spacing h was empirically chosen every 12 blobs. Since no *a priori* knowledge was available about the deformation, according to Chun et al. in [12], the topology-preserving regularization parameters were chosen symmetrically. The regularization parameter γ in Eq.5.5, for all the four clinical data sets was set experimentally to $\gamma = 0.001$. For the RM optimizer, at each multiresolution level, the gain factor ρ_n in Eq.5.10 was calculated using the same following parameters ($a = 3500$, $A = 51$, $\alpha = 0.602$), it was iterated for 5000 iterations, and in each iteration a different random subset of 5000 image voxels was selected which are members of a Halton sequence for computing the similarity criterion. A number of 3D-3D registrations between the

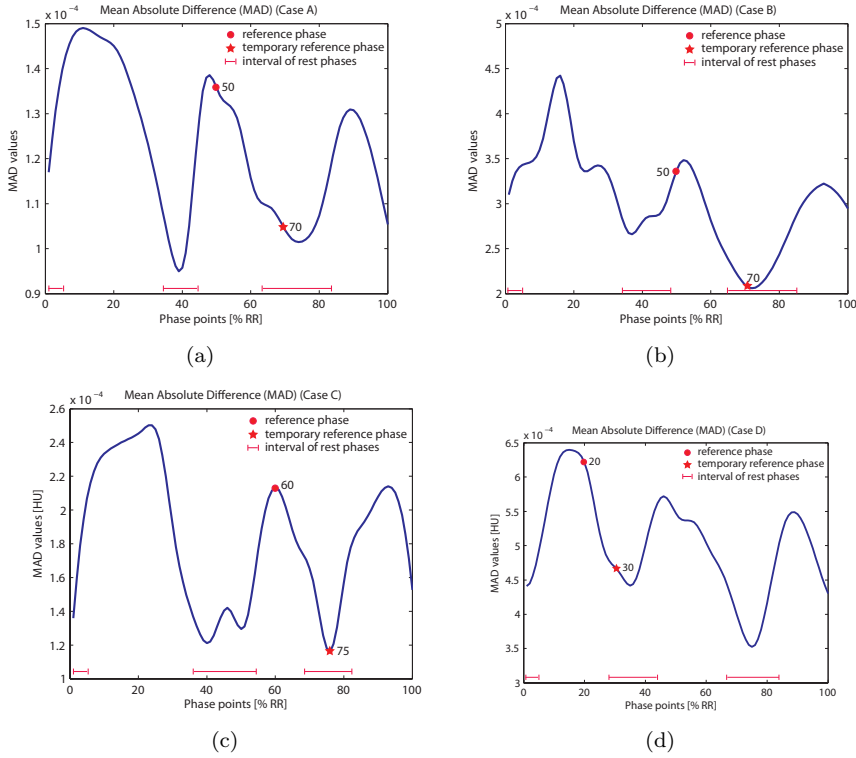


Figure 5.6. The *MM* of the four clinical cases A,B,C and D. The mean absolute differences ((a)-(d)) are presented. For a smoother representation of the MAD curves, a cubic-spline interpolation was used. Moreover, the selected actual (red points) and temporary (red stars) reference phases, and the intervals of quiescent motion phases (red intervals) used for the image registration process are shown.

previous temporary reference phases R^T and all the other selected quiescent phases Q were executed. Each registration took approximately 6 minutes on a 2.8 GHz AMD Opteron. As an example, in Fig.5.7 the registration results achieved for the case B are shown. A cubic-spline interpolation was used to achieve a temporal continuous MVF $\mathbf{m}(\mathbf{x}_i(R^T), R^T, P)$ from the temporary phase R^T and all the other arbitrary phases P in the entire RR interval. Given the $\mathbf{m}(\mathbf{x}_i(R^T), R^T, R)$ a fixed-point-based iterative approach [11] was used to recover the inverse MVF from the actual strong motion to the temporary quiescent reference phase $\mathbf{im}(\mathbf{x}_i(R), R, R^T)$. Here, to determine the $\mathbf{im}(\mathbf{x}_i(R), R, R^T)$ it was iterated for 10 iterations which took approximately 3 minutes. After performing all the remaining steps previously described in section 5.2.4 the final MVFs $\mathbf{m}(\mathbf{x}_i(R), R, P)$ were achieved.

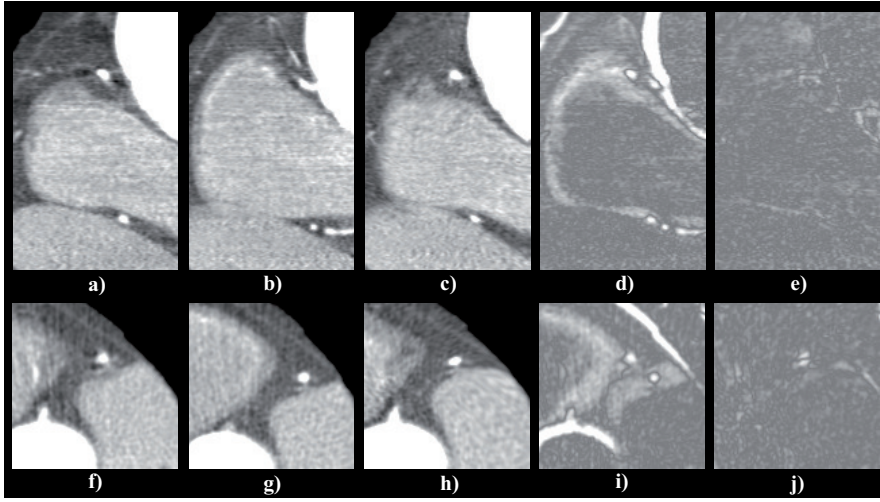


Figure 5.7. Registration results for the case B. In order, at the top, a sagittal view of the volume reconstructed at 70% RR (a), the corresponding view of the volume reconstructed at 40% RR (b), the corresponding view of the volume reconstructed at 40% RR warped to the 70% RR phase (c), and the absolute difference images before (d) and after (e) the registration are shown. At the bottom with the same order the registration results for an axial view are presented. (AWCR method, optimized gating window width, Level=0 HU, Window=500 HU)

5.3.4 Consistency study of the estimated motion vector fields

In clinical applications, due to the absence of ground truth evaluating the accuracy of estimated MVF is a complex issue. In this contribution, the current gold standard AWCR reconstruction [57] with the narrowest gating window width was considered as the best representation of the ground truth. This reconstruction was compared with the MC AWCR reconstruction [136]. Fig.5.8 presents the reconstruction results (top), and the mean absolute difference (MAD) between the AWCR reconstructions with a gating window width of 22% RR and the MC AWCR reconstructed volumes with gating window widths of 22%, 40%, 60% and 80% RR, performed at each phase within the RR interval with step of 10% RR.

A common way to evaluate the consistency of an MVF estimation methodology can be to determine the cumulative MVF over a closed motion sequence, which should ideally be equal to zero. For the method described in this chapter, the EIR was applied only between volumes imaged at cardiac rest phases. Therefore, it makes sense to perform the EIR consistency check, over one of the selected region of quiescent phases within the RR interval. Chosen a starting phase point P , the cumulative MVF of a

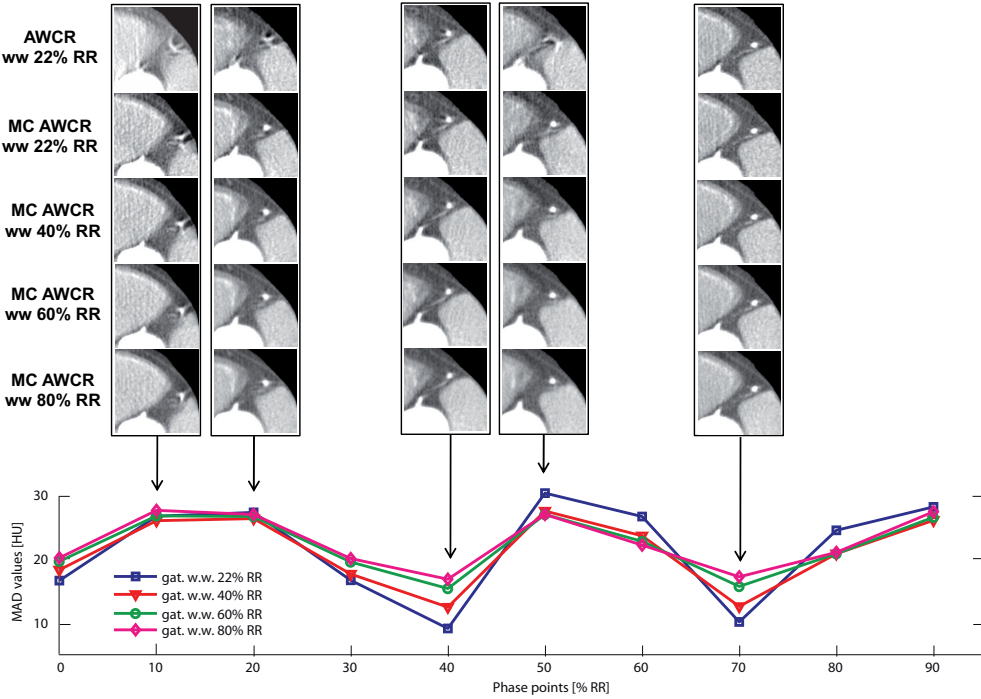


Figure 5.8. MVF consistency study. In order in each column (top) the AWCR reconstructed images with a gating window width of 22% RR (first row), and the MC AWCR reconstructed images with a gating window width of 22, 40, 60, and 80 % RR (second-fifth rows) at five different phase points within the RR interval are shown (case A, cubic grid size = 0.3 mm, Level=0 HU, Window=500 HU). At the bottom, the corresponding MAD curves are presented.

closed sequence $\mathbf{m}(\cdot, P, P)$ can be determined by

$$\mathbf{m}(\cdot, P, P) = \sum_{i=0}^{L-1} \mathbf{m}(\cdot, P + \nu i, P + \nu(i+1)) + \sum_{i=L-1}^0 \mathbf{m}(\cdot, P + \nu(i+1), P + \nu i), \quad (5.14)$$

where $\nu = 1, 2, \dots$ is the step, and $L = 1, 2, \dots$ represents the number of subsequent MVFs considered to build the closed MVF sequence. For the consistency check performed in this chapter, $P=65\%$ RR, $\nu = 5\%$ RR, and $L = 4$ are used for all the clinical cases. In Table 5.3, the mean and the standard deviation (STD) values of the cumulative MVF $\mathbf{m}(\cdot, 65\%RR, 65\%RR)$ x,y, and z components are determined over the all image voxels. Moreover, the percentages of voxels with MVF components within four different inconsistency bins are shown (Table 5.3). From both the re-

Table 5.3. Closed sequence consistency check. The mean and the STD of the MVF $\mathbf{m}(\cdot, 65\%RR, 65\%RR)$'s components values determined over the all image voxels are presented. Moreover, even the percentages of image voxels with MVF's components inconsistency within different inconsistency bins are shown.

Case	$\mathbf{m}(\cdot, 65\%, 65\%)$	Mean[\pm STD]	< 0.3 mm	[0.3-0.6] mm	[0.6-1.2] mm	> 1.2 mm
A	MVF _x	-0.01[\pm 0.27] mm	93.65 %	4.78 %	1.39 %	0.18 %
	MVF _y	-0.02[\pm 0.30] mm	92.13 %	5.60 %	1.88 %	0.39 %
	MVF _z	0.06[\pm 0.33] mm	90.77 %	4.91 %	2.70 %	1.62 %
B	MVF _x	0.08[\pm 0.44] mm	91.51 %	5.40 %	2.50 %	0.59 %
	MVF _y	-0.06[\pm 0.42] mm	93.84 %	3.65 %	1.78 %	0.73 %
	MVF _z	0.09[\pm 0.45] mm	90.26 %	4.45 %	3.41 %	1.88 %
C	MVF _x	-0.10[\pm 0.48] mm	90.51 %	7.85 %	1.49 %	0.15 %
	MVF _y	0.04[\pm 0.44] mm	87.34 %	8.11 %	2.65 %	1.90 %
	MVF _z	0.09[\pm 0.40] mm	86.10 %	8.25 %	3.22 %	2.43 %
D	MVF _x	-0.01[\pm 0.25] mm	97.79 %	1.60 %	0.54 %	0.07 %
	MVF _y	-0.02[\pm 0.33] mm	98.59 %	1.09 %	0.29 %	0.03 %
	MVF _z	-0.01[\pm 0.26] mm	98.59 %	1.07 %	0.33 %	0.01 %

sults presented in Fig. 5.8 and the *MM* shown in Fig. 5.6(a), it can be observed that consistent motions are estimated in the regions of slow cardiac motion ([30,45]% and [65,85]% RR). Indeed, here the MC AWCR reconstruction with the narrowest gating window of 22%RR present a very good quality which is comparable with the quality of AWCR reconstruction (Fig. 5.8, blue curve). Moreover, despite to the increased gating window width, in these phases even the MC AWCR performed with a gating window width of 40%, 60%, and 80% RR still remove the residual motion blurring artifacts (Fig. 5.8, bottom, red, green, and magenta MAD curves). Clearly, at the phases of strong motion the strength of the MC reconstruction can be observed. In the regions between [0,25]%, [50,60]%, and [90,100]% RR excellent MC AWCR reconstructions are achieved. Here, all the MAD curves show higher values due to the strong motion blurring artifacts which are present in the AWCR reconstructed images, but removed in the MC AWCR results. Furthermore, as can be observed in the curves at the bottom in Fig. 5.8, the MAD values never exceed 30 HU in the interval of strong cardiac motion, and 20 HU in the phases of slow cardiac motion. Since very high absorption values are present in regions filled of contrast agent (e.g. the Aorta, the left ventricle

and the RCA and LCA), these very low maximum values of the MAD prove that a very good global overlap was achieved between the volumes reconstructed with the AWCRC and the MC AWCRC methods.

Finally, from both the images and the MAD curves shown in Fig. 5.8 can be observed as MC reconstructions overcome the quality of non-compensated reconstructions in the whole RR interval.

Similar conclusions are achieved for the quantitative consistency check results presented in Table 5.3. In accordance with the qualitative observations discussed above, the presented results show as for the all clinical cases the determined cumulative MVFs $\mathbf{m}(\cdot, 65\%RR, 65\%RR)$'s components have mean values close to zero, and STD values about the voxel size. For the 90% of voxels, a subvoxel precision is achieved for the cumulative MVF components, and in the 95% of them the MVF inconsistency never exceeds two times the voxel size. In conclusion, this final quantitative study confirms as the EIR method can be an efficient solution to carry out a reliable MVF estimation between volumes reconstructed at quiescent phases.

5.3.5 MC iterative coronary ROI reconstructions in patient data

The proposed MC iterative ROI reconstruction was used to reconstruct the coronary arteries of three different clinical cases. A suitable ROI was selected that was large enough to contains the LCA and RCA of the three patients (Table 5.1). The images were reconstructed at the strong cardiac motion reference phases $R= 50\%$, 50% , 60% RR for the case A,B and C, respectively. For all image reconstructions a gating window width of 40% RR was used. Finally, the gated AWSART and the MC gated AWSART reconstructed volumes produced after 10 iterations and the relative 3D volume rendered images, are shown in Fig. 5.9,5.10 and 5.11 for the case A, B, and C, respectively. Here, for reasons of comparison, even the gated AWSART reconstructions at the quiescent phase of 75% RR with a gating window width of 40% RR are presented.

For the clinical case A, an RCA was reconstructed. The gated AWSART reconstruction leads to blurred images (Fig. 5.9(a)-(i) (left)), whereas the MC gated AWSART reconstruction produces significantly better images quality, where the *Aorta*, the RCA's *ostium*, the *interventricular posterior branch*, the whole RCA, and its *right conal* and *marginal acute branches* are clearly visible (Fig. 5.9(a)-(i) (right)). The same improvements are observable in the 3D volumes rendering in Fig. 5.9(j), where for the MC gated AWSART a very long RCA segment is recovered and visible (Fig. 5.9(j) (center)). Due to the residual strong cardiac motion, the gated AWSART image is blurred and an inconsistent ghost RCA is obtained (Fig. 5.9(j) (left)).

An RCA is shown for the clinical case B. Even here, the MC reconstructed images of the RCA (Fig. 5.10(a)-(c) (right)) and the *Aorta* (Fig. 5.10(a)-(b) (right)) look sharper than the corresponding non-compensated gated reconstructions (Fig. 5.10(a)-(c) (left)). The 3D volumes rendering presented in Fig. 5.10(d) confirms as the proposed MC gated AWSART method (center) allows to strongly reduce the motion blurring artifacts which degrade the quality of the standard gated reconstruction (left).

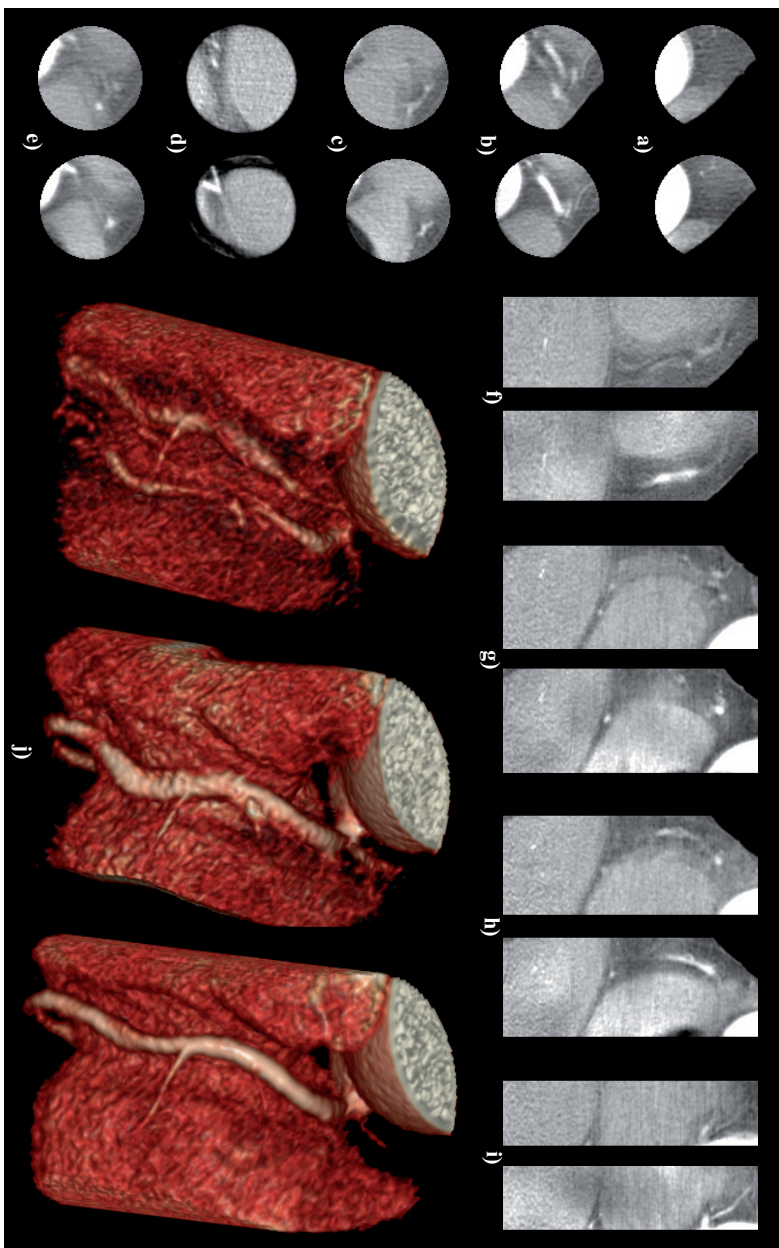


Figure 5.9. The axial (a)-(c), coronal (d)-(f) and sagittal (g)-(i) views and the corresponding 3D volume rendering (j). In order, the gated AWSART (left column) and the MC gated AWSART (right column) reconstructed images at phase point 50% RR with a gating window width of 40% RR are shown. In (j) the corresponding 3D volume rendering are presented (left and center) and a gated AWSART reconstruction at 75% RR with a gating window width of 40% RR is shown (j)(right). (Case A, 10 iterations, ROI's radius=25 mm, Level=0 HU, Window=700 HU).

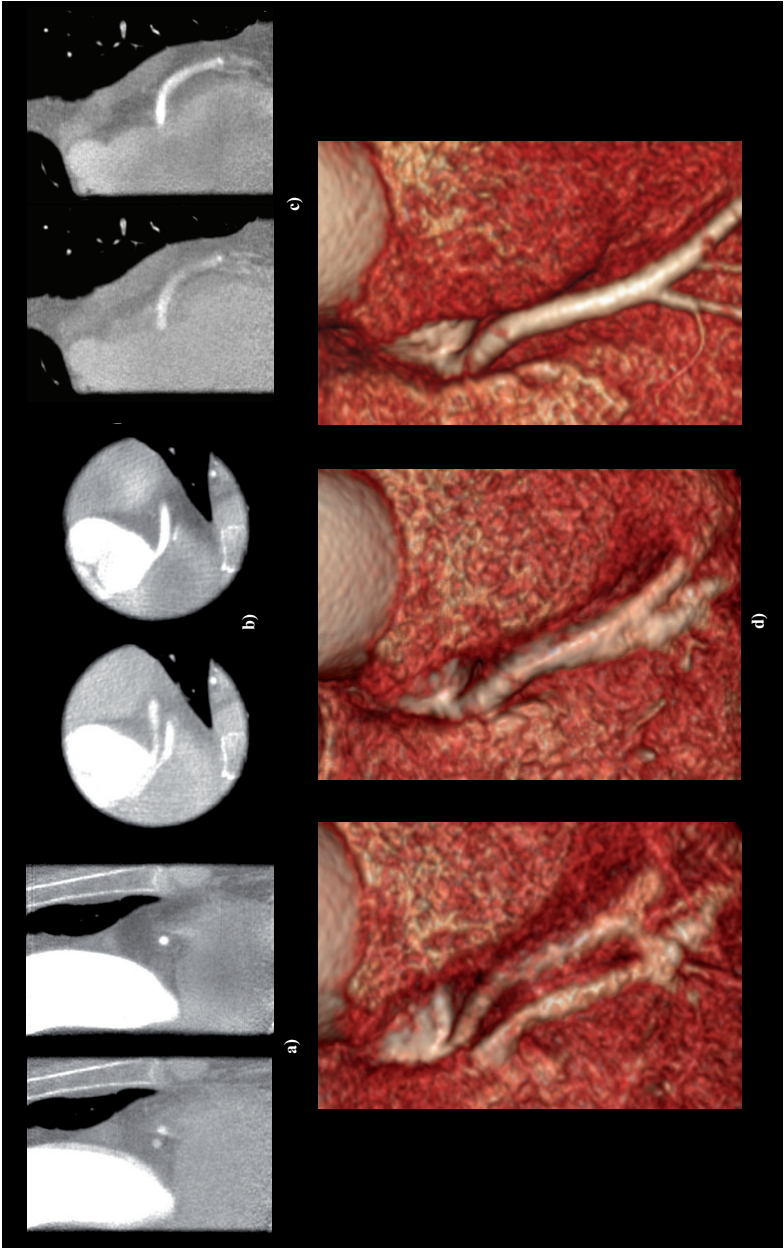


Figure 5.10. The sagittal (a), axial (b) and coronal (c) views and the corresponding 3D volume rendering (d). In order, the gated AWSART (left column) and the MC gated AWSART (right column) reconstructed images at phase point 50% RR with gating window width of 40% RR are shown. In (d) the corresponding 3D volume rendering are presented (left and center) and a gated AWSART reconstruction at 75% RR with a gating window width of 40% RR is shown (d)(right). (Case B, 10 iterations, ROI's radius=33 mm, Level=0 HU, Window=500 HU).

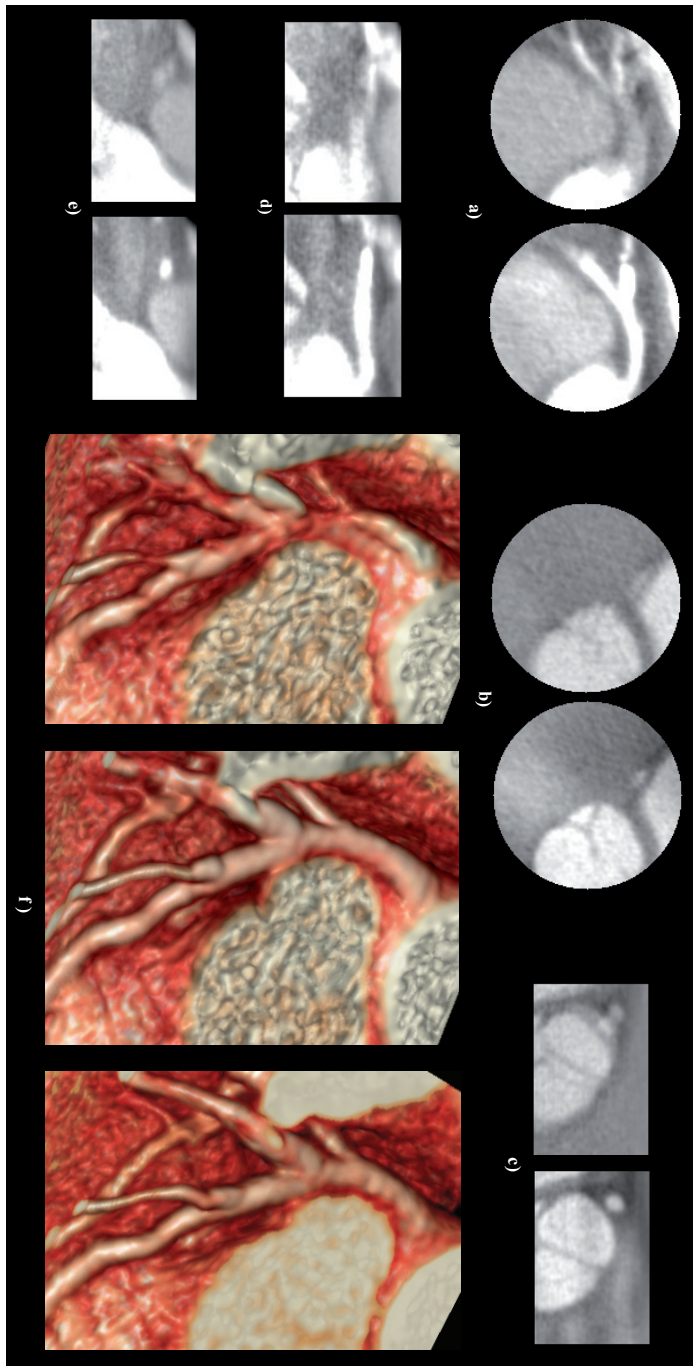


Figure 5.11. The axial (a)-(b), sagittal (c) and coronal (d)-(e) views and the corresponding 3D volume rendering (f). In order, the gated AWSART (left column) and the MC gated AWSART (right column) reconstructed images at phase point 60% RR with a gating window width of 40% RR are shown. In (f) the corresponding 3D volume rendering are presented (left and center) and a gated AWSART reconstruction at 75% RR with a gating window width of 40% RR is shown (f)(right). (Case C, 10 iterations, ROI's radius=29 mm, Level=0 HU, Window=850 HU in (a), (d) and (e), and Level=200 HU, Window=900 HU in (b) and (c)).

Excellent results are achieved even for the LCA's ROI reconstruction of the clinical case C. In Fig. 5.11(a) the *left main* and its two main branches, the *left anterior descending* and the *left circumflex artery* are clearly visible in the MC gated AWSART reconstruction (right), but practically invisible in the gated AWSART image (left). In the MC images in Fig. 5.11(b) (right) the *aortic valve* is very sharp and visible, instead in its counterpart non motion-corrected gated image the same valve is strongly blurred (Fig. 5.11(b) (left)). The same conclusions can be given for the MC results presented in the coronal and sagittal views in Fig. 5.11(c)-(e), where the LCA vessel, and the *aortic valve* are well visible. The 3D volumes rendering in Fig. 5.11(f) (center) show as even in a phase of strong cardiac motion, the MC iterative reconstruction leads to an image where not only the LCA's main branches, but even the secondary vessels as its *first diagonal branch* and its *first marginal branch* are recovered and noticeably visible.

Finally, it is interesting to observe as in all cases presented the MC gated AWSART reconstructions at strong motion phases produce coronary arteries that are consistent with those obtained with a standard gated AWSART method at a quiet phase of 75% RR (Fig. 5.9(j)(right), 5.10(d)(right), 5.11(f)(right)). Despite the impressive results, the ECG-gated reconstructions at phases of slow cardiac motion present an higher image sharpness compared to that achieved using the proposed MC approach at strong motion phases.

5.3.6 Validation on clinical data of the blobs volume-adaptation for MC iterative reconstructions

In this subsection an investigation of the performance of the efficient projection model for blobs in MC iterative cone beam CT reconstruction [39] on clinical data is presented. Due to the characteristic divergent pumping motion of the chambers of the heart, the comparison between the MC gated AWSART reconstructions with and without the proposed blobs-volume scaling, is shown for the LV reconstruction of the clinical case D.

The gated AWSART and MC gated iterative reconstructions with (MC gated AWSART) and without (MC gated AWSART_{nvs}) the proposed blob volume scaling are performed by using the settings listed in Table 5.1. In Fig.5.12 the relative reconstructed images are shown. Furthermore, in Fig.5.13 the absorption profiles along the red and green lines in the images in Fig.5.12(b) and Fig.5.12(c) are presented.

In Fig. 5.12(a) (left) the gated AWSART reconstructed images are strongly affected by the motion blurring artifact. This makes impossible to perform a preventive analysis of the cardiac condition of the LV, the *ventricular myocardium*, the *left atrium*, the *ascending Aorta*, and the *aortic* and *mitral valves*. In Fig. 5.12(a) (middle) the MC gated AWSART reconstructed images performed using the estimated MVFs and the proposed volume-dependent blob-footprint adaptation look sharper and the motion blurring artifact is strongly reduced. The same enhancement is clearly visible in Fig. 5.12(b)-(c) (middle). Here, the *pulmonary artery*, the *ascending Aorta* and the *aortic valve* are well defined. Moreover, even a section of the LCA vessel which was strongly blurred and almost invisible in the non-compensated iterative reconstruction, in the MC images it looks sharper and well visible. For reasons of

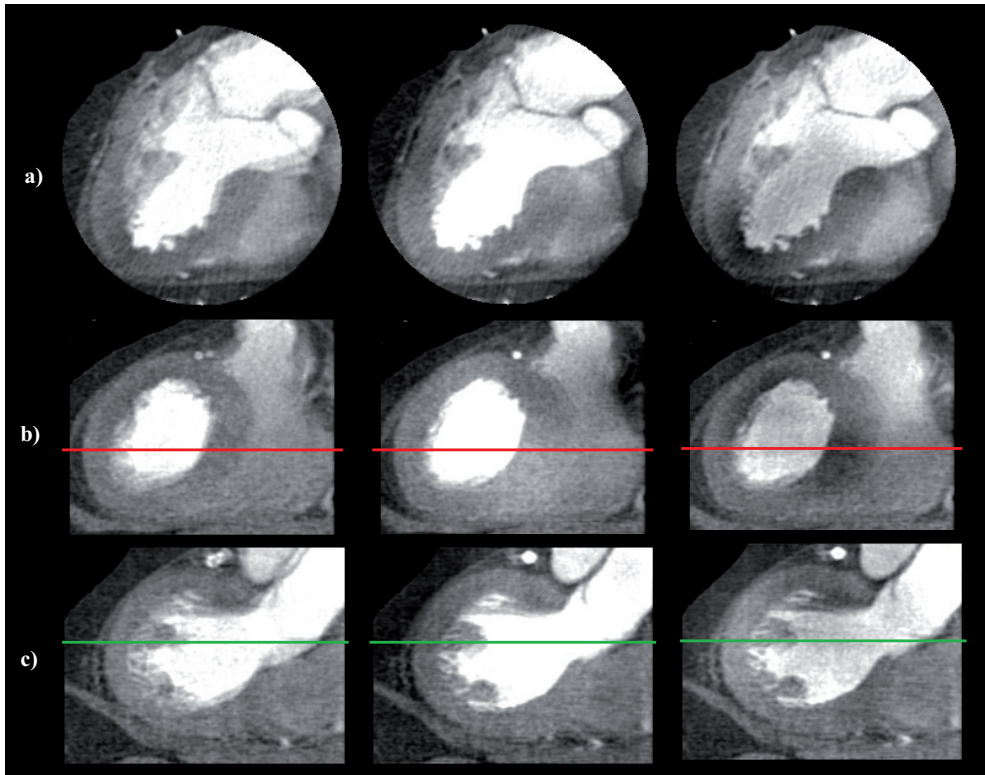


Figure 5.12. Axial (a) and coronal (b)-(c) views of the gated AWSART (left column), the MC gated AWSART (middle column), and the MC gated AWSART_{nvs} (right column) reconstructed images are shown. (Case D, at phase point 20% RR, gating window width of 40 % RR, 10 iterations, ROI's radius=37 mm, Level=150 HU, Window=650 HU).

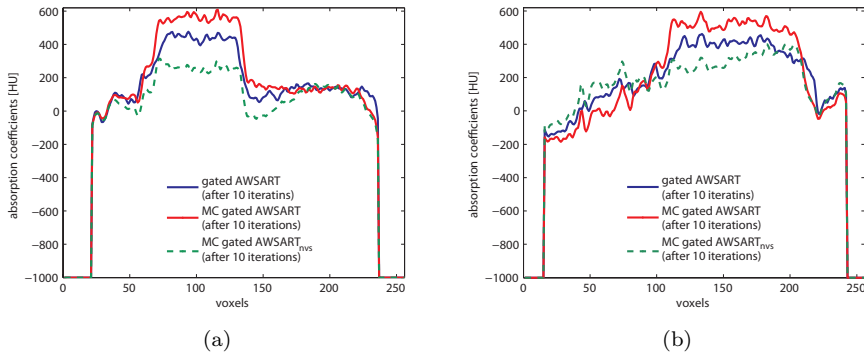


Figure 5.13. Absorption coefficients of the gated AWSART, the MC gated AWSART, and the MC gated AWSART_{nvs} image reconstructions performed for clinical case D, respectively, along the red lines indicated in Fig. 5.12(b), and along the green lines indicated in figure Fig. 5.12(c).

comparison, in the right column in Fig. 5.12(a)-(c), even the MC gated AWSART_{nvs} reconstruction images performed using the same estimated MVFs are shown. Even in this case the motion artifacts are reduced, but the quality of the images is clearly degraded. Here, due to the divergent pumping motion of the LV chamber, the blobs are locally moved in different directions and an irregular reconstruction grid is produced. If any volume-dependent blobs-footprint adaptation is performed, several gaps are generated among the blobs of the irregular grid. These yield a non-homogeneous image representation and degrade tremendously the quality of the reconstructed images. In different areas of the LV, of the *myocardium*, and of the ascending Aorta, a strong reduction of the absorption coefficients produces several dark stains that can induce to an erroneous or practically impossible diagnosis of the LV (Fig. 5.12(a)-(c) (right)). The proposed volume-dependent blob footprint adaptation shows to avoid this strong reduction of the absorption coefficients, by taking into account the variation of the blobs volume caused from the divergent MVF of the LV. This is confirmed even from the absorption coefficient profiles shown in Fig. 5.13(a)-(b). Here, for the MC gated AWSART_{nvs}, even if it is completely filled of contrast agent, the absorption coefficients inside the LV are so reduced that they become comparable with the absorption coefficients of the *myocardium*. Instead, with the MC gated AWSART and the proposed blob-volume adaptation an higher contrast between the LV and the *myocardium* absorption coefficients is recovered.

5.4 Discussion

In this chapter, the use of a fast elastic image registration method for fully automatic local cardiac motion compensated gated iterative coronary artery reconstruction was presented and evaluated. The evaluation included a validation on a dynamic cardiac phantom, an MVF consistency check, a qualitative inspection of reconstructed image

quality, and a clinical validation of the method proposed in [39] for volume-dependent adaptation of the footprint of the blobs in case of MC iterative reconstructions.

The ECG-gated CT reconstructed images are strongly affected by the chosen phase of reconstruction. In this work, subvolumes of the heart of different patients have been reconstructed in fast cardiac motion phases. Here, the ECG-gated iterative reconstructions, even if the smallest possible gating window width is used, fail to generate motion artifact-free images. This hampers the interpretation of coronary segments which could contain suspicious structures.

From the MC gated iterative reconstruction results presented in Fig. 5.5, 5.9, 5.10, 5.11, and 5.12, it is noticeable that adding a reliable object motion model inside the iterative reconstruction framework can lead to excellent reconstructed images with reduced motion blurring. After the clinical validation study, the efficient projection model proposed in [39] reduced the strong artifacts caused by the change of the blobs volume, when a divergent MVF is applied for MC iterative reconstructions.

Compared with local improvements obtainable with other landmarks- or coronary centerlines-MVF estimation methodologies [5, 43, 95], here the improvement of the MC reconstruction is visible uniformly inside the ROI. Future research should be focused on the application of the proposed method on whole heart MC iterative reconstruction. Here, further investigations are required to verify if accurate cardiac MVFs can be achieved.

The calculation of the temporal resolution of an MC reconstruction with the proposed motion model is not straightforward and no recipe to calculate temporal resolution known from the literature includes motion compensation. The interval of possible values for the temporal resolution varies from the time required to measure a single projection at the selected phase point (ideal MC reconstruction) to the temporal resolution of a data set reconstructed with an ECG-gated reconstruction method using all projections inside the gating window. Apparently the temporal resolution is improved when using an MC reconstruction method, but the exact quantification remains an open area of research.

Despite the promising results, some method limitations are not negligible. First, since the image registration estimates the unknown cardiac MVF at the quiescent motion phases, future work should address the challenge to estimate the MVF even at fast motion phases. It is important to stress that a non-equidistant phase sampling is to the cost of interpolation errors between phases where rapid cardiac motions take place. A linear or cubic-spline temporal interpolation of the MVF might not capture the real motion of the heart. Registering the images reconstructed at fast motion phases could provide important spatial information of the heart at these phases. A possible solution to use the cardiac strong motion phases during the registration step, could be to add a temporal smoothing term to the combined criterion in Eq. 5.5 in order to produce a smoothed version of the motion trajectory of each image voxel. In this case, care should be taken in order to properly tune the corresponding regularization parameter, since a strong temporal regularization could lead to non-optimal solutions with poor images spatial alignment. An alternative approach is surface-model-based segmentation [96, 138] together with image registration in order to extrapolate the cardiac MVF.

Second, one requirement to this approach is having accurate initial reconstruc-

tions to be aligned. The frequent presence of image artifacts can affect the real MVF which describes the heart motion. A 2D-3D non-rigid registration [99] can be a potential solution for a more accurate cardiac motion estimation. Here, the 3D MVF is determined by aligning only one initially ECG-gated reconstructed volume to a series of ECG-gated projections.

Third, the proposed MC iterative method consists of two passes. Initially, the cardiac MVF is estimated by image registration, subsequently, this motion information is used to perform an MC iterative reconstruction. To increase the method's speed and accuracy, single-pass methodologies may permit the determination of the MVF during the reconstruction process [114].

5.5 Conclusions

In conclusion, a fully automatic local cardiac motion compensated gated iterative method with volume-adapted blobs as basis functions is proposed. The method leads to excellent MC gated iterative reconstructed images which outperform the quality of the images reconstructed with a classical gated iterative method. In clinical cases, a volume-dependent blobs-footprint adaptation proves to be a good solution to take care of the change of the blobs volume caused by a divergent MVF. Though the image quality of reconstructions at cardiac phases of fast motion is increased significantly, a gated reconstruction in the cardiac resting phase remains superior in image quality at moderate heart rate.

Summary

If people do not believe that mathematics is simple, it is only because they do not realize how complicated life is.

— JOHN LOUIS VON NEUMANN (1903 – 1957)

Iterative CT reconstruction techniques are an excellent alternative to classical FBP reconstruction methods. In particular, statistical iterative methods have shown to produce reconstructed images with a higher SNR compared to that achieved with analytical methods. A drawback of iterative reconstruction is its high computational cost. However, in case of a cardiac subvolume reconstruction, e.g. a coronary vessel segment or the left ventricle, iterative ROI reconstruction represents an excellent solution to reduce the computational effort.

As a consequence of cardiac motion, CT image quality of ECG-gated and -triggered reconstructions strongly depends on the cardiac phase. The larger the gating window the better the SNR of the image, because more projections contribute to the reconstruction results. However, a wider gating window produces more motion artifacts. Also, at certain cardiac phases of rapid motion, cardiac CT reconstruction quality is seriously compromised.

Cardiac-motion compensated CT reconstruction methods have shown to be a potential tool to correct the artifacts caused by object-motion during CT acquisition. Hereto, an efficient local motion estimation methodology has to be developed in order to extract the unknown motion information related to the chosen cardiac ROI. Furthermore, divergence in motion vector fields as occurring for the ventricular pumping motion should be taken into account during MC reconstruction. If this effect would be neglected, this would lead to strong streak artifacts or dark stains which could hamper the visualization of the coronary vessels and the heart chambers.

The objective of this thesis was to derive new techniques in the field of diagnostic cardiac imaging to overcome these problems. In the first part, a new MC iterative algorithm was proposed which takes both the motion vector field and its divergence during line integral calculation into account (Chapter 2). Since an MC reconstruction requires as input an MVF of the moving object, three methods for motion estimation are proposed: a manual, semi-automatic and fully-automatic motion estimation methodology, respectively (Chapters 3-5). For all of these methods an initial 4D multiphase ECG-gated image data set is required.

In the following the results of the chapters are discussed in more detail:

Chapter 2: In this chapter a new 3D method to reconstruct moving objects from cone-beam X-ray projections using an iterative reconstruction algorithm and a given motion vector field was presented and evaluated on phantom data. A comparison with a non-motion compensated iterative method and a classical FBP reconstruction approach was given. Results for two simulated data sets subject to three different motion patterns were shown. The motion compensation framework combined with an efficient method to calculate the line integral through volume-adapted blobs prevented motion and streak artifacts in the reconstructed images and ensured robustness against noise.

Chapter 3: In this chapter a novel 3D method for motion compensated iterative CT reconstruction of a cardiac region of interest was presented. A statistical maximum likelihood ECG-gated iterative technique was applied as basic reconstruction method. A limited number of manually indicated anatomical point landmarks of the coronary segment of interest were used as an input of a thin-plate spline warping in order to estimate the unknown MVF of the cardiac ROI. An inspection of the manual localization error revealed that an error up to 7.5 mm can be tolerated, and that bigger landmark localization errors lead to blurred reconstructed images of the coronary vessel. Results on two clinical data sets at strongest motion phases were compared with standard gated iterative reconstruction showing that motion compensation strongly improved reconstruction quality. MC statistical iterative reconstructed images presented an higher SNR compared to that achieved with an MC FBP method. Despite its simplicity and efficiency, the proposed method requires the input of an experienced observer for landmark localization. This is a limitation, owing to the workload, and the introduced inter-observer variability.

Chapter 4: In this chapter a method which combines motion-compensated iterative computed tomography reconstruction and minimum cost path-based coronary centerline extraction technique to obtain motion artifact-free reconstructed images of the coronary arteries was proposed and evaluated. To reduce the human interaction during the motion estimation, the method required a pair of starting-ending coronary vessel points provided by the user in a single time-frame only. Subsequently, a set of coronary centerlines extracted at multiple cardiac phases within the RR interval were used to determine the unknown MVF. The performance of the method was validated on three patients, showing the improved sharpness of cardiac motion-corrected gated iterative reconstructions compared to the results achieved by a classical gated iterative method. The results were also compared to the manual coronary artery motion estimation method introduced in chapter 3 showing improved image quality. Since the MVF was determined from the extracted multiphase coronary centerline, the proposed method yielded only local improvements in the regions surroundings the coronary artery.

Chapter 5: In this chapter a novel method for motion-corrected iterative CT reconstruction of a cardiac region of interest was proposed. Given a precomputed (non-motion compensated) ECG-gated 4D ROI image data set, a fast and fully automatic elastic image registration was applied to determine a dense cardiac MVF from a chosen cardiac reference phase to a number of phases within the RR interval. Experiments on phantom and patient data sets showed that in terms of image quality

MC iterative reconstructions outperformed standard gated iterative reconstructions at phases of fast cardiac motion. Furthermore, a qualitative and quantitative accuracy analysis of the estimated cardiac motion field showed that for 90% of the voxels a subvoxel precision was achieved for the cumulative MVF components, and for 95% of them the MVF inconsistency never exceeded two times the voxel size. Finally, for the first time a blob-volume adaptation was applied on clinical data. In the case of divergence in the LV motion field, it yielded improved image quality. Though the image quality of MC reconstructions at cardiac phases of fast motion was increased significantly, ECG-gated reconstruction in the cardiac resting phase remained superior in image quality at moderate heart rate.

The reconstruction techniques proposed in this thesis can be applied in cases where the current ECG-gated or -triggered coronary CT reconstructions at rest phases are strongly degraded by motion artifacts. An MC approach can reduce the residual motion artifacts present in the coronary reconstructed images, and since wider gating window can be applied, also image SNR can be increased. Another potential application is in the field of cardiac functional CT imaging. Here, images of cardiac valves and chambers are needed within the whole RR interval. ECG-gated reconstructions yield excellent images at quiescent motion phases, but fail to produce good images in the phases of strong motion (e.g. at systole). The proposed MC iterative reconstruction and motion estimation methodologies can be applied to yield sharp images even at these phases of fast heart motion.

The proposed MC reconstruction methods have also potential in other anatomies.

The thoracic aorta is known to cause many diagnostic difficulties and pitfalls in CT imaging, especially in patients with suspected aortic dissection [80]. When streak artifacts and aortic wall motion may simulate or alter aortic dissection, MC reconstruction can be applied to reduce these artifacts and to allow improved diagnosis and treatment planning of the disease.

Detectability of lung tumors in CT images is severely compromised by respiratory motion. A method like the one proposed in chapter 5 can be applied to perform MC reconstruction of the lung. Hereto, a 4D data set consisting of volumes reconstructed at different breathing motion phases should be elastically registered to determine the unknown lung motion.

The work presented in this thesis still has a number of limitations. First, improved image quality has been shown on a limited number of cases only. A further extensive clinical validation of the proposed approaches is still required. In such a study, also parameter settings should be optimized to increase accuracy and robustness of the method. Second, the proposed MC iterative methods consist of two passes. Initially, the unknown cardiac MVF is determined by applying suitable motion estimation techniques, subsequently, this motion information is used to perform an MC iterative reconstruction. To increase the methods's speed and accuracy, single-pass methodologies should be investigated which may permit the determination of the MVF during the reconstruction process [114].

In conclusion, a method for motion compensated iterative reconstruction for cardiac CT has been proposed. A significant improvement in image quality can be achieved at phases of significant cardiac motion. The method therefore has potential

for evaluating segments which contain suspicious structures and in which standard ECG-gated MSCT reconstruction results yield limited image quality. In coronary segments with hardly visible soft plaques, the parallel SNR improvement and motion artifact reduction can be used to reduce ambiguous diagnosis without performing a second examination.

Bibliography

One's work may be finished someday, but one's education, never.

— ALEXANDRE DUMAS, PÈRE (1802 – 1870)

- [1] S. Achenbach, W. Moshage, K. Bachmann, “Noninvasive coronary angiography by contrast-enhanced electron beam computed tomography”, *Clin. Cardiol.*, vol. 21, no. 5, pp. 323 – 330, 1998.
- [2] S. Achenbach, D. Ropers, J. Holle, G. Muschiol, W. G. Daniel, W. Moshage, “In-Plane Coronary Arterial Motion Velocity: Measurement with Electron-Beam CT”, *Radiology*, vol. 216, no. 2, pp. 457 – 463, 2000.
- [3] A. S. Agaston, W. R. Janowitz, F. J. Hildner, N. R. Zusmer, M. Jr. Viamonte, R. Detrano, “Quantification of coronary artery calcium using ultrafast computed tomography”, *J. Am. Coll. Cardiol.*, vol. 15, no. 4, pp. 827 – 832, 1990.
- [4] A. Andersen & A. Kak, “Simultaneous Algebraic Reconstruction Technique (SART): A superior implementation of the ART algorithm”, *Ultrason. Imag.*, vol. 6, pp. 81 – 94, 1984.
- [5] C. Blondel, R. Vaillant, G. Malandain, N. Ayache, “3-D tomographic reconstruction of coronary arteries using a precomputed 4D motion field”, *Phys. Med. Biol.*, vol. 49, pp. 2197 – 2208, 2004.
- [6] F. Bookstein, “Thin-Plate Splines and the decomposition of deformations”, *IEEE Trans. Pattern Anal. Machine Intell.*, vol. 11, no. 6, pp. 567 – 585, 1989.
- [7] D. P. Boyd & M. J. Lipton, “Cardiac computed-tomography”, *Proc. IEEE*, vol. 71, pp. 298 – 307, 1983.
- [8] R. N. Bracewell (ed.), *The Fourier Transform and Its Applications*, 2nd ed. ed., McGraw-Hill, New York, 1978.
- [9] K. M. Brown, D. J. Heuscher, P. Kling, “Conebeam computed tomography imaging”, 2002, US Patent 6775346.
- [10] F. Cademartiri, L. L. Grutta, A. Palumbo, P. Malagutti, F. Pugliese, W.B. Meijboom, T. Baks, N. R., Mollet, N. Bruining, R. Hamers, P. J. de Feyter, “Non-invasive visualization of coronary atherosclerosis: state-of-art”, *J. Cardiovasc. Med.*, vol. 8, no. 3, pp. 129–137, 2007.
- [11] M. Chen, W. Lu, Q. Chen, K. J. Ruchala, G. H. Olivera, “A simple fixed-point approach to invert a deformation field”, *Med. Phys.*, vol. 35, no. 1, pp. 81 – 88, 2008.
- [12] S. Y. Chun & J. A. Fessler, “A Simple Regularizer for B-spline Nonrigid Image Registration That Encourages Local Invertibility”, pp. 159 – 169, 2009.
- [13] A. M. Cormack, “Representation of a function by its line integrals, with some radiological applications”, *J. Appl. Phys.*, vol. 34, pp. 2722 – 2727, 1963.
- [14] W. R. Crum, T. Hartkens, D. L. G. Hill, “Non-rigid image registration: theory and practice”, *Brit. J. Radiol.*, vol. 77, pp. S140 – S153, 2004.

- [15] M.E. Daube-Witherspoon, S. Matej, J.S. Karp, R.M. Lewitt, "Application of the row action maximum likelihood algorithm with spherical basis functions to clinical PET imaging", *IEEE Trans. Nucl. Sci.*, vol. 48, no. 1, pp. 24–30, 2001.
- [16] B. De-Man & S. Basu, "A study of noise and spatial resolution for 2D and 3D filtered back-projection reconstruction", in *Nuclear Science Symposium Conference Record*, vol. 6, IEEE, pp. 3937–3939, 2004.
- [17] A. R. DePierro & M. E. B. Yamagishi, "Fast EM-Like Method for Maximum A Posteriori Estimates in Emission Tomography", *IEEE Trans. Med. Imaging*, vol. 20, no. 4, pp. 280–288, 2001.
- [18] EW Dijkstra, "A note on two problems in connexion with graphs", *Numerische Mathematik*, vol. 1, no. 1, pp. 269–271, 1959.
- [19] J. P. Earls, "Questions in cardiovascular CT: how to use a prospective gated technique for cardiac CT", *J. Cardiovasc. Comput. Tomogr.*, vol. 3, no. 1, pp. 45–51, 2008.
- [20] J. P. Earls, E. L. Berman, B. A. Urban, C. A. Curry, J. L. Lane, R. S. Jennings, C. C. McCulloch, J. Hsieh, J. H. Londt, "Prospectively Gated Transverse Coronary CT Angiography versus Retrospectively Gated Helical Technique: Improved Image Quality and Reduced Radiation Dose", *Radiology*, vol. 246, pp. 742–753, 2008.
- [21] E. P. Efstathiopoulos, N. L. Kelekis, I. Pantos, E. Brountzos, S. Argentos, J. Grebáč, D. Ziaka, D. G. Katritsis, I. Seimenis, "Reduction of the estimated radiation dose and associated patient risk with prospective ECG-gated 256-slice CT coronary angiography", *Phys. Med. Biol.*, vol. 54, pp. 5209–5222, 2009.
- [22] L. A. Feldkamp, L. C. Davis, J. W. Kress, "Practical Cone-Beam Algorithm", *J. Opt. Soc. Am. A*, vol. 6, pp. 612–619, 1984.
- [23] T. G. Flohr, U. J. Schoepf, B. M. Ohnesorge, "Chasing the heart-New developments for cardiac CT", *J. Thorac. Imaging*, vol. 22, no. 1, pp. 4–16, 2007.
- [24] A. F. Frangi, W. J. Niessen, K. L. Vincken, M. A. Viergever, "Multiscale Vessel Enhancement Filtering", in *Medical Image Computing and Computer-Assisted Intervention*, vol. 1496 of *Lecture Notes in Computer Science*, pp. 130–137, 1998.
- [25] R. Gordon, R. Bender, G. T. Herman, "Algebraic Reconstruction Techniques (ART) for Three-dimensional Electron Microscopy and X-ray Photography", *J. Theor. Biol.*, vol. 29, pp. 471–481, 1970.
- [26] M. Grass, R. Manzke, T. Nielsen, P. Koken, R. Proksa, M. Natanzon, G. Shechter, "Helical cardiac cone beam reconstruction using retrospective ECG gating", *Phys. Med. Biol.*, vol. 48, pp. 3069–3084, 2003.
- [27] J. H. Halton, "On the Efficiency of Certain Quasi-Random Sequences of Points in Evaluating Multi-Dimensional Integrals", *Numer. Math.*, vol. 2, pp. 84–90, 1960.
- [28] G. T. Herman & L. B. Meyer, "Algebraic reconstruction technique can be made computationally efficient", *IEEE Trans. Med. Imaging*, vol. 12, no. 3, pp. 600–609, 1993.
- [29] N. Hirai, J. Horiguchi, C. Fujioka, M. Kiguchi, H. Yamamoto, N. Matsuura, T. Kitagawa, H. Teragawa, N. Kohno, K. Ito, "Prospective versus Retrospective ECG-gated 64-Detector Coronary CT Angiography: Assessment of Image Quality, Stenosis, and Radiation Dose", *Radiology*, vol. 248, pp. 424–430, 2008.
- [30] M. Hoffmann, J. Lessick, R. Manzke, F. Schmid, E. Gershin, D. Boll, S. Rispler, A. Aschoff, M. Grass, "Automatic determination of minimal cardiac motion phases for computed tomography imaging: initial experience.", *Eur. Radiol.*, vol. 16, no. 2, pp. 365–373, 2006.
- [31] M. H. Hoffmann, H. Shi, B. L. Schmitz, F. T. Schmid, M. Lieberknecht, R. Schulze, B. Ludwig, U. Kroschel, N. Jahnke, W. Haerer, H. J. Brambs, A. Aschoff, "Noninvasive coronary angiography with multislice computed tomography", *J. of Am. Med. Association*, vol. 293, no. 20, pp. 2471–2478, 2005.
- [32] M. B. M. Hofman, S. A. Wickline, C. H. Lorenz, "Quantification of in-plane motion of the coronary arteries during the cardiac cycle: implications for acquisition", *J. Magn. Reson. Imag.*, vol. 8, no. 3, pp. 568–576, 1998.

- [33] M. Holden, "A review of geometric transformations for nonrigid body registration", *IEEE Trans. Med. Imaging*, vol. 27, pp. 111 – 128, 2008.
- [34] G. N. Hounsfield, "Computerized transverse axial scanning (tomography). 1. Description of system.", *Br. J. Radiol.*, vol. 46, no. 552, pp. 1016 – 1022, 1973.
- [35] J. Hsieh, *Computed Tomography - Principles, Design, Artifacts, and Recent Advances.*, SPIE, Bellingham, Washington, 2003.
- [36] J. Hsieh, J. Londt, M. Vass, J. Li, X. Tang, D. Okerlund, "Step-and-shoot data acquisition and reconstruction for cardiac x-ray computed tomography", *Med. Phys.*, vol. 33, no. 11, pp. 4236 – 4248, 2006.
- [37] J. Hsieh, J.-B. Thibault, C. A. Bouman, K. Sauer, "Iterative Method for Region-Of-Interest Reconstruction", 2004, US Patent 6,768,782.
- [38] H. Hu, T. Pan, Y. Shen, "Multi-Slice Helical CT: image temporal resolution", *IEEE Trans. Med. Imaging*, vol. 19, no. 5, pp. 384 – 390, 2000.
- [39] A. A. Isola, A. Ziegler, T. Koehler, W. J. Niessen, M. Grass, "Motion-compensated iterative cone-beam CT image reconstruction with adapted blobs as basis functions", *Phys. Med. Biol.*, vol. 53, no. 23, pp. 6777 – 6797, 2008.
- [40] A. A. Isola, A. Ziegler, D. Schäfer, T. Köhler, W. J. Niessen, M. Grass, "Motion compensated iterative reconstruction of a region of interest in cardiac cone-beam CT", *Comput. Med. Imaging Graph.*, vol. 34, no. 2, pp. 149 – 159, 2010.
- [41] Jr. J. Dennis & R. Schnabel, *Numerical Methods for Unconstrained Optimisation and Non-linear Equations*, SIAM J. Math. Anal., 1997.
- [42] U. Jandt, D. Schäfer, M. Grass, V. Rasche, "Automatic generation of 3D coronary artery centerlines using rotational X-ray angiography", *Med. Image Anal.*, vol. 13, no. 6, pp. 846 – 858, 2009.
- [43] U. Jandt, D. Schäfer, M. Grass, V. Rasche, "Automatic generation of time resolved motion vector fields of coronary arteries and 4D surface extraction using rotational x-ray angiography", *Phys. Med. Biol.*, vol. 54, pp. 47 – 66, 2009.
- [44] M. Kachelriess & W. A. Kalender, "Electrocardiogram correlated image reconstruction from subsecond multi-slice spiral computed tomography scans of the heart", *Med. Phys.*, vol. 25, no. 12, pp. 2417 – 2431, 1998.
- [45] M. Kachelriess, M. Knaup, W. A. Kalender, "Extended parallel backprojection for standard three-dimensional and phase-correlated four-dimensional axial and spiral cone-beam CT with arbitrary pitch, arbitrary cone-angle, and 100% dose usage", *Med. Phys.*, vol. 31, no. 6, pp. 1623 – 1641, 2004.
- [46] M. Kachelrieß, S. Ulzheimer, W. A. Kalender, "ECG-Correlated image reconstruction from subsecond multi-slice spiral computed tomography scans of the heart", *Med. Phys.*, vol. 27, no. 8, pp. 1881 – 1902, 2000.
- [47] M. Kachelriess, S. Ulzheimer, W. A. Kalender, "ECG-correlated image reconstruction from subsecond multi-slice spiral CT scans of the heart", *Med. Phys.*, vol. 27, no. 8, pp. 1881 – 1902, 2000.
- [48] M. Kachelrieß, S. Ulzheimer, W. A. Kalender, "ECG-Correlated Imaging of the Heart with Subsecond Multislice Spiral CT", *IEEE Trans. Med. Imaging*, vol. 19, no. 9, pp. 888 – 901, 2000.
- [49] W. A. Kalender, W. Seissler, E. Klotz, P. Vock, "Spiral volumetric CT with single-breath-hold technique, continuous transport and continuous scanner rotation", *Radiology*, vol. 176, pp. 181 – 183, 1990.
- [50] C. Kamphuis & F. Beekman, "Accelerated Iterative Transmission CT Reconstruction Using an Ordered Subsets Convex Algorithm", *IEEE Trans. Med. Imaging*, vol. 17, no. 6, pp. 1101 – 1105, 1998.
- [51] A. Katsevich, "Theoretically exact FBP-type inversion algorithm for spiral CT", in *Proc. 6th Int. Conf. on Fully 3D Reconstruction in Radiology and Nuclear Medicine*, Asilomar, USA, pp. 3 – 6, 2001.

- [52] J. Kiefer & J. Wolfowitz, "Stochastic estimation of the maximum of a regression function", *Annals of Mathematical Statistics*, vol. 23, no. 3, pp. 462 – 466, 1952.
- [53] J. Kim, *Intensity based image registration using robust similarity measure and constrained optimization: application for radiation therapy*, Ph.D. thesis, the University of Michigan, 2004.
- [54] S. Klein, J. P. W. Pluim, M. Staring, M. A. Viergever, "Adaptive stochastic gradient descent optimisation for image registration", *International Journal of Computer Vision*, vol. 81, no. 3, pp. 227 – 239, 2009.
- [55] S. Klein, M. Staring, J.P.W. Pluim, "Evaluation of optimization methods for nonrigid medical image registration using mutual information and B-splines", *IEEE Trans. Im. Proc.*, vol. 16, no. 12, pp. 2879 – 2890, 2007.
- [56] T. Köhler, R. Proksa, T. Nielsen, "SNR-weighted ART Applied to Transmission Tomography", in *Nuclear Science Symposium Conference Record*, IEEE, pp. 2739 – 2742, 2003.
- [57] P. Koken & M. Grass, "Aperture weighted cardiac reconstruction for cone-beam CT", *Phys. Med. Biol.*, vol. 51, pp. 3433 – 3448, 2006.
- [58] H. Kudo, F. Noo, M. Defrise, "Cone-beam Filtered-Backprojection Algorithm for Truncated Helical Data", *Phys. Med. Biol.*, vol. 43, pp. 2885 – 2909, 1998.
- [59] J. Kybic & M. Unser, "Fast parametric elastic image registration", *IEEE Trans. Im. Proc.*, vol. 12, no. 11, pp. 1427 – 1442, 2003.
- [60] K. Lange & J. A. Fessler, "Globally Convergent Algorithms for Maximum *a Posteriori* Transmission Tomography", *IEEE Trans. Im. Proc.*, vol. 4, no. 10, pp. 1430 – 1450, 1995.
- [61] A. C. Lardo, M. A.S. Cordeiro, C. Silva, L. C. Amado, R. T. George, A. P. Saliaris, K. H. Schuleri, V. R. Fernandes, M. Zviman, S. Nazarian, H. R. Halperin, K. C. Wu, J. M. Hare, J. A. C. Lima, "Contrast-Enhanced Multidetector Computed Tomography Viability Imaging After Myocardial Infarction: Characterization of Myocyte Death, Microvascular Obstruction, and Chronic Scar", *Circulation*, vol. 113, pp. 394 – 404, 2006.
- [62] G. Lauritsch, J. Boese, L. Wigström, H. Kemeth, R. Fahrig, "Towards Cardiac C-arm Computed Tomography", *IEEE Trans. Med. Imaging*, vol. 25, no. 7, pp. 922 – 934, 2006.
- [63] L. P. Lawler, H. K. Pannu, E. K. Fishman, "MDCT evaluation of the coronary arteries, 2004: how we do it-data acquisition, postprocessing, display, and interpretation", *Am. J. Roentgenol.*, vol. 184, pp. 1402 – 1412, 2005.
- [64] A. W. Leber, A. Becker, A. Knez, F. von Ziegler, M. Sirol, K. Nikolaou, B. Ohnesorge, Z. A. Fayad, C. R. Becker, M. Reiser, G. Steinbeck, P. Boekstegers, "Accuracy of 64-slice computed tomography to classify and quantify plaque volumes in the proximal coronary system: a comparative study using intravascular ultrasound", *J. Am. Coll. Cardiol.*, vol. 47, no. 3, pp. 672 – 677, 2006.
- [65] M. Ledesma-Carbayo, P. Mahía-Casado, A. Santos, E. Pérez-David, M. García-Fernández, M. Desco, "Cardiac motion analysis from ultrasound sequences using nonrigid registration: Validation against Doppler tissue velocity", *Ultrasound Med Biol.*, vol. 32, no. 4, pp. 483 – 490, 2006.
- [66] J. Lessick, R. Dragu, D. Mutlak, S. Rispler, R. Beyar, D. Litmanovich, A. Engel, Y. Agmon, M. Kapeliovich, H. Hammerman, E. Ghersin, "Is Functional Improvement after Myocardial Infarction Predicted with Myocardial Enhancement Patterns at Multidetector CT?", *Radiology*, vol. 244, no. 3, pp. 736 – 744, 2007.
- [67] R. Leta, F. Carreras, X. Alomar, J. Monell, J. García-Picart, J. M. Augé, A. Salvador, G. Pons-Lladó, "Coronariografía no invasiva mediante tomografía computarizada con 16 detectores: estudio comparativo con la angiografía coronaria invasiva", *Rev. Esp. Cardiol.*, vol. 57, no. 3, pp. 217 – 224, 2004.
- [68] R. M. Lewitt, "Multidimensional digital image representations using generalized Kaiser-Bessel window functions", *J. Opt. Soc. Am. A*, vol. 7, no. 10, pp. 1834 – 1846, 1990.
- [69] R. M. Lewitt, "Alternatives to voxels for image representation in iterative reconstruction algorithms", *Phys. Med. Biol.*, vol. 37, no. 3, pp. 705 – 716, 1992.

- [70] T. Li, E. Schreibmann, B. Thorndyke, G. Tillman, A. Boyer, A. Koong, K. Goodman, L. Xing, "Radiation dose reduction in four-dimensional computed tomography", *Med. Phys.*, vol. 32, no. 12, pp. 3650 – 3660, 2005.
- [71] T. Li, E. Schreibmann, L. Xing, "Motion correction for improved target localization with on-board cone-beam computed tomography", *Phys. Med. Biol.*, vol. 51, no. 2, pp. 253 – 267, 2006.
- [72] Y. Liang & R. A. Kruger, "Dual-slice spiral versus single-slice spiral scanning: comparison of the physical performance of two computed tomography scanners", *Med. Phys.*, vol. 23, no. 11, pp. 205 – 220, 1996.
- [73] J. Mackay & G. Mensah, *The Atlas of Heart Disease and Stroke*, World Health Organization, 2004.
- [74] R. Manzke, M. Grass, T. Nielsen, G. Shechter, D. Hawkes, "Adaptive temporal resolution optimization in helical cardiac cone beam CT reconstruction", *Med. Phys.*, vol. 30, no. 12, pp. 3072 – 3080, 2003.
- [75] R. Manzke, Th. Köhler, T. Nielsen, D. Hawkes, M. Grass, "Automatic phase determination for retrospectively gated cardiac CT", *Med. Phys.*, vol. 31, no. 12, pp. 3345 – 3362, 2004.
- [76] S. Matej & R. Lewitt, "Practical Considerations for 3D Image Reconstruction Using Spherically Symmetric Volume Elements", *IEEE Trans. Med. Imaging*, vol. 15, no. 1, pp. 68 – 78, 1996.
- [77] C.T. Metz, M. Schaap, A.C. Weustink, N.R.A. Mollet, T. van Walsum, W.J. Niessen, "Coronary centerline extraction from CT coronary angiography images using a minimum cost path approach", *Med. Phys.*, vol. 36, no. 12, pp. 5568 – 5579, 2009.
- [78] K. A. Miles, "Measurement of tissue perfusion by dynamic computed tomography", *Br. J. Radiol.*, vol. 64, no. 761, pp. 409 – 412, 1991.
- [79] T. Mochizuki, K. Murase, H. Higashino, Y. Koyama, S. Azemoto, J. Ikezoe, "Demonstration of acute myocardial infarction by subsecond spiral computed tomography: early defect and delayed enhancement", *Circulation*, vol. 99, pp. 2058 – 2059, 1999.
- [80] G. J. Morgan-Hughes, P. E. Owens, A. J. Marshall, C. A. Roobottom, "Thoracic Aorta at MultiDetector Row CT: Motion Artifact with Various Reconstruction Windows", *Radiology*, vol. 228, pp. 583 – 588, 2003.
- [81] K. Mueller, R. Yagel, J. J. Wheller, "Anti-Aliased Three-Dimensional Cone-Beam Reconstruction of Low-Contrast Objects with Algebraic Methods", *IEEE Trans. Med. Imaging*, vol. 18, no. 6, pp. 519 – 537, 1999.
- [82] F. Müller, P. Brigger, K. Illgner, M. Unser, "Multiresolution approximation using shifted splines", *IEEE Trans. Sig. Proc.*, vol. 46, no. 9, pp. 2555 – 2558, 1998.
- [83] H. G. Musmann, P. Pirsch, H.-J. Grallert, "Advances in picture coding", *Proceedings of the IEEE*, vol. 73, no. 4, pp. 523 – 548, 1985.
- [84] T. Nakanishi, Y. Kayashima, R. Inoue, K. Sumii, Y. Gomyo, "Pitfalls in 16-detector row CT of the coronary arteries", *RadioGraphics*, vol. 25, no. 2, pp. 425 – 438, 2005.
- [85] M. V. Narayanan, C. L. Byrne, M. A. King, "An Interior Point Iterative Maximum-Likelihood Reconstruction Algorithm incorporating Upper and Lower Bounds with Application to SPECT Transmission Imaging", *IEEE Trans. Med. Imaging*, vol. 20, no. 4, pp. 342 – 353, 2001.
- [86] T. Nielsen, R. Manzke, R. Proksa, M. Grass, "Cardiac cone-beam CT volume reconstruction using ART", *Med. Phys.*, vol. 32, no. 4, pp. 851 – 860, 2005.
- [87] K. Nieman, F. Cademartiri, P. A. Lemos, R. Raaijmakers, P. M. Pattynama, P. J. de Feyter, "Reliable noninvasive coronary angiography with fast submillimeter multislice spiral computed tomography", *Circulation*, vol. 106, no. 16, pp. 2051 – 2054, 2002.
- [88] K. Nieman, M. Oudkerk, B. J. Rensing, P. van Ooijen, A. Munne, R. J. van Geuns, P. J. de Feyter, "Coronary angiography with multi-slice computed tomography", *Lancet*, vol. 357, no. 9256, pp. 599 – 603, 2001.

- [89] K. Nikolaou, T. Flohr, A. Knez, C. Rist, B. Wintersperger, T. Johnson, M.F. Reiser, C.R. Becker, "Advances in cardiac CT imaging: 64-slice scanner", *Int. J. Cardiovasc. Imaging*, vol. 20, no. 6, pp. 534 – 540, 2004.
- [90] K. Nikolaou, J. Sanz, M. Poon, B. J. Wintersperger, B. Ohnesorge, T. Rius, Z. A. Fayad, M. F. Reiser, C. R. Becker, "Assessment of myocardial perfusion and viability from routine contrast-enhanced 16-detector-row computed tomography of the heart: preliminary results", *Eur. Radiol.*, vol. 15, 2005.
- [91] A. Okabe, B. Boots, K. Sugihara, S. N. Chiu (eds.), *Spatial Tessellations - Concepts and Applications of Voronoi Diagrams. 2nd edition*, John Wiley, 2000.
- [92] J. D. Pack & F. Noo, "Dynamic computed tomography with known motion field", in *Medical Imaging 2004: Image Processing*, J. Michael Fitzpatrick & Milan Sonka (eds.), vol. 5370, Proc. of SPIE, pp. 3983 – 3986, 2004.
- [93] L. Parra & H. H. Barrett, "List-Mode Likelihood: EM Algorithm and Image Quality Estimation Demonstrated on 2-D PET", *IEEE Trans. Med. Imaging*, vol. 17, no. 2, pp. 228 – 235, 1998.
- [94] J.-F. Paul, M. Wartschi, C. Caussin, A. Sigal-Cinqualbre, B. Lancelin, C. Angel, G. Dambrin, "Late defect on delayed contrastenhanced multi-detector row CT scans in the prediction of SPECT infarct size after reperfused acute myocardial infarction: initial experience", *Radiology*, vol. 236, pp. 485 – 489, 2005.
- [95] B. Perrenot, R. Vaillant, R. Prost, G. Finet, P. Douek, F. Peyrin, "Motion Correction for Coronary Stent Reconstruction From Rotational X-ray Projection Sequences", *IEEE Trans. Med. Imaging*, vol. 26, no. 10, pp. 1412 – 1423, 2007.
- [96] J. Peters, O. Ecabert, H. Schmitt, M. Grass, J. Weese, "Local Cardiac Wall Motion Estimation from Retrospectively Gated CT Images", in *LNC5 5528, Functional Imaging and Modeling of the Heart*, N. Ayache, H. Delingette, M. Sermesant (eds.), Springer-Verlag, pp. 191 –200, 2009.
- [97] W. Press, S. Teukolsky, W. Vetterling, B. Flannery, *Numerical Recipes in C, Second edition*, Cambridge University Press, Cambridge, UK, 1992.
- [98] M. Prümmer, J. Hornegger, G. Lauritsch, L. Wigström, E. Girard-Hughes, R. Fahrig, "Cardiac C-arm CT: a Unified Framework for Motion Estimation and Dynamic CT", *IEEE Trans. Med. Imaging*, vol. 28, no. 11, pp. 1836 – 1849, 2009.
- [99] M. Prümmer, L. Wigstroem, J. Hornegger, J. Boese, G. Lauritsch, N. Strobel, R. Fahrig, "Cardiac C-arm CT: Efficient Motion Correction for 4D-FBP", in *Nuclear Science Symposium Conference Record*, IEEE, San Diego, USA, pp. 2620 – 2628, 2006.
- [100] J. Radon, "Über die Bestimmung von Funktionen durch ihre Integralwerte längs gewisser Mannigfaltigkeiten", *Berichte Sächsische Akademie der Wissenschaft, Math. Phys. Kl.*, vol. 69, pp. 262 – 267, 1917.
- [101] C.J. Ritchie, C.R. Crawford, J.D. Godwin, K.F. King, Kim Yongmin, "Correction of computed tomography motion artifacts using pixel-specific back-projection", *IEEE Trans. Med. Imaging*, vol. 15, no. 3, pp. 333 – 342, 1996.
- [102] H. Robbins & S. Monro, "A stochastic approximation method", *Annals of Mathematical Statistics*, vol. 22, no. 3, pp. 400 – 407, 1951.
- [103] C. E. Rochitte, J. A. C. Lima, D. A. Bluemke, S. B. Reeder, E. R. McVeigh, T. Furuta, L. C. Becker, J. A. Melin, "Magnitude and Time Course of Microvascular Obstruction and Tissue Injury After Acute Myocardial Infarction", pp. 1006 – 1014, 1998.
- [104] T. Rohlfing, C. R. M. Maurer, D. A. Bluemke, M. A. Jacobs, "Volume-preserving non-rigid registration of MR breast images using free-form deformation with an incompressibility constraint", *IEEE Trans. Med. Imaging*, vol. 22, no. 6, pp. 730 – 741, 2003.
- [105] W. C. Röntgen, "Eine Neue Art von Strahlen", *Sitzungsberichte der Physikalisch-Medizinischen Gesellschaft zu Würzburg*, 1895.

- [106] D. Ropers, U. Baum, K. Pohle, K. Anders, S. Ulzheimer, B. Ohnesorge, C. Schlundt, W. Bautz, W. G. Daniel, S. Achenbach, "Detection of coronary artery stenoses with thin-slice multi-detector row spiral computed tomography and multiplanar reconstruction", *Circulation*, vol. 107, pp. 664 – 666, 2003.
- [107] S. Roux, L. Desbat, A. Koenig, P. Grangeat, "Exact reconstruction in 2D dynamic CT: compensation of time-dependent affine deformations", *Phys. Med. Biol.*, vol. 49, pp. 2169 – 2182, 2004.
- [108] W. Rudin, *Principles of Mathematical Analysis*, McGraw-Hill, 1976.
- [109] D. Rueckert, L. I. Sonoda, C. Hayes, D. L. Hill, M. O. Leach, D. J. Hawkes, "Nonrigid registration using free-form deformations: application to breast MR images", *IEEE Trans. Med. Imaging*, vol. 18, no. 8, pp. 712 – 721, 1999.
- [110] F. J. Rybicki, H. J. Otero, M. L. Steigner, G. Vorobiof, L. Nallamshetty, D. Mitsouras, H. Ersoy, R. T. Mather, P. F. Judy, T. Cai, K. Coyner, K. Schultz, A. G. Whitmore, M. F. Di Carli, "Initial evaluation of coronary images from 320-detector row computed tomography", *Int. J. Card. Imaging*, vol. 24, no. 5, pp. 535 – 546, 2008.
- [111] M. Schaap, C. T. Metz, T. van Walsum, A. G. van der Giessen, A. C. Weustink, et al., "Standardized evaluation methodology and reference database for evaluating coronary artery centerline extraction algorithms", *Med. Image Anal.*, vol. 13, no. 5, pp. 701 – 714, 2009.
- [112] Dirk Schäfer, Jörn Borgert, Volker Rasche, Michael Grass, "Motion-Compensated and Gated Cone Beam Filtered Back-Projection for 3-D Rotational X-Ray Angiography", *IEEE Trans. Med. Imaging*, vol. 25, no. 7, pp. 898 – 906, 2006.
- [113] C. O. Schirra, C. Bontus, U. van Stevendaal, O. Dössel, M. Grass, "Improvement of cardiac CT reconstruction using local motion vector fields", *Comput. Med. Imaging Graph.*, vol. 33, no. 2, pp. 122 – 130, 2009.
- [114] H. Schomberg, "Time-Resolved Cardiac Cone Beam CT", in *Proc. 9th Int. Conf. on Fully 3D Reconstruction in Radiology and Nuclear Medicine*, M. Kachelriess & F. Beekman (eds.), Lindau, Germany, pp. 362 – 365, 2003.
- [115] J. Schuijf, J. Bax, L. Salm, J. Jukema, H. Lamb, E. van der Wall, A. de Roos, "Noninvasive coronary imaging and assessment of left ventricular function using 16-slice computed tomography", *Am. J. Cardiol.*, vol. 95, no. 5, pp. 571 – 574, 2005.
- [116] D. Shepard, "A two-dimensional interpolation function for irregularly-spaced data", in *Proceedings of the 1968 23rd ACM national conference*, ACM, New York, NY, USA, pp. 517 – 524, 1968.
- [117] D. L. Snyder, M. I. Miller, L. J. Thomas, D. G. Politte, "Noise and edge artifacts in maximum-likelihood reconstruction for emission tomography", *IEEE Trans. Med. Imaging*, vol. 6, no. 3, pp. 228 – 238, 1987.
- [118] J.C. Spall, "Multivariate stochastic approximation using a simultaneous perturbation gradient approximation", *IEEE Trans. on Autom. Control*, vol. 37, no. 3, pp. 332 – 341, 1992.
- [119] J.C. Spall, "Implementation of the simultaneous perturbation method for stochastic optimization", *IEEE Trans. Aerosp. and ElecSys*, vol. 34, no. 3, pp. 817 – 823, 1998.
- [120] K. M. Stantz, Y. Liang, C. Meyer, S. Teague, M. Stecker, G. Hutchins, G. McLennan, S. Persohn, "In-Vivo Regional Myocardial Perfusion Measurements in a Porcine Model by ECG-Gated Multi-Slice Computed Tomography", in *Proc. of SPIE Medical Imaging Conference*, vol. 5031, pp. 222 – 233, 2003.
- [121] K. Taguchi & H. Anno, "High temporal resolution for multi-slice helical computed tomography", *Med. Phys.*, vol. 27, no. 5, pp. 861 – 872, 2000.
- [122] K. Taguchi, B. S. Chiang, I. A. Hein, "Direct cone-beam cardiac reconstruction algorithm with cardiac banding artifact correction", *Med. Phys.*, vol. 33, no. 2, pp. 521 – 539, 2006.
- [123] K. Taguchi, W. P. Segars, G. S. K. Fung, B. M. Tsui, "Toward time resolved 4D cardiac CT imaging patient dose reduction: estimating the global heart motion", in *Medical Imaging 2006: Physics of Medical Imaging*, Jiang Hsieh J. Michael J. Flynn (ed.), vol. 6142, Proc. of SPIE, San Diego, CA, USA, 2006.

- [124] K. Taguchi, W. P. Segars, H. Kudo, E. C. Frey, E. K. Fishman, B. M. W. Tsui, "Toward time resolved cardiac CT images with patient dose reduction: image-based motion estimation", in *Nuclear Science Symposium Conference Record*, IEEE, San Diego, USA, pp. 2029 – 2032, 2006.
- [125] Task Force of the European Society of Cardiology the North American Society of Pacing Electrophysiology, "Heart Rate Variability: Standards of Measurement, Physiological Interpretation, and Clinical Use", *Circulation*, vol. 93, no. 5, pp. 1043 – 1065, 1996.
- [126] J.-B. Thibault, K. Sauer, C. Bouman, J. Hsieh, "High Quality Iterative Image Reconstruction For Multi-Slice Helical CT", in *Proc. 7th Int. Conf. on Fully 3D Reconstruction in Radiology and Nuclear Medicine*, Y. Bizais (ed.), Saint Malo, France, pp. 51 – 54, 2003.
- [127] R. G. Tilton, K. B. Larson, J. R. Udell, B. E. Sobel, J. R. Williamson, "External detection of early microvascular dysfunction after no-flow ischemia followed by reperfusion in isolated rabbit hearts", *Circ. Res.*, vol. 52, pp. 210 – 225, 1983.
- [128] H. K. Tuy, "3D Image Reconstruction for Helical Partial Cone-Beam Scanners Using Wedge Beam Transform", 2000, US Patent No. 6104775.
- [129] Michael Unser, "Splines: A perfect fit for signal and image processing", *IEEE Sig. Proc. Mag.*, vol. 16, pp. 22–38, 1999.
- [130] M. Unser, A. Aldroubi, M. Eden, "B-spline signal processing: Part I-Theory", *IEEE Trans. Sig. Proc.*, vol. 41, no. 2, pp. 821 – 832, 1993.
- [131] M. Unser, A. Aldroubi, M. Eden, "B-spline signal processing: Part II-Efficient design and applications", *IEEE Trans. Sig. Proc.*, vol. 41, no. 2, pp. 834 – 848, 1993.
- [132] M. Unser, A. Aldroubi, M. Eden, "The L2-Polynomial Spline Pyramid", *IEEE Trans. Pattern Anal. Machine Intell.*, vol. 15, no. 4, pp. 364 – 379, 1993.
- [133] U. van Stevendaal, P. Forthmann, T. Köhler, J. von Berg, C. Lorenz, M. Grass, "Advanced processing for motion-compensated reconstruction in cardiac cone-beam CT", in *Proc. of SPIE Medical Imaging Conference*, vol. 7258, pp. 725833–1, 2009.
- [134] U. van Stevendaal, P. Koken, P.G.C. Begemann, R. Koester, G. Adam, M. Grass, "ECG Gated Circular Cone-Beam Multi-Cycle Short-Scan Reconstruction Algorithm", *Proc. of SPIE Medical Imaging Conference*, vol. 6510, 2007.
- [135] U. van Stevendaal, C. Lorenz, J. von Berg, M. Grass, "Motion-Compensated Reconstruction in Helical Cardiac CT", *Proceedings of the 9th International Meeting on Fully Three-Dimensional Image Reconstruction in Radiology and Nuclear Medicine*, pp. 437 – 440, 2007.
- [136] U. van Stevendaal, J. von Berg, C. Lorenz, M. Grass, "A motion-compensated scheme for helical cone-beam reconstruction in Cardiac CT angiography", *Med. Phys.*, vol. 35, no. 7, pp. 3239 – 3251, 2008.
- [137] M. Vembar, M. J. Garcia, D. J. Heuscher, R. Haberl, D. Matthews, G. E. Böhme, N. L. Greenberg, "A dynamic approach to identifying desired physiological phases for cardiac imaging using multislice spiral CT", *Med. Phys.*, vol. 30, no. 7, pp. 1683 – 1693, 2003.
- [138] J. von Berg & C. Lorenz, "Multi-surface Cardiac Modelling, Segmentation, and Tracking", in *LNCS 3504, Functional Imaging and Modeling of the Heart*, A. F. Frangi, P. I. Radeva, A. Santos, M. Hernandez (eds.), Springer-Verlag, pp. 1–11, 2005.
- [139] G. Voronoi, "Nouvelles applications des paramètres continus à la théorie des formes quadratiques", *Journal für die Reine und Angewandte Mathematik*, vol. 133, pp. 97 – 178, 1907.
- [140] G. Wang, S. Zhao, D. Heuscher, "A knowledge-based cone-beam x-ray CT algorithm for dynamic volumetric cardiac imaging", *Med. Phys.*, vol. 29, no. 8, pp. 1807 – 1822, 2002.
- [141] G. N. Watson, *Theory of Bessel Functions*, Cambridge Univ. Press, Cambridge, U.K., 1944.
- [142] C.-Y. Wee & R. Paramesran, "Measure of image sharpness using eigenvalues", *Inf. Sci.*, vol. 177, no. 12, pp. 2533 – 2552, 2007.
- [143] Wm. G. Weigold, M. E. Olszewski, M. J. Walker, "Low-dose prospectively gated 256-slice coronary computed tomographic angiography", *Int. J. Cardiovasc. Imaging*, vol. 25, no. Suppl. 2, pp. 217 – 230, 2009.

- [144] L. Wexler, B. Brundage, J. Crouse, R. Detrano, V. Fuster, J. Maddahi, J. Rumberger, W. Stanford, R. White, K. Taubert, “Coronary artery calcification: pathophysiology, epidemiology, imaging methods, and clinical implications”, *Circulation*, vol. 94, pp. 1175 – 1192, 1996.
- [145] World Health Organization (WHO), “The top ten causes of death - Fact sheet N310”, October 2008.
- [146] W. Zbijewski & F. J. Beekman, “Characterization and suppression of edge and aliasing artefacts in iterative x-ray CT reconstruction”, *Phys. Med. Biol.*, vol. 49, no. 1, pp. 145 – 157, 2004.
- [147] A. Ziegler, Th. Köhler, T. Nielsen, R. Proksa, “Efficient projection and backprojection scheme for spherically symmetric basis functions in divergent beam geometry”, *Med. Phys.*, vol. 33, no. 12, pp. 4653 – 4663, 2006.
- [148] A. Ziegler, Th. Köhler, R. Proksa, “Noise and resolution in images reconstructed with FBP and OSC algorithms for CT”, *Med. Phys.*, vol. 34, no. 2, pp. 585 – 598, 2007.
- [149] A. Ziegler, T. Nielsen, M. Grass, “Iterative reconstruction of a region of interest for transmission tomography”, *Med. Phys.*, vol. 35, no. 4, pp. 1317 – 1327, 2008.

Samenvatting

*Although nature commences with reason and ends in experience
it is necessary for us to do the opposite, that is to commence with
experience and from this to proceed to investigate the reason.*

— LEONARDO DA VINCI (1452 – 1519)

Iteratieve CT reconstructie is een voortreffelijk alternatief voor de klassieke methode die gebruik maakt van terugprojectie. Met name blijkt de signaal - ruisverhouding die bereikt kan worden met iteratieve CT reconstructie hoger te zijn dan voor beelden die gereconstrueerd zijn met analytische methodes. Een nadeel van iteratieve reconstructie methode zijn de hoge eisen die gesteld worden aan de rekenkracht. Door enkel een deelvolume van het hart, zoals een segment van de kransslagaders of een deel van de linker hartkamer, iteratief te reconstrueren kan de rekentijd echter aanzienlijk worden teruggebracht.

Bestaande reconstructie technieken voor cardiale röntgen-CT sturen de beeldvorming prospectief aan op basis van het elektrocardiogram (ECG) of gebruiken het ECG signaal om retrospectief een reconstructie te maken voor een bepaalde fase van de hartslag. Hierdoor hangt de beeldkwaliteit sterk af van het gekozen tijdsinterval waarin het röntgen-CT beeld gemaakt wordt. Wanneer dit interval wordt vergroot neemt de signaal-ruisverhouding toe, omdat een grotere hoeveelheid van de gemeten projectie data wordt gebruikt. Daarentegen is het risico op bewegingsartefacten bij een breder reconstructie interval groter. Bovendien neemt bij deze technieken de beeldkwaliteit aanzienlijk af in fases waarin het hart erg snel beweegt.

Reconstructie methodes die gebruik maken van bewegingscorrectie geven de mogelijkheid om te corrigeren voor artefacten veroorzaakt door beweging van de anatomie tijdens de beeldvorming. Om gebruik te kunnen maken van deze methodes zijn efficiënte algoritmes nodig die deze beweging af kunnen schatten. Daarnaast moeten deze reconstructie methodes om kunnen gaan met de divergerende beweging die het gevolg is van de pompende beweging van het hart. Wanneer men geen rekening houdt met dit effect kunnen sterke streep artefacten of donkere vlekken in de gereconstrueerde beelden de visualisatie van de kransslagaders en hart kamers bemoeilijken.

Het doel van dit onderzoek was het ontwikkelen van nieuwe technieken voor cardiale diagnostische beeldvorming die een oplossing bieden voor bovengenoemde problemen. In het eerste gedeelte van dit proefschrift werd een nieuwe methode voor

iteratieve reconstructie met bewegingscorrectie voorgesteld die rekening houdt met de divergerende beweging van het hart tijdens het berekenen van de lijn integralen (Hoofdstuk 2). Omdat deze reconstructie methode ervan uitgaat dat de beweging van de objecten in het beeld bekend is in de vorm van een vector veld, werden in de daaropvolgende hoofdstukken drie methodes voorgesteld voor het bepalen van deze vector velden: een handmatige, semiautomatische en volledig automatische methode (respectievelijk Hoofdstuk 3 tot en met 5). Alle drie de methodes maken gebruik van een initieel 4D multi-fase beeld dat is gereconstrueerd op basis van het ECG-signaal. Hieronder volgt een meer gedetailleerde beschrijving van de afzonderlijke hoofdstukken:

Hoofdstuk 2: In dit hoofdstuk werd een nieuwe methode gepresenteerd voor de driedimensionale reconstructie van bewegende objecten op basis van kegelvormige röntgen projectiedata. Om gebruik te kunnen maken van de methode moet de beweging van de objecten in het beeld bekend zijn in de vorm van een vector veld. Voor de berekening van de lijnintegralen wordt een efficiënte methode voorgesteld waarbij het volume van de basis functies wordt aangepast. De methode is geëvalueerd op simulatie beelden en vergeleken met de klassieke terugprojectie methode en een iteratieve reconstructie methode die niet voor beweging corrigeert. Resultaten voor drie verschillende bewegingspatronen in twee gesimuleerde data sets lieten zien dat de methode effectief bewegings- en streepartefacten voorkomt en voor een hogere robuustheid tegen ruis zorgt.

Hoofdstuk 3: In dit hoofdstuk werd een nieuwe methode gepresenteerd voor het iteratief reconstrueren van röntgen-CT beelden van een deelgebied van het hart, waarbij voor beweging wordt gecorrigeerd. De reconstructie methode die als basis dient is gebaseerd op het op een iteratieve manier afschatten van het meest waarschijnlijke 3D beeld. Een vector veld van de beweging van het te reconstrueren deelgebied werd afgeschat door de beweging van handmatig aangegeven herkenningpunten te interpoleren met 'thin plate splines'. Inspectie toonde aan dat de fout in deze handmatig aangegeven herkenningpunten op mag lopen tot 7.5 mm. Grotere fouten leiden tot vervaging van de beelden van de kransslagaders. Voor twee klinische beelden werden de resultaten voor een hartfase met de meeste beweging vergeleken met standaard ECG gestuurde iteratieve reconstructie. Dit toonde aan dat de kwaliteit van de beelden door de voorgestelde bewegingscorrectie aanzienlijk verbetert. De signaal-ruisverhouding van de resulterende beelden is bovendien hoger dan die van beelden gemaakt met terugprojectie methodes die gebruik maken van bewegingscorrectie. Ondanks de eenvoud en efficiëntie van de methode is er ook een beperking te noemen. De bruikbaarheid van de methode hangt namelijk af van de inbreng van een deskundige voor het aangeven van de herkenningpunten. Dit zorgt voor een hogere werklast en variatie in de resultaten door de variatie in het aangeven van de herkenningpunten door experts.

Hoofdstuk 4: In dit hoofdstuk wordt een iteratieve reconstructie methode voorgesteld om bewegingsvrije beelden van de kransslagaders te reconstrueren door bewegingscorrectie op basis van geëxtraheerde vaatassen toe te passen. Zowel het start- als eindpunt van het te reconstrueren segment van de kransslagader moet handmatig worden aangegeven in één tijdpunt van de hart cyclus. Vervolgens wordt het vector veld van de beweging afgeschat op basis van een set centrale vaatassen die in meerder fases van de hartslag geëxtraheerd worden met behulp van minimale kosten paden.

De effectiviteit van de methode werd aangetoond in röntgen-CT beelden van drie patiënten. De methode leverde scherpere beelden op dan een klassieke iteratieve reconstructie methode. Ook werden de resultaten vergeleken met de resultaten van de methode gepresenteerd in hoofdstuk 3, waarin de beweging op basis van herkenningspunten wordt afgeschat. Verbeteringen werden vooral lokaal waargenomen, doordat het vector veld alleen gebaseerd is op de centrale as van de kransslagaders.

Hoofdstuk 5: In dit hoofdstuk werd een nieuwe methode gepresenteerd voor het bewegingsvrij reconstrueren van röntgen-CT beelden van een deelgebied van het hart. Een vector veld van de beweging van het hart wordt afgeschat met een snelle en volledige automatische elastische registratie methode. Deze methode wordt gebruikt om beelden uit verschillende fases van een niet voor beweging gecorrigeerd beeld met elkaar te registreren. Experimenten op klinische en simulatiedata lieten een aanzienlijke verbetering van de beeldkwaliteit in fases met veel beweging zien ten opzichte van standaard ECG gestuurde iteratieve reconstructie methodes. Een kwalitatieve en kwantitatieve analyse van de nauwkeurigheid van het afgeschatte vector veld liet bovendien zien dat voor 90% van de voxels de fout in de gesommeerde elementen van de bewegingsvectoren kleiner is dan de voxelgrootte, en dat voor 95% van de voxels geldt dat deze fout niet groter was dan twee keer de voxelgrootte. In dit hoofdstuk werd ook voor het eerst de volume aanpassing van de basis functies toegepast op klinische data. Dit leverde vooral verbeteringen op voor de divergerende delen van het vector veld nabij de linker hart kamer. Alhoewel de beeldkwaliteit door iteratieve reconstructie met bewegingscorrectie aanzienlijk verbeterde in fases van de hartslag met snelle beweging blijft de beeldkwaliteit van ECG gestuurde reconstructie voor patiënten met een gemiddelde hartslag het beste.

De in dit proefschrift voorgestelde reconstructie technieken kunnen toegepast worden wanneer de huidige ECG gestuurde technieken ook in de rustfases van het hart ernstig verstoord worden door beweging. Een benadering waarin tijdens de reconstructie gecorrigeerd wordt voor deze beweging kan in dit geval de resulterende artefacten in het beeld aanzienlijk verminderen. Bovendien kan door deze nieuwe methodes het reconstructie interval vergroot worden wat een betere signaal-ruisverhouding tot gevolg heeft. Andere potentiële toepassingen liggen op het terrein van functionele beeldvorming van het hart. Voor deze toepassingen is beeldinformatie van bijvoorbeeld de hartkleppen of kamers over de hele hartslag nodig. ECG gestuurde reconstructie levert dan uitstekende beeldkwaliteit voor bewegingsloze fases op, maar de kwaliteit voor fases met veel beweging (bijvoorbeeld tijdens systole) is aanzienlijk lager. De hier voorgestelde methodes kunnen toegepast worden om beelden van hoge kwaliteit voor alle fases van de hartslag te reconstrueren.

De hier beschreven technieken kunnen mogelijk ook voor andere anatomische structuren gebruikt worden.

Een goed voorbeeld is de diagnose van patiënten met een vermoedelijke dissectie van de thoracale aorta. In deze gevallen kunnen streep- en bewegingsartefacten in de röntgen-CT beelden ervoor zorgen dat een niet bestaande dissectie wordt waargenomen of dat een bestaande dissectie wordt gemist. Iteratieve reconstructie met bewegingscorrectie kan hier toegepast worden om deze artefacten te verminderen, waardoor de diagnoseerbaarheid en de toepasbaarheid van de beelden voor het

plannen van de behandeling verhoogd worden.

Een ander voorbeeld is de door ademhalingsartefacten slechte herkenbaarheid van long tumoren in röntgen-CT. De methode uit hoofdstuk 5 zou toegepast kunnen worden om in deze gevallen een bewegingsvrije reconstructie van de longen te maken. De ademhalingsbeweging kan dan afgeschat worden door de verschillende beelden uit een 4D long sequentie elastisch op elkaar te registreren.

Het hier gepresenteerde onderzoek heeft ook een aantal beperkingen. Ten eerste, de verbetering van de beeldkwaliteit is maar voor een beperkt aantal gevallen geëvalueerd. Een uitgebreide klinische evaluatie van de voorgestelde methodes kan daarom niet uitblijven. In een dergelijke studie moet ook gekeken worden naar het optimaliseren van de parameters van de methode om de nauwkeurigheid en robuustheid van de methode te verbeteren. Ten tweede bestaat de voorgestelde reconstructiemethode uit twee stappen. Eerst wordt een afschatting van de beweging gemaakt op basis van een niet voor beweging gecompenseerde reconstructie. Daarna wordt deze informatie gebruikt om een iteratieve reconstructie te maken waarin de beweging wordt gecompenseerd. Om de snelheid en nauwkeurigheid van de methode te verbeteren zou onderzoek gedaan moeten worden naar éénstapsmethodes die het mogelijk maken de beweging af te schatten tijdens het reconstructie proces [114].

Samenvattend, is in dit proefschrift een methode voorgesteld voor iteratieve reconstructie van cardiale röntgen-CT beelden, waarbij gecompenseerd wordt voor de beweging van de anatomie tijdens de beeldvorming. Een significante verbetering van de beeldkwaliteit kan bereikt worden voor fases waarin het hart snel beweegt. De toepassing van de methode is daarom mogelijk interessant voor de evaluatie van vaatsegmenten met verdachte structuren waarbij standaard ECG gestuurde reconstructie methodes een beperkte beeldkwaliteit tot gevolg hebben. Een voorbeeld is de evaluatie van segmenten van de kransslagaders waarin de zachte plak nauwelijks waarneembaar is. De gepresenteerde methodes kunnen zowel de signaal-ruisverhouding verbeteren als ook de bewegingsartefacten beperken om de ambiguiteit van de diagnose te verlagen zonder dat een nieuwe scan gemaakt hoeft te worden.

PhD Portfolio

Research Skills:

- M.Sc. degree in Computer Engineering, Università degli Studi di Catania, Italy, 2006

In-Depth Courses:

- Knowledge driven Image Segmentation, ASCI, Leiden, The Netherlands, September 17–21, 2007

International Conference Presentations:

- IEEE Nuclear Science Symposium & Medical Imaging Conference 2008, Dresden, Germany, October 22–25, 2008, *poster presenter*
- 4th European Congress for Medical and Biomedical Engineering 2008, Antwerp, Belgium, November 23–27, 2008, *oral presenter*
- Computer Assisted Radiology and Surgery (CARS) 2009 Conference, Berlin, Germany, June 23–27, 2009, *oral presenter*
- IEEE Nuclear Science Symposium & Medical Imaging Conference 2009, Orlando, USA, October 25–31, 2009, *poster presenter*

Marie Curie Actions Events:

- Marie Curie Monitoring Mission, Alexander von Humboldt Foundation, Bonn, Germany, January 29–30, 2009

Reviewing:

- Referee activities for various international scientific journals (Medical Physics, Physics in Medicine and Biology, Computer Methods and Programs in Biomedicine, Journal of Healthcare Engineering)

Publications

Publications in International Journals:

- **A. A. Isola**, A. Ziegler, T. Koehler, W. J. Niessen, M. Grass, “Motion compensated iterative cone-beam CT image reconstruction with adapted blobs as basis functions”, *Physics in Medicine and Biology*, vol. 53, no. 23, pp. 6777 – 6797, December 2008
- **A. A. Isola**, A. Ziegler, D. Schäfer, T. Köhler, W. J. Niessen, M. Grass, “Motion compensated iterative reconstruction of a region of interest in cardiac cone-beam CT”, *Computerized Medical Imaging and Graphics*, vol. 34, no. 2, pp. 149 – 159, March 2010
- **A. A. Isola**, M. Grass, W. J. Niessen, “Fully automatic non-rigid registration-based local motion estimation for motion-corrected iterative cardiac CT reconstruction”, *Medical Physics*, vol. 37, no. 3, pp. 1093 – 1109, March 2010
- **A. A. Isola**, C. T. Metz, M. Schaap, S. Klein, M. Grass, W. J. Niessen, “Cardiac motion-corrected iterative cone-beam CT reconstruction using a semi-automatic minimum cost path-based coronary centerline extraction”, *Medical Image Analysis*, *under review*

Publications in International Conference Proceedings:

- **A. A. Isola**, A. Ziegler, D. Schäfer, T. Köhler, W. J. Niessen, M. Grass, “Efficient Projection model for Blobs in Motion-Compensated Iterative Cone-Beam CT”, in *2008 IEEE Nuclear Science Symposium & Medical Imaging Conference Record*, (NSS/MIC 2008, held in Dresden, Germany, October 22–25, 2008), IEEE, M06-317, pp. 4130–4137, 2008
- **A. A. Isola**, A. Ziegler, T. Köhler, U. van Stevendaal, D. Schäfer, W. J. Niessen, M. Grass, “Motion compensated iterative reconstruction of a cardiac region of interest for CT”, in *IFMBE Proceedings ECIFMBE 2008 “4th European Conference of the International Federation for Medical and Biological Engineering”*, (eMBEC 2008, held in Antwerp, Belgium, November 23–27, 2008), J. Vander Sloten, P. Verdonck, M. Nyssen, J. Haueisen (eds.), Springer-Verlag Berlin/Heidelberg, vol. 22, pp. 646–650, 2008

- **A. A. Isola**, M. Grass, T. Köhler, W. J. Niessen, “Motion compensated iterative reconstruction of a cardiac region of interest for CT”, in *International Journal of Computer Assisted Radiology and Surgery* (CARS 2009, held in Berlin, Germany, June 23–27, 2009), Springer Berlin/Heidelberg, vol. 4 (Suppl 1), pp. S33–S34, June 2009
- **A. A. Isola**, A. Ziegler, D. Schäfer, T. Köhler, W. J. Niessen, M. Grass, “Cardiac-motion correction for helical CT”, in *2009 IEEE Nuclear Science Symposium & Medical Imaging Conference Record*, (NSS/MIC 2009, held in Orlando, FL, USA, October 25–31, 2009), IEEE, M09-203, pp. 3247–3250, 2009

Inventions Disclosure & Patent Applications:

- **A. A. Isola**, A. Ziegler, “Line integral calculation for iterative motion compensated reconstruction”, *Philips Intellectual Property & Standards*, Invention Ref. ID295981, 2007

Technical Reports:

- U. van Stevendaal, **A. A. Isola**, M. Grass, “Motion-Corrected Region Of Interest Reconstruction in Cardiac CT”, *Koninklijke Philips Electronics N.V.*, Report Ref. PR-TN 2009/00605, 2009

Curriculum Vitae

Alfonso Agatino Isola was born in Catania, Italy, on February 4, 1978. He received a M.Sc. degree in Computer Engineering from the Università degli Studi di Catania, Italy, in 2006, for his work on methodologies and instruments for the characterization of the Parkinson disease.

From May 2006 to February 2007, he was a Software Researcher at the Surface Radar-TC-TU-Processing department of the Thales Nederland B.V. of Hengelo, the Netherlands. During that period he was involved into three main set of activities: (1) investigation and implementation of one message passing-based middleware for the inter-process communications among radar applications, (2) investigation and implementation of one data distribution service-based middleware for the inter-process communications among radar applications, and (3) working on the parallelization of some codes by using the Intel Threading Building Blocks.

From March 2007 to February 2010, he was a Marie Curie Actions sponsored Ph.D. student at the Department of Medical Informatics and Radiology of the Erasmus MC, University Medical Center Rotterdam, in cooperation with the Philips Research Laboratories, Hamburg, Germany. His research topics were in the field of motion-compensated iterative reconstruction algorithms, and advanced motion estimation methodologies for cardiac computerized tomography. The results are described in this thesis.

Since March 2010, he is working as Research Scientist at the Philips Research Laboratories, Hamburg, Germany. His research interests are in the field of novel image reconstruction methods for cardiac C-arm CT.

